Investigating Mass Transport of Ocean Wave in Nearshore Area

A Study of Wave-Current Interactions

Kai Kang

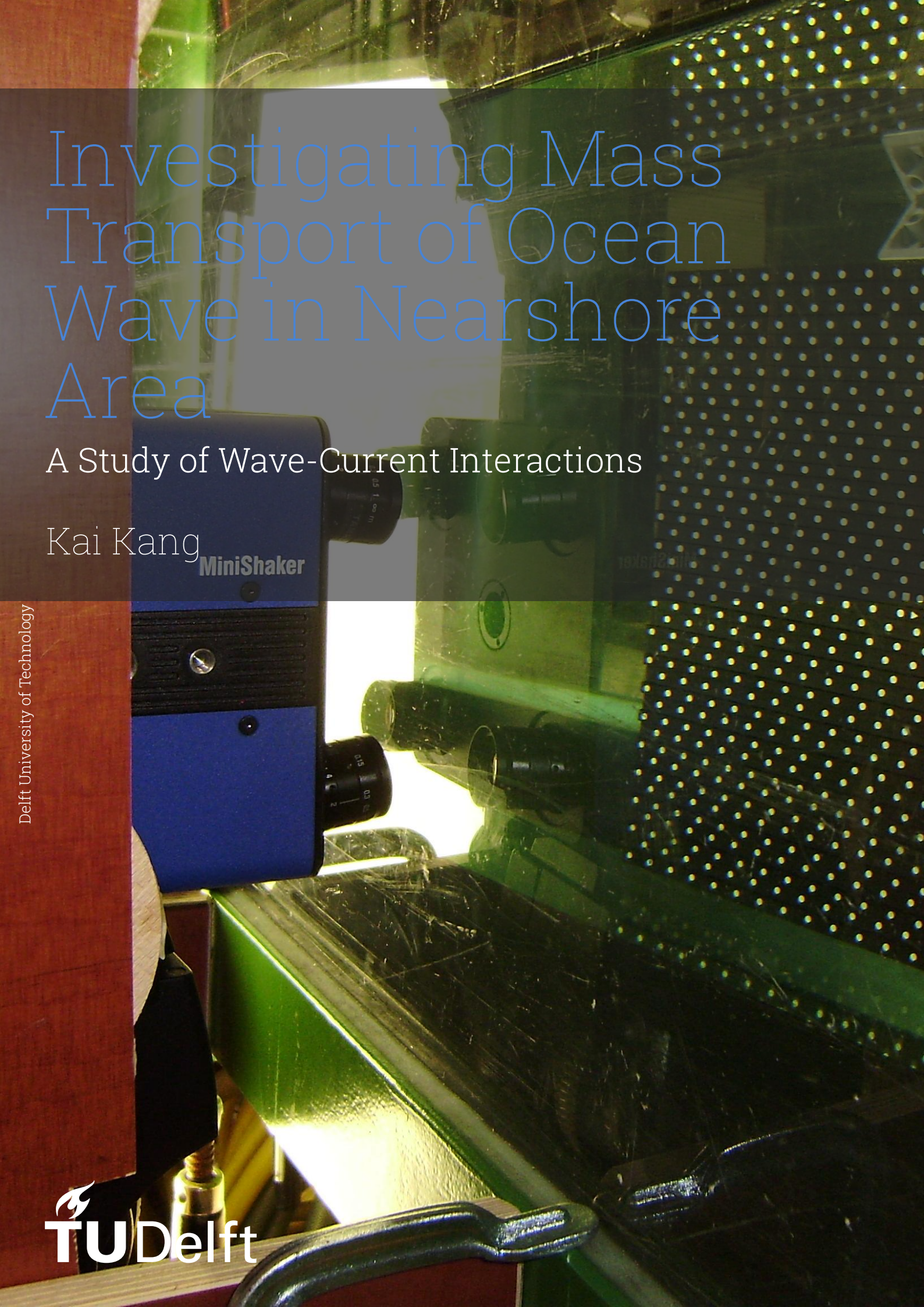

Delft University of Technology

TU Delft

Investigating Mass Transport of Ocean Wave in Nearshore Area

A Study of Wave-Current Interactions

by

Kai Kang

to obtain the degree of Master of Science

at the Delft University of Technology,

to be defended publicly on Thursday September 26, 2024 at 8:45 AM.

Student number:	5686458	
Project duration:	December 15, 2023 – August 26, 2024	
Thesis committee:	Dr. P. Bayle,	TU Delft, supervisor
	Dr. T. S. van den Bremer,	TU Delft, graduation chair
	Prof. W. S. J. Uijttewaal,	TU Delft, secondary supervisor
	Ir. W. Bakker,	Deltares, additional supervisor

TU Delft

Summary

This thesis presents a comprehensive study of Lagrangian and Eulerian mass transport in a wave flume experiment, aiming to improve understanding of mass transport mechanisms and their role in wave-current interactions. This has important implications for nearshore particle transport and pollutant dispersion. The research utilizes state-of-the-art Particle Tracking Velocimetry (PTV) to directly measure the Lagrangian velocity of individual particles, providing higher temporal resolution and precision in capturing unsteady flow phenomena compared to traditional methods. The study compares experimental mass transport data with existing mathematical models, including the irrotational and conduction solutions, and qualitatively discusses the potential importance of the convection model.

The focus of the study is on the temporal evolution of vertical velocity profiles influenced by waves and wave-induced currents, exploring how these profiles change under varying relative water depths (kh) and wave steepness (ka). Additionally, the temporal evolution of vorticity profiles is examined to identify the underlying mechanisms driving these changes.

To extract the net Lagrangian drift from particle tracking data, three averaging methods—time-averaging, wave-by-wave, and low-pass filtering—are compared. The wave-by-wave method is found to be the most suitable for this study.

The velocity profile transitions from an initially irrotational state, characterized by uniform motion near the surface, to a more complex structure resembling the conduction solution as vorticity diffuses. However, the observed profiles do not quantitatively align with the conduction solution. After approximately 60 minutes, the profile stabilizes but continues to exhibit discrepancies from both the irrotational and conduction models.

At equilibrium, while the velocity profiles qualitatively align with the theoretical predictions of the conduction solution, significant quantitative differences remain, particularly in surface drift velocities and the negative peak velocity in the middle of the water column.

The study also shows that as wave steepness increases, deviations from theoretical predictions grow, indicating that higher steepness disrupts the assumptions underlying the conduction solution, leading to greater discrepancies between observed and predicted velocities.

The evolution of the velocity profile is further explained through vorticity transport, where a more uniform vorticity distribution is observed compared to predictions from the conduction solution. This complex behavior is influenced by factors such as sidewall interactions and vorticity convection along the direction of wave propagation.

Acknowledgement

I would like to express my deepest gratitude to my main supervisor, Dr. P. Bayle, for his invaluable guidance, continuous support, and patience throughout my master's thesis journey. His insights and encouragement have significantly contributed to both my academic and personal development.
I am also deeply grateful to my committee members, Dr. T.S. (Ton) van den Bremer, Prof. W.S.J. Uijttewaal, and Ir. W. Bakker, for their thoughtful discussions, technical advice, and unwavering support. Their involvement made this research experience both insightful and enjoyable.
Additionally, I would like to sincerely thank Paul Bayle for designing and leading the experiment, and Jessamy Mol for her invaluable assistance throughout the experimental process. I am also grateful to Jessamy Mol for developing the surface particle tracking program and for her patient guidance, which was crucial to the success of this research.
Finally, I would like to acknowledge LaVision for providing the FlowMaster 4D-PTV system and the corresponding software.

Kai Kang
Delft, September 2024

Contents

1

Introduction

1.1. Motivation

Marine environments are increasingly threatened by the transport and accumulation of floating objects and pollutants, such as plastic debris, oil spills, and chemical contaminants. These pollutants not only harm marine ecosystems but also pose significant risks to coastal communities, fisheries, and tourism. Understanding the behavior of particles and pollutants in ocean currents is critical for developing strategies to mitigate their impact.

In the nearshore area, transport of particles in water become complex. Wave breaking and the bottom in finite depth can significantly alter the transport pattern, thus making it more difficult to predict.

Existing models are mainly divided into three categories: the first is the irrotational solution derived from Stokes wave theory, and the second is the conduction solution, which accounts for vorticity diffusion. The third is the convection model, which accounts for the convective behavior of the vorticity. The first two are able to derive analytical solutions. However, the convection solution is difficult to derive its analytical solution due to the influence of varied boundary conditions such as beach.

Although many laboratory experiments have been conducted, the results show high variability due to varying wave conditions and experiment running time. Neither of the irrotational and conduction solutions consistently predicts the velocity profile accurately. Therefore, we revisited this topic using higher-resolution experimental instruments and performed a more systematic analysis of the evolution of the velocity profiles.

1.2. Technological Advancement

The use of a state-of-the-art 3D Particle Tracking Velocity (PTV) system is an approach in studying wave-induced currents. This advanced technology allows the tracking of neutrally buoyant particles in space and time, leading to a high-resolution volumetric velocity field. Based on thousands of tracks, it also allows one to reconstruct the velocity field. In this way, accurate and detailed analysis can be conducted, providing valuable insights into their behavior and characteristics.

1.3. Main research question

”What are the key determinants of the transport of the particle in water in the nearshore?”

Given the main research question, Detailed research scopes and sub research questions is present in the Chapter 2

1.4. Outline of the thesis

Chapter 1 introduces the research context, defining the problem of studying wave-induced currents and pollutant transport in nearshore areas, followed by the research questions. Chapter 2 provides background on key theoretical frameworks, including the Eulerian and Lagrangian approaches and Stokes drift. Chapter 3 reviews relevant literature, identifying research gaps. Chapter 4 outlines the experi-

mental methodology, including wave flume tests and advanced measurement techniques like Particle Tracking Velocimetry. Chapter 5 presents the results, focusing on current profiles and vortex formation. Chapter 6 discusses the implications and limitations of the findings with the previous research. Chapter 7 concludes with key takeaways and offers recommendations for future research.

2

Background Knowledge and Literature Review

In the study of wave and current dynamics, the Eulerian and Lagrangian frameworks inherently focus on different aspects of fluid motion. The Eulerian approach is well-suited for analyzing vorticity and velocity fields at fixed spatial points, while the Lagrangian approach is more appropriate for examining the transport paths of individual particles and the overall movement of matter within the flow.

2.1. Eulerian Approach

The Eulerian approach examines the fluid flow by observing the properties of the fluid at fixed points in space over time. It is widely used in the analysis of fluid dynamics due to its practical applicability in field measurements and computational models. The main characteristics are the following:

Fixed Spatial Framework:
In the Eulerian framework, observations are made at specific spatial coordinates, which can vary across three dimensions (e.g., $\mathbf{x} = (x, y, z)$). The primary variable of interest in this study is the velocity field, represented as $\mathbf{u}(\mathbf{x}, t)$, where $\mathbf{x}$ denotes the spatial position and t represents time.

Field representation:
Fluid motion is described through a velocity field ($\mathbf{u}(\mathbf{x}, t)$), which provides the velocity vector of the fluid at every point in the domain at any given time. This field-based description facilitates the study of spatial variations in fluid properties and the influence of external forces.

Wave-Induced Currents:
In the context of wave-induced currents, the Eulerian approach focuses on the oscillatory and mean flow components at fixed locations. It captures the temporal variations in velocity due to wave motion and any resulting net currents. The mean Eulerian current ($\overline{U_E}$) is the wave averaged flow observed at a point, hence excluding the oscillatory wave motion. The Eulerian velocity of a flow is commonly measured using devices like the Laser Doppler Velocimeter (LDV), Acoustic Doppler Velocimeter (ADV) or Particle Image Velocimetry (PIV), which can capture the velocity of particles as they pass through a particular location.

2.2. Lagrangian Approach

The Lagrangian approach tracks individual fluid particles as they move through space and time, offering a detailed understanding of particle trajectories and behaviors in the presence of waves.

Moving Reference Frame: In this framework, specific fluid particles are tracked from their initial three-dimensional positions, $\mathbf{X}_0 = (X_0, Y_0, Z_0)$, to their positions at time t, denoted as $\mathbf{X}(\mathbf{X}_0, t) =$

$(X(t), Y(t), Z(t))$. The focus is on the particles' paths as they move through space over time, providing a comprehensive view of their trajectories.

Particle Tracking: The motion of fluid particles is described by their three-dimensional trajectory, $\mathbf{X}(\mathbf{X}_0, t)$, where $\mathbf{X}_0$ represents the particles' initial positions. This approach enables a detailed analysis of particle movement and displacement, allowing researchers to study net transport and dispersion within the fluid.

Wave-Induced Currents: In wave studies, the Lagrangian approach elucidates Stokes drift, which arises due to the asymmetry in particle velocities between the crest and trough of a wave. This results in a net forward displacement of fluid particles over a complete wave cycle.

Measurement Techniques: Lagrangian particle motion is typically measured using techniques such as floating drifters or Particle Tracking Velocimetry (PTV). These methods provide detailed data on the movement and properties of particles within the fluid, offering insights into fluid dynamics from the perspective of individual particles within a moving reference frame.

2.3. Mass Transport

(author?) [4] provide a detailed description of the definition of mass transport in both the Eulerian and Lagrangian frameworks.

2.3.1. Eulerian Mass Transport

In Eulerian description, the horizontal velocity at any point below the water surface and averaging over a wave period shows that:

$$\overline{u}(x,z) = \frac{1}{T}\int_0^T u(x,z), dt = 0 \tag{2.1}$$

where z indicates the vertical coordinate originate from the bottom, at water surface, z=h, and h indicates the water depth. x is the coordinate of the wave propagation direction. $\overline{u}(x,z)$ represents the time-averaged velocity at position (x,z) over a time period T. The term $u(x,z)$ denotes the instantaneous velocity at position (x,z) as a function of time. The result of this time-averaged velocity is zero, indicating no net transport over the wave cycle. In the area between the wave trough and crest, the horizontal velocity is determined using a Taylor series expansion. The surface velocities is as follows:

$$u(x,\eta) = u(x,0) + \eta \left.\frac{\partial u}{\partial z}\right|_{z=0} \tag{2.2}$$

$$= \frac{gak}{\sigma}\frac{\cosh kz}{\cosh kh}\cos(kx-\sigma t) + \frac{ga^2k^2}{\sigma}\tanh kh\cos^2(kx-\sigma t) \tag{2.3}$$

$$= \frac{gak}{\sigma}\cos(kx-\sigma t) + a^2k\sigma\cos^2(kx-\sigma t) \tag{2.4}$$

where η is the surface elevation; a is the wave amplitude; k is wave number, which is related to the wavelength (λ) by $k = \frac{2\pi}{\lambda}$; σ : angular frequency of the wave by $\sigma = \frac{2\pi}{T}$. Then, the wave-averaged Eulerian velocity between the crest and trough can gives:

$$\overline{u}(x,\eta) = \frac{1}{T}\int_0^T u(x,\eta)\, dt = \frac{a^2k\sigma}{2} = \frac{(ka)^2 C}{2} \tag{2.5}$$

Thus, the Eulerian mass transport:

$$M = \int_{-h}^{\eta} \overline{\rho u}\, dz = \int_{-h}^{0} \overline{\rho u}\, dz + \overline{\eta\rho u} = \frac{E}{C} \tag{2.6}$$

where $E = \frac{1}{2}\rho g a^2$ denotes the Wave energy, and $C = \frac{\sigma}{k}$ is the phase speed.

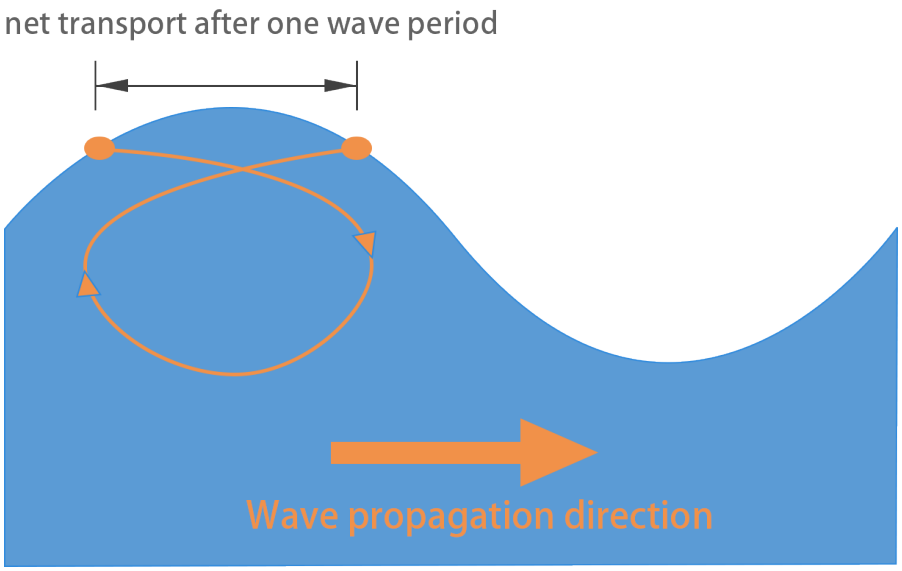

Figure 2.1: Illustration of the Stokes drift in one wave period.

2.3.2. Lagrangian Mass Transport

As discussed earlier, Lagrangian velocity is obtained by tracking individual fluid particles as they move through space. **(author?)** [4] derived the mean value of Lagrangian transport in absence of the Eulerian flow , $\overline{u_L}$, using second-order Stokes wave theory:

$$\overline{u_L} = \frac{a^2 \sigma k \cosh 2kz}{2 \sinh^2 kh} = \frac{g a^2 k^2 \cosh 2kz}{\sigma \sinh 2kh} \tag{2.7}$$

Where h is the water depth. Equation 2.7 means that water particles experience a net drift in the direction of wave propagation, with faster movement near the surface and slower movement near the seabed. By integrating the Lagrangian velocity over the water column and multiplying by the fluid's density, the total mass transport can be calculated:

$$M = \int_{-h}^{0} \rho \overline{u_L}, dz = \frac{\rho g a^2 k}{2\sigma} = \frac{E}{C} \tag{2.8}$$

This result aligns with the Eulerian mass transport expression, demonstrating that both the Eulerian and Lagrangian approaches yield the same total mass transport, albeit through different forms. In the Eulerian framework, the velocity below the water surface is typically zero, while in the Lagrangian framework, the velocity is positive and gradually decreases with depth. Despite these differences in how the velocity is represented in each framework, both ultimately describe the same underlying mass transport phenomenon, ensuring consistency in the overall transport of mass.

2.3.3. Stokes Drift

Stokes drift, introduced by **(author?)** [25] for non-rotating surface gravity waves of finite amplitude, describes the net forward displacement of fluid particles over a wave cycle. As shown in Figure 2.1, unlike in purely linear wave motion where particle orbits are closed, Stokes drift occurs because the orbital motion is slightly asymmetric. This asymmetry arises due to the nonlinear nature of waves: particles spend more time moving at slower speeds in deeper water at the trough than they do at the crest, where they move faster in shallower water.

Consequently, the particles undergo a net forward displacement in the direction of wave propagation [25]. Stokes drift is best understood in a Lagrangian framework, where individual particles are tracked over time. In contrast, within an Eulerian framework, the average fluid velocity at fixed points may be zero below the trough, even though particles experience a net forward motion due to this asymmetry.

The Stokes drift velocity is calculated by the following equation [25]:

$$U_{std} = \frac{a^2 \sigma k \cosh 2kz}{2 \sinh^2 kh} = \frac{g a^2 k^2 \cosh 2kz}{\sigma \sinh 2kh} \tag{2.9}$$

At the water surface($z = h$), the Stokes drift velocity gives:

$$U_{std,surface} = \frac{g a^2 k^2 \cosh 2kh}{\sigma \sinh 2kh} \tag{2.10}$$

Since Stokes drift cannot be determined by the Eulerian method, mass transport studied based on the Eulerian point of view may have been underestimated by some previous studies. **(author?)** [17] emphasizes the significant impact of Stokes drift on nearshore material transport compared to Eulerian currents. The importance of Stokes drift in nearshore environments is underscored, particularly for living and dissolved material transport. Observations show that Stokes drift can be stronger than Eulerian currents, highlighting the need to account for this in nearshore transport models.
The potential nature of Stokes drift has been studied for decades, but remains challenging to observe experimentally. Without vorticity or viscous effects, the Eulerian return flow would ideally be uniform throughout the fluid depth [30]. However, boundary layers at the sidewalls, surface, and bottom of the tank introduce complexities, altering the mean Eulerian flow. [13] and [26] found that turbulence near boundary layers significantly affects the velocity field. Using Particle Image Velocimetry (PIV), **(author?)** [19] extracted Stokes drift velocities by subtracting measured Eulerian mean velocities from Lagrangian velocities (Section 2.4). This method effectively eliminated wavemaker-generated vorticity and closely matched the theoretical Stokes drift profile, though it slightly underestimated theoretical velocity. [30] showed that short quasi-monochromatic waves can prevent a return flow in a closed-flume system by suppressing the wave-induced return flow, thereby avoiding vorticity transport, which would disrupt velocity profile. These results support the leading-order irrotational solution, confirming Stokes drift.

2.4. Generalised Lagrangian Mean

Stokes drift is a Lagrangian mean drift, as mentioned in section 2.3.3. However, the Lagrangian drift is not equal to the Stokes drift in most cases. **(author?)** [1] give an interpretation about this using an Generalized Lagrangian Mean (GLM) to combine the Eulerian and Lagrangian approaches. Applying GLM to wave-flow interaction fields, the expression of the GLM can be reflected by the additional terms as Stokes drift correlation in the following equation [3]:

$$\text{Lagrangian} = \text{Eulerian} + \text{Stokes}$$

The Stokes term represents a correction resulting from wave motion. When the Eulerian velocity is zero, the Lagrangian velocity is equivalent to the Stokes drift, as shown in Equation 2.7. Since Stokes drift arises directly from wave motion and remains constant under steady wave conditions, it plays a key role in wave-current mass transport alongside Eulerian currents.

In the Generalized Lagrangian Mean aspect by 2.4, the wave averaged Lagrangian drift velocity (U_L) is the combination of the wave-averaged Eulerian mass transport velocity $\overline{U_E}$ and the Stokes drift U_{std}:

$$\overline{U_L} = U_{std} + \overline{U_E} \tag{2.11}$$

2.5. Lagrangian Mass Transport Theory and Test

2.5.1. Mass conservation

In a closed wave flume, there is zero net mass transport over the whole flume, the onshore mass flux engendered by Stokes drift is counterbalanced by an offshore return flow, as depicted in Figure 2.4. The continuity equation for incompressible flow in the vertical z and horizontal x directions, when integrated over the depth, is represented as follows:

$$\int_{-h}^{\eta} \overline{U_L}(z)\, dz = 0 \tag{2.12}$$

Here, $\overline{u}(z)$ can be split into contributions from the wave-induced Stokes drift ($\overline{u_{Std}}(z)$) and the return current ($\overline{u_E}(z)$):

$$\int_{-h}^{\eta} \overline{U_{std}}(z)\, dz + \int_{-h}^{\eta} \overline{U_E}(z)\, dz = 0 \tag{2.13}$$

2.5.2. Stokes Irrotational Solution

Equation 2.12 can also be interpreted as the momentum over the water column in the wave flume in any cross-shore profile should be zero, since there is no net flux in the wave flume. In the assumption of Stokes irrotational solution, vorticity is not considered, therefore, the Lagrangian drift velocity according to Equation2.11 is $U_{Std} + \overline{U_{E,depth-uniform}}$. Hence, the Stokes irrotational solution gives [13]:

$$\overline{U_L} = \frac{ga^2k^2 \cosh 2kz}{\sigma \sinh 2kh} - \frac{a^2\sigma}{2h} \coth kh \tag{2.14}$$

However, this approach has been criticized for neglecting inertia effects relative to viscous forces [13]. Since the irrotational solution is only accurate for small displacements, it is applicable only to very small waves.

2.5.3. Conduction and Convection Solution

(author?) [13] experimentally found differences compared to the Stokes solution. **(author?)** [13] states that vorticity diffusion (both viscous (conduction) diffusion and convective (convection) diffusion) depends on $\frac{a^2}{\delta^2}$, where a is the wave amplitude and δ is the boundary layer thickness. The conduction solution, which involves the conduction of vorticity from the bottom boundary layer and the surface boundary layer to the middle water column, is prominent when the wave height is small. In contrast, the convection solution dominates when the wave amplitude is high.

The conduction solution is applied in conditions $\frac{a^2}{\delta^2} \ll 1$ under which may predominate. The paper presents the solution derived from conduction theory as follows:

$$\overline{U_L} = \frac{ga^2k^2}{2\sigma \sinh(2kh)} \left[2\cosh(2kh(1-\mu)) + 3 + kh \sinh(2kh) \left(3\mu^2 - 4\mu + 1\right) + 3\left(\frac{\sinh(2kh)}{2kh} + \frac{3}{2}\right)\left(\mu^2 - 1\right) \right] \tag{2.15}$$

where μ defined as $\mu = 1 - z/h$. Noting that the μ is different from the notation accordingly from [13], in this paper, the z originates from the water surface and $z = -h$ denotes the bottom. But in this paper, z is originate from the bottom and $z = h$, denotes the surface. According to the authors' formulation, the assumption for the solution of the conduction solution to hold is that the flow regime within the bottom and surface boundary layers is laminar, i.e., it is satisfied when $\frac{a^2}{\delta^2} \ll 1$, but the authors reasoned that in some cases, the conduction solution would still be consistent with the results even if the flow regime within the boundary layer is turbulent, which has evoked other researchers to explore the conditions under which the conduction solution applies, and some of the highlighting studies will be presented below

The Convection solution according to [13], is highly dependent on the boundary condition of the beach and the wavemaker, so there is not quantitative analysis given here, but the qualitative analysis is addressed by other research.

2.5.4. Laboratory Experiment

Influence of the relative water depth

(author?) [21] primarily investigated the impact of water depth on surface drifts. Their study revealed that in deep water, surface drifts align well with Stokes' irrotational theory. When the dimensionless parameter kh (where k is the wave number and h is the water depth) lies between 0.7 and 1.3, the internal profiles closely match Longuet-Higgins' conduction solution. However, in very shallow water, where $kh < 0.3$, the profiles show little agreement with either the irrotational or conduction solution and are considered highly unstable over time.

Later research by **(author?)** [15] supported Russell's findings. They observed that for $kh > 1.8$, the profile follows the irrotational solution, while for kh between 0.9 and 1.5, it better aligns with the conduction solution. For long waves with $kh < 0.6$, the profiles become irregular, exhibiting large-scale horizontal circular flows.

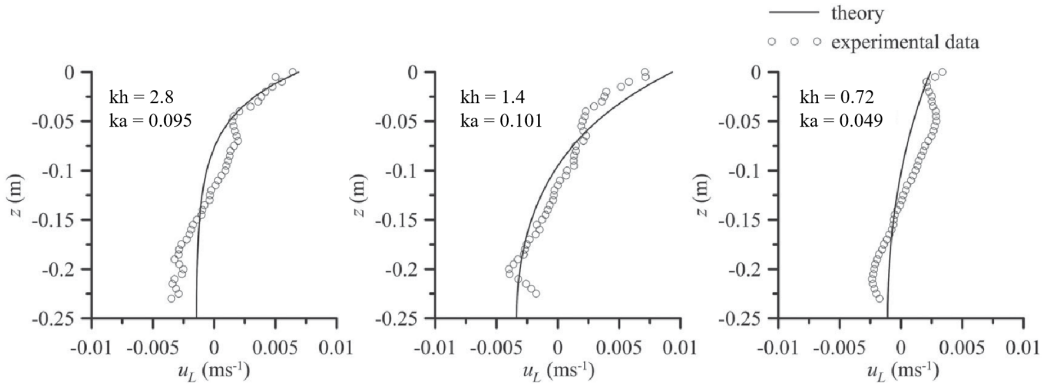

Figure 2.2: Time-averaged Lagrangian velocity from **(author?)** [19]. Theory: Stokes irrotaional solution; Experimental data: PIV measurement

(author?) [2] extended these investigations by studying profile evolution over a sloping bottom. They confirmed that the profile matches the conduction theory most closely around $kh = 1.0$, but its accuracy decreases when kh is below 0.7 or above 1.8. Additionally, they found that theoretical predictions tend to overestimate the observed values but it is likely due to the wave attenuation.
In summary, these studies agree that the irrotational solution fits best in sufficiently deep water, while the conduction solution is most accurate when kh approaches 1. For very long waves in shallow water, significant three-dimensional motion occurs, complicating the profile analysis considerably.

Influence of the experiment duration
In addition to the impact of water depth, many researchers are interested in the temporal evolution of the flow. According to Longuet-Higgins [13], the irrotational solution agree when disregarding vorticity, which is correct when the flow is initially setting up. The conduction or convection solutions, however, necessitate a time scale of d^2/ν to be fully developed. **(author?)** [19] used a PIV system to track particle displacement in the center of a wave flume, sufficiently distant from the beach and wavemaker to avoid vorticity disturbances. The results is shown in Figure 2.2. Their analysis showed that the time-averaged distribution of the Lagrangian mass-transport velocity aligned well with the irrotational solution from $kh = 0.72$ to 2.8, though minor discrepancies were noted. The study did not account for the wavemaker's operational time before measurements, but it suggests that vorticity had insufficient time to diffuse, leading to this initial irrotational state. The time evolution of at the initial stage of the Lagrangian transport velocity profile is examined by Tsuchiya et al [28]. By employing a newly-developed wave flume to remove the effect of Eulerian return flow, a strong correlation with the Stokes profile is noted at considerable water depth ($h/H = 7.36$), showing minimal temporal variation, which is unlike traditional closed wave flumes. For the traditional closed wave flume, after 250 wave cycles, the Lagrangian drift velocity shifts from an irrotational profile to a more conductive one, signifying that initially the flow is irrotational but vorticity soon becomes significant in mass transport velocity. The experiment from Mei et al. [15] cover longer running time. The major finding is that under most of the wave conditions, the flow is usually stable after 1-2 hours which be indicated as 'intermediate stable condition', the Lagrangian profile at this state will be stable and little varied with time. But after longer time (24 hours), for deep water, there's still little change of the profile, but for shallower water condition($0.7 < kh < 1.5$) the profile switch from conduction solution back to irrotational, indicating a more complicated mechanical process happened over very long time scale. Sleath's work [23] also supports these conclusions. Using numerical methods, he found three solutions accounting for wave attenuation. After four hours, the Eulerian surface velocity dropped to zero, leaving only Stokes drift. Comparing long-term surface drift results with Russell [21] and Mei [15], he observed a similar pattern. Good agreement with the conduction solution was found only when kh approached 1.
In summary, the temporal evolution of flow profiles in wave systems transitions from early irrotational behavior, as described by Longuet-Higgins, to a more complex conductive state due to the diffusion of vorticity. Experiments, such as those by Tsuchiya and Mei, show that the response of the conduction is quick, and around 1 hour, the flow stabilizes, but over longer periods, especially in shallow water, the

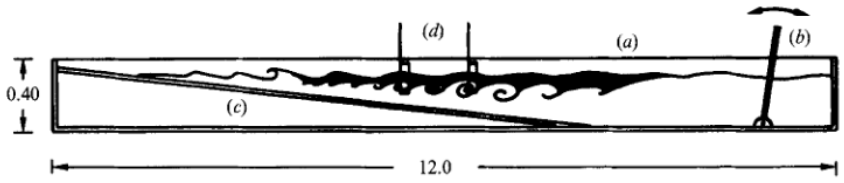

Figure 2.3: Formation of a Vortex Train in the wave flume, refer by **(author?)** [14]

profiles can revert to an irrotational state.

Influence of convected vorticity
Swan's research [26] highlights the potential influence of the convection and vorticity, and shows that the resulting profile can significantly deviate from both the irrotational and conduction solution. But apart from measuring the velocity profile over the water column, there is another phenomenon that may illustrate the convection theory directly. Using the dye tracer method, Matsunaga [14] found that a train of vortices progresses offshore from the surf zone in a certain range of wave and bottom slope conditions; he named this the offshore vortex train, and figure 2.3 illustrates the shape of the vortex train (the dark zone) and its progression in the offshore direction. Based on this finding, Li et al. [12] found two layers of the vortex. This study concludes that the counter current can be unstable due to the propagation of the vorticity.
Although the formation and propagation of the vortex train suggest convective behavior of vorticity, the vortex train only forms under specific conditions and is not a prerequisite for convection to dominate. Quantitative analysis about these vortex and how they influence the velocity profile remain to be solved.

2.5.5. Eulerian Mass Transport and test
In a closed wave flume, there is zero total mass transport over the water depth. Therefore, there should be the existence of the Eulerian counter flow that canceled the mass transport induced by Stokes drift in the scale of the whole water column,[13].

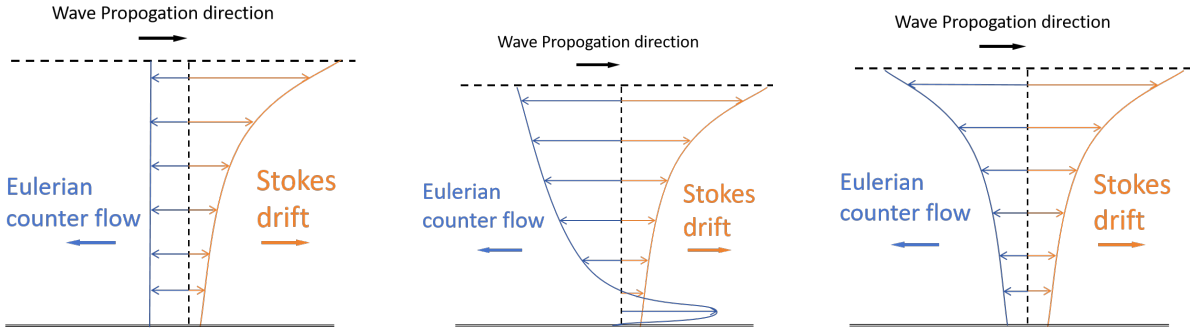

(a) Depth-uniform **(b)** Sheared **(c)** Anti-Stokes

Figure 2.4: Comparison of different shapes of Eulerian counter flow

2.5.6. Depth-uniform Eulerian current
The irrotational solution of **(author?)** [25] neglects the viscous effects of the boundary layer, resulting in a uniform pressure gradient across the water column. Even with boundary layer effects, vorticity does not diffuse into the interior, maintaining a nearly uniform pressure gradient and forming a depth-averaged Eulerian flow (see figure 2.4a). This uniformity and irrotation implies that the flow is not affected by any vorticity or boundary layer. The current speed and direction are invariant with depth from the surface to the bottom. The depth-uniform Eulerian mass transport velocity U_E must counterbalance the total onshore mass transport induced by Stokes drift. Given that U_E is consistent across the depth,

its integral is straightforward: in 2.16

$$\overline{U_E} \cdot h = -\int_{-h}^{0} U_{std}(z)\, dz \tag{2.16}$$

Rearrange the equation to solve for the depth-uniform Eulerian current:

$$\overline{U_E} = -\frac{1}{h}\int_{-h}^{0} U_{std}(z)\, dz \tag{2.17}$$

Note that the first term of the irrotational solution from Equation 2.14 is the Stokes drift velocity shown by Equation 2.9, while the second term is the Eulerian return current derived by bringing U_{Std} into Equation 2.17.

2.5.7. Other Eulerian current profile

When the vorticity and the viscosity have to be considered, which is common in the laboratory wave flume or finite water depth condition, the Eulerian flows often exhibit shear flow properties, manifesting a non-uniformity in depth. The non-uniformity of the flow can result from the advection and diffusion of vorticity from the vertical or horizontal boundaries [13], which requires a relatively long time to fully develop [29]. This vorticity is highly sensitive to various conditions, such as temperature fluctuations, the boundaries of the laboratory flume, and disturbances caused by wave makers, making it difficult to derive a quantitative solution that applies to all scenarios [26]. Overall, the velocity profile typically exhibits a sheared flow, as shown in figure 2.4b. The flow velocity decreases gradually from the surface toward the bottom, until it reaches the boundary layer near the seabed. In this region, there is a rapid change in velocity, eventually reaching zero at the bottom boundary [9]. In addition, there are some different forms of Eulerian flow such as the anti-Stokes Eulerian flow analysed by **(author?)** [16] and others, in which, the Eulerian flow will cancelled out the Stokes drift at each depth, not in integration aspect.

Because of the complexity of the vorticity aspect, specific expression will not be present in this paper, but further detailed review will be present in the next section. But still, though these deviations, the evolution of the Eulerian flow is an intuitive way to study the variation of the flow inside the flume.

Generally, by using the concept from **?**], In order to obtain the observed Eulerian return data, an additional step to convert from the average result of the Lagrangian mass transport velocity into an Eulerian flow according to the equation 2.11, which will be equation 2.18

$$\overline{U_E} = \overline{U_L} - U_{std} \tag{2.18}$$

2.5.8. Laboratory Experiment

(author?) [9] and **(author?)** [18] both investigated Eulerian mass transport in regular waves, using Laser Doppler Velocimetry (LDV) and other laboratory techniques. Their results show a consistent evolution of the Eulerian velocity profile from offshore to onshore along a sloping bottom. The Figure 2.5 shows the results of Hwuang in different station located in different water depth, and Table 2.1 shows the relative statistic. Offshore, before the breaking point, the horizontal Eulerian velocity remains relatively depth-uniform. However, as the wave propagates towards the shore and the dimensionless wavenumber kh decreases, the velocity profile develops a negative shear, with surface velocities becoming more negative relative to the bottom. This shear effect intensifies within the surf zone, where the influence of wave breaking further enhances the velocity gradient near the surface.

Table 2.1: Wave stastistics of the experiment by Hwung et al. d: water depth at each location; H: the wave height at each location.

	T(s)	h (cm)	H (cm)	kh	ka
Offshore	1.45	33.0	5.30	0.92	0.074
Station 1	1.45	17.4	5.59	0.60	0.097
Station 2	1.45	13.0	5.70	0.49	0.107
Station 3	1.45	9.8	5.78	0.39	0.114

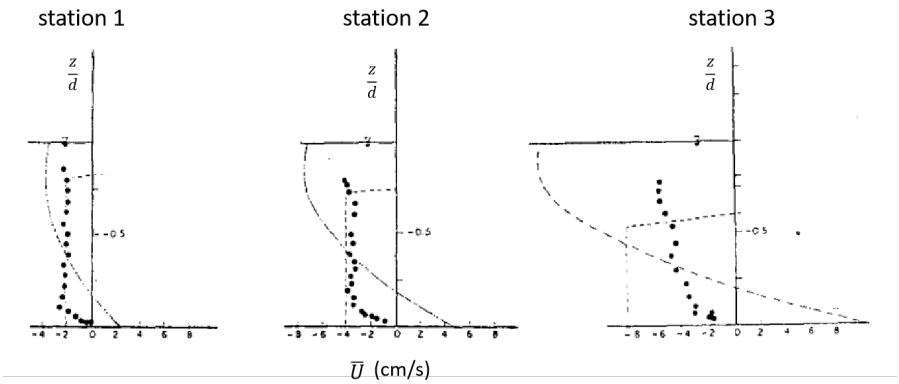

Figure 2.5: Mean Eulerian velocity measured by **(author?)** [9]. ● : Experiment result; - - -: Theoretical depth-averaged velocity below the trough; — — Conduction solution.

The vortex train observed by **(author?)** [14] was present in Test 2 but absent in Test 7, as shown in Figure 2.6. Table 2.2 provides the relevant statistics for each test. Test 2 exhibited a double sheared layer, while Test 7 showed only a single negative sheared layer. The presence of the vortex train, associated with lateral vorticity convection, can significantly affect the Eulerian flow profile, leading to instabilities and variations in the velocity structure.

Table 2.2: The statistic with Test 2 and Test 7 in **(author?)** [12]

Test	H (m)	T (s)	h (m)	ka	kh
2	0.09	2	0.31	0.08	0.59
7	0.15	1.1	0.31	0.31	1.3

Swan [26] using the LDV to investigate the Eulerian profile evolution with time at the centre of the wave flume with the relative water depth $kh = 1.9$, who considered mainly the effect of time and found that at an early stage (t = 0) in the middle of the water column the Eulerian flow was close to the Stokes irrotational theory (depth-averaged Eulerian flow), whereas the velocities close to the bed surface were positive. However, as the eddy developed (t=1.0h and 2.5h), the Eulerian velocity flow at the surface of the water column was three to four times larger than the original negative velocity, making the whole profile more negatively sheared. It is noteworthy that **(author?)** [26] also compares the conduction solution obtained from eddy-diffusion effects only and finds that the observed and theoretical curves do not match, hinting at the influence of convection.
(author?) [16] summarized the experimental results of **(author?)** [11], **(author?)** [26] and **(author?)** [27], and give some reanalysis, which shows a good agreement with the anti-Stokes profile. And furthur more, this paper also associates this anti-Stokes model of Eulerian flow with Gerstner wave theory which is rotational Lagrangian wave theory, and argues that the use of Gerstner theory explains this anti-Stokes flow well, but that the dynamics behind it are not yet clear.

2.6. Summary review of the previous laboratory experiment

Eulerian and Lagrangian measurements and profile

Although the results from the Eulerian and Lagrangian approaches differ, the theoretical distinction between them, according to **(author?)** [1], lies in the term of Stokes drift. **(author?)** [19] demonstrated this difference through experimental measurements, while **(author?)** [30] validated the Stokes drift predicted by **(author?)** [25]. Additionally, **(author?)** [28] simulated an infinitely long wave flume to eliminate the effects of Eulerian flow, finding good agreement with the Stokes drift calculated by Equation 2.9.
In the Eulerian framework, the depth-uniform return current beneath the trough aligns with the irrotational solution in the Lagrangian framework. The work of **(author?)** [8] and **(author?)** [18], using LDV, agrees with the particle tracking results of **(author?)** [2]. These studies show that, over a sloping bed where kh decreases continuously until wave breaking, the Eulerian profile shifts from depth-uniform to

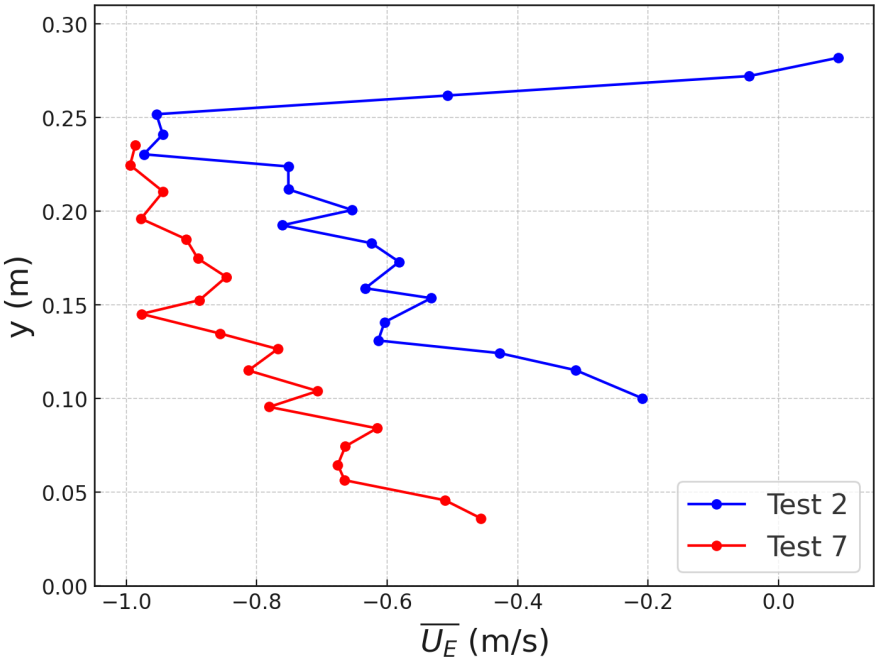

Figure 2.6: (author?) [12] measurement result, Test2 and Test 7.

sheared, while the Lagrangian drift evolves from an irrotational to a more rotational flow.

The Influence of Wace Conditions

Laboratory studies have identified three distinct Eulerian profile patterns: depth-uniform, sheared, and anti-Stokes (Figure 2.4). Only the depth-uniform profile indicates an irrotational flow, while the sheared and anti-Stokes profiles both exhibit rotational characteristics. Whether the flow is rotational or irrotational depends heavily on local wave statistics [9, 18] and time [26]. Lagrangian experiments suggest that, contrary to **(author?)** [13]'s expectations, the conduction solution applies over a broader range of water depths than initially assumed ($\frac{a^2}{\delta^2} \ll 1$). For instance, **(author?)** [21] extended the applicable conditions to $0.5 < kh < 1.3$. However, **(author?)** [15] found that the conduction solution is not the final state of the drift profile. Their experiments revealed a puzzling phenomenon: over a long period, flow transitions from conduction to an irrotational state [15], yet a systematic analysis of the evolution of the current profile remains unclear. Additionally, neither **(author?)** [21] nor **(author?)** [15] addressed the effect of the wave steepness (ka) on velocity profiles.

In shallow water, wave-induced flow is strongly influenced by vorticity not only from the boundary layer but also from the free surface [6] and sidewalls [15]. **(author?)** [14] and **(author?)** [12] highlighted the impact of vorticity convected from the beach, which can deviate the flow from both irrotational and conduction solutions [26], resulting in a double sheared layer [12]. However, these factors are dominant under specific experimental conditions and timescales.

The shortcoming of the previous measurement method

Earlier studies, such as those by **(author?)** [15], primarily measured transient velocity using dye displacement and surface drift by filming particles. While dye measurements can be affected by viscous diffusion and turbulence, leading to overestimated results compared to neutrally buoyant particles [21], these methods offered limited accuracy and could not capture full-depth transient displacement. Neutrally buoyant particles provide more reliable data but fail to capture detailed flow changes across the entire water column.

Modern techniques like Particle Image Velocimetry (PIV) have improved flow field measurement by averaging velocity in different regions, providing both Eulerian and Lagrangian data simultaneously [19]. However, PIV often lacks the resolution to account for temporal evolution in the velocity profile.

State-of-the-art Particle Tracking Velocimetry (PTV) systems, on the other hand, directly track the Lagrangian velocity of individual particles, offering higher temporal resolution and precision in capturing unsteady flow phenomena. Revisiting this topic using PTV could provide new insights into turbulence, vorticity, and time-evolving flow fields with far greater detail than traditional methods.

2.7. Research scopes and research questions

2.7.1. Research scopes

This thesis focuses on: 1. Using wave gauges to analyze wave data and obtain the theoretical Stokes drift. Extracting the Lagrangian drift from particle trajectories measured by PTV and image tracking, Obtaining the Eulerian velocity using the Lagrangian drift velocity and Stokes drift.
2. Understanding the velocity profile taken into account Stokes drift and wave-induced current velocity in laboratory experiments in comparison with the irrotational solution and conduction solution, based on different wave conditions and running time.
3. Understanding the evolution of vorticity over the water column over time and how vorticity influences the velocity profile.

2.7.2. Sub research questions

1. What methods can be used to obtain the drift velocity from particle tracking data? What is the level of uncertainty in doing so? How does this uncertainty affect the analysis?
2. How do wave characteristics, such as relative wave height, steepness affect the velocity profile? How does it compare to the irrotational solution and the conduction solution?
3. From a temporal perspective, what changes occurred in the velocity profile? How does it compare to the irrotational solution and the conduction solution?
4. Can the evolution of the velocity profile be explained from the perspective of vorticity transport?

3

Methodology

This chapter outlines the methodology employed to investigate wave-induced current profiles under controlled laboratory conditions. Monochromatic waves were tested across various scenarios. First, the experimental setup and procedures are described in Section 3.1. The methodology for time-domain analysis, including the calculation of wave parameters, wave skewness and asymmetry, and viscous wave attenuation, is detailed in Section 3.2. Section 3.3 presents the spectral domain analysis. Section 3.4 focuses on the surface drift tracking methodology, emphasizing the use of the Z-camera and the Averaging method to determine surface drift velocity. In Section 3.5, the application of the PTV system for tracking particles in the mid-water column is discussed, including an evaluation of the tracer's settling velocity. Furthermore, Section 3.6 provides a detailed explanation of Lagrangian velocity calculations for the PTV system, with three averaging scenarios presented. Finally, Section 3.7 outlines the method for obtaining the vorticity profile, following the determination of the drift velocity profile.

3.1. Laboratory experiment

3.1.1. Experiment test runs

Five wave conditions, each exhibiting distinct characteristics, were subjected to testing, with each wave undergoing repetition between three to five times. Monochromatic waves were employed in this experiment. The forced values, denoting the input parameters to the wavemaker, are given in Table 3.1. The table also lists the calculated non-dimensionless parameters and indicates the potential formation of the Matsunaga vortex train according to the criteria outlined by **(author?)** [14].

Table 3.1: Wave Characteristics and Parameters. h: water depth; a: wave amplitude; T: wave periods; ka: relatively wave steepness; kh: water depth; Ur: the Ursell number; Re: the Raynold number; Matsunaga vortex: Whether or not the given condition will form vortex train; Repeat times: The times of the experiment repeat

	Type	h (m)	a (m)	T (s)	ka	kh	Ur	Re	Matsunaga vortex	Repeat times
Wave 1	Regular	0.35	0.050	1.8	0.10	0.71	22	12500	Yes	5
Wave 2	Regular	0.35	0.065	1.4	0.18	0.96	16	22300	No	4
Wave 3	Regular	0.35	0.030	1.2	0.10	1.18	5	5000	No, but yes landward	3
Wave 4	Regular	0.35	0.035	1.4	0.09	0.96	8	6500	No, but yes landward	3
Wave 5	Regular	0.35	0.020	0.85	0.11	2.02	1.1	711	No, but yes landward	4

The following figure 3.1 shows the Le Mehaute diagram that illustrates wave behavior under different water depth conditions using dimensionless parameters $\frac{h}{gT^2}$ and $\frac{H}{gT^2}$, with h, still water depth and H, wave height in Table 3.1. The diagram is divided into shallow water, intermediate water depth, and deep water regions.

- **W1 and W2**: Located in the intermediate water depth region, close to Cnoidal wave theory zone, in the 3rd Stokes theory zone.
- **W3 and W4**: Both are located in the intermediate water depth region, in the 2nd order Stokes

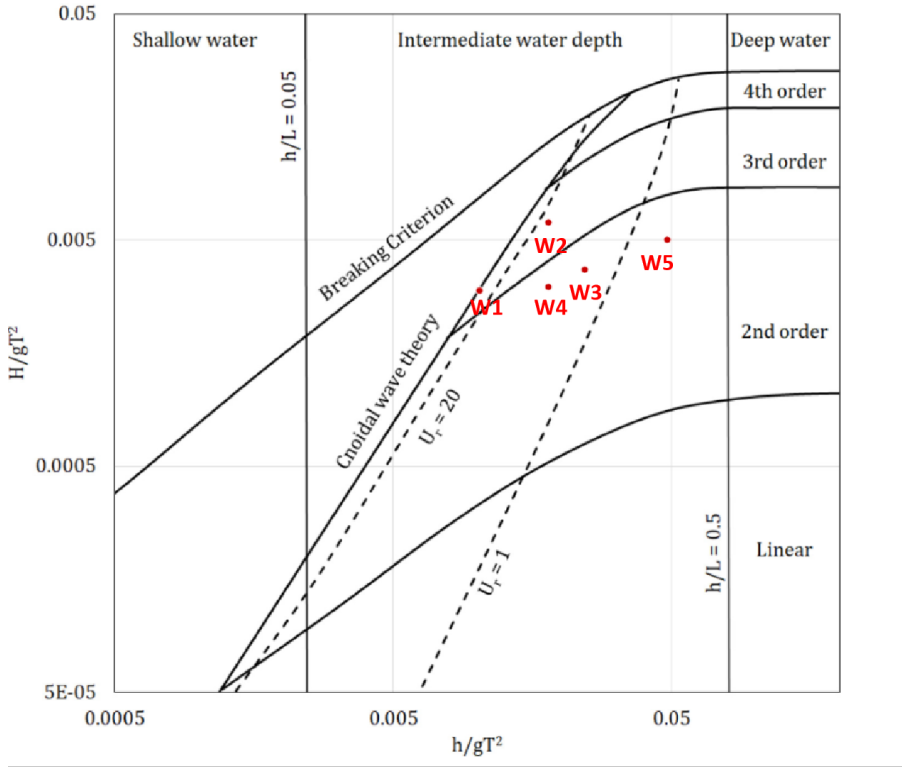

Figure 3.1: Five kinds of waves running in experiment with the position in the diagram of Le Mehaute's diagram

wave theory zone.

- **W5**: In the intermediate water region, in the second-order Stokes wave theory zone.

3.1.2. Wave flume configuration

The experiment is undertaken in the TUDelft faculty of Civil Engineering and Geosciences. A wave flume with the length of 39 m $\times$ and a width of 0.79 m is used. Figure 3.2 and Figure 3.7 shows the configuration of the wave flume. There are majorly 5 components in the wave flume:

Wavemaker The wavemaker is a piston, wet back type, located at one end of the wave flume to generate artificial waves in a controlled environment, as shown in Figure 3.3. The gap between the paddle and the flume is sealed to prevent wave leakage, and active wave absorption is employed to minimize reflected waves.

Beach To dissipate waves and prevent reflection, a planar wooden beach with a slope of 1:25 is positioned at the other end of the flume, as illustrated in Figure 3.4.

Wave Gauges The resistive wave gauges consist of two thin parallel rods that measure changes in water level by detecting variations in conductance, which are then converted into surface elevation as a function of time (see Figure 3.5). These gauges are mounted on a horizontal beam above the wave flume, with 10 gauges positioned at fixed locations (the blue dots in Figure 3.2). The first three gauges record offshore wave conditions and help calculate the reflection coefficient. WGH 4 and WGH 5 are positioned near the PTV system and Z-camera, while the remaining gauges monitor wave shoaling and surf. To avoid interference with the PTV and Z-camera, WGH 4 and WGH 5 were used only in the first experiment and removed in subsequent trials.

Z-camera The Z-camera is located 3 meters above the wave flume, capturing images of the water surface at a resolution of 3860x2140 pixels and 30 frames per second (fps). The images are processed

to obtain the drift velocities with a range of 1.7m $\times$ 0.85m during 80-second intervals at predetermined time slots, as depicted in Figure 3.6.

PTV LaVision's FlowMaster Shake-the-Box system used consists of a high-resolution camera for tracking particle motion. The camera captures detailed images of the fluid and seeded particles, ensuring precise measurements of their displacement over time. Figure 3.7 shows the experimental setup, while Figure 3.8a presents an on-site photo taken during calibration. The calibration plate (Figure 3.8b) is removed during the actual experiment. Detailed information is presented in 3.5

Table 3.2 provides the locations of the equipment, with the origin at the zero position of the wavemaker paddle.

Table 3.2: Locations of the experiment devices in the wave flume. The PTV LED window indicates the glass windows located at the bottom of the flume, as shown in figure 3.8a; The "Offshore" and "Onshore" refer to the two ends of the window based on the wave direction.

Wave Gauge	**Cross-shore Location (x) from the wavemaker rest position (m)**
WHG1 (G15)	12.37
WHG2 (G12)	12.79
WHG3 (G16)	13.47
WHG4 (G7)	21.79
WHG5 (G11)	24.06
WHG6 (G9)	28.38
WHG7 (G17)	28.89
WHG8 (G26)	29.41
WHG9 (G21)	29.90
WHG10 (G22)	30.42
PTV LED Window	
Offshore	22.53
Onshore	23.33
Z_Camera	
Lense	21.33

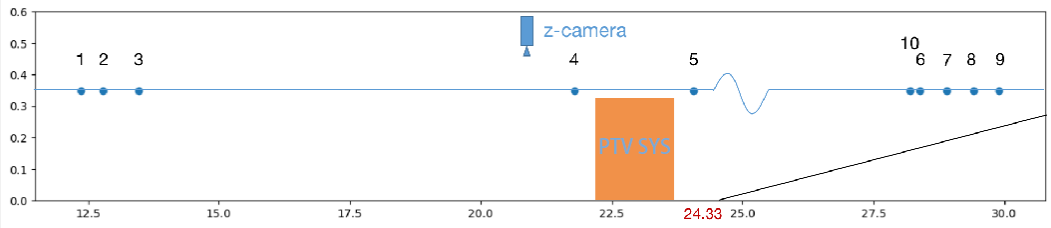

Figure 3.2: Experiment setup of the wave flume.

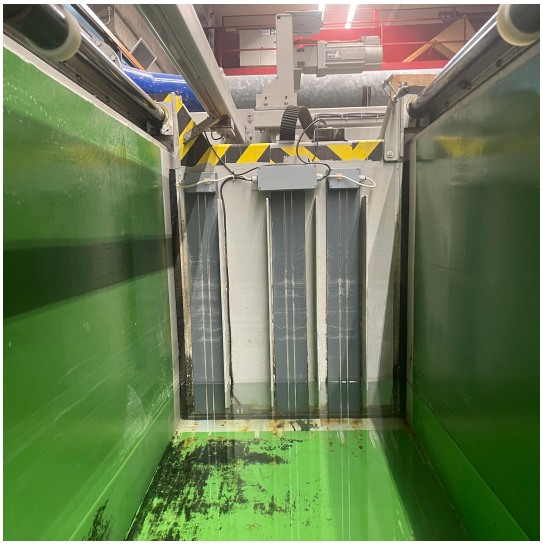

Figure 3.3: Wavemaker

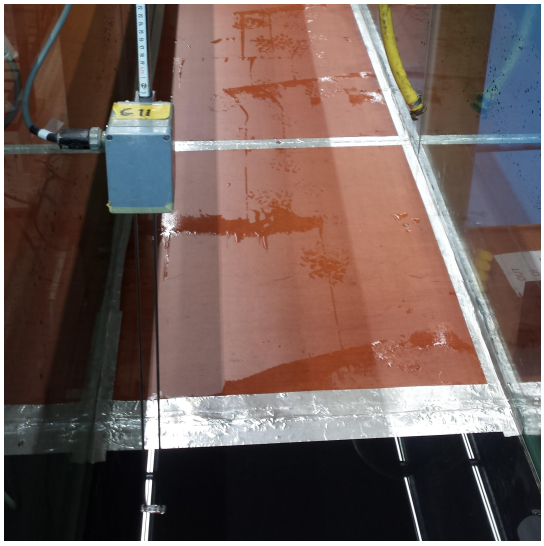

Figure 3.4: Beach

Figure 3.5: Wave Gauge

Figure 3.6: Z-camera

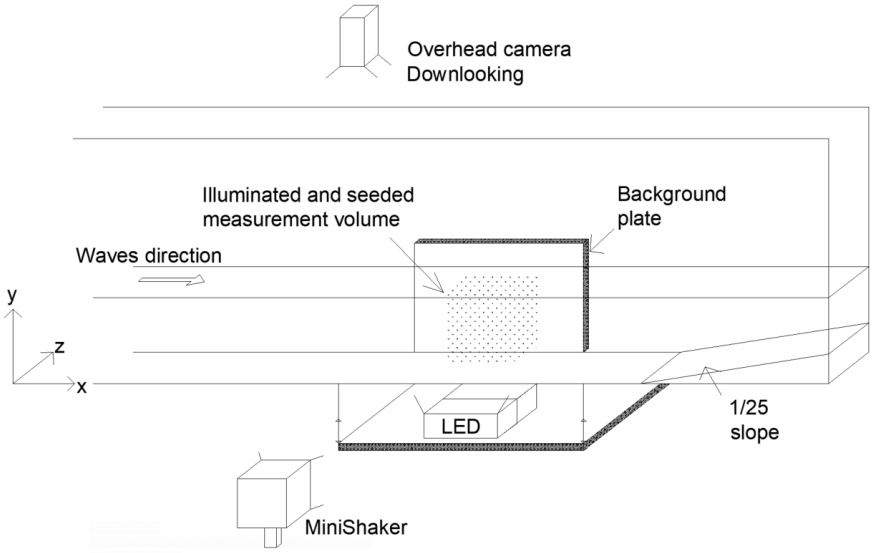

Figure 3.7: Experimental setup with location of overhead camera and PTV system

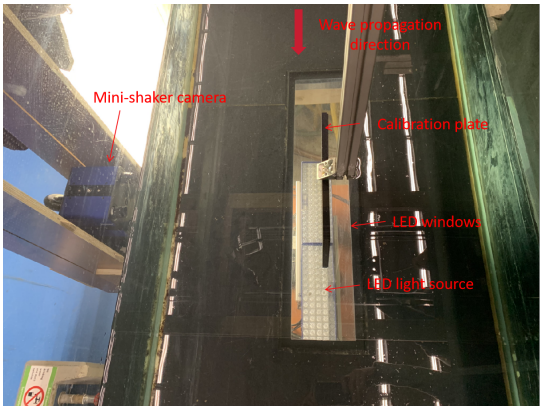

(a) PTV setup with labeled components

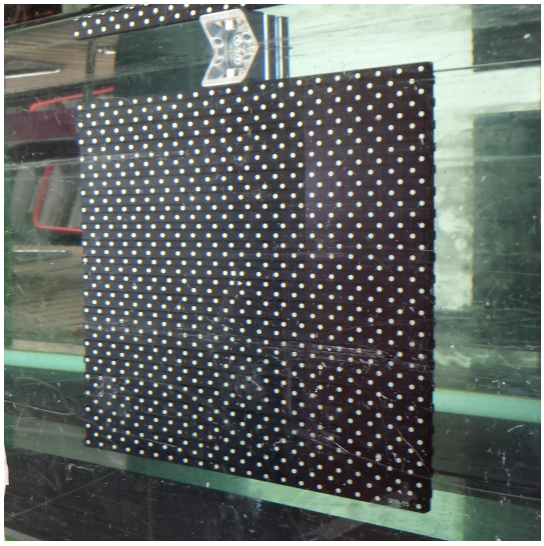

(b) Calibration plate close-up

3.1.3. Experimental Procedure

This experiment focuses on the evolution of the velocity profile over a 120-minute period, and record observational data is at different time intervals. However, due to the large storage space occupied by the image data from the PTV system and Z-camera, continuously recording for 120 minutes is impractical. At the same time, the recording duration should not be too short to ensure that each camera record contains enough waves to eliminate randomness. Therefore, the duration of each recording is set to 80 seconds, ensuring that the longest recorded particle in the PTV system and Z-camera can experience more than 30 waves. The specific experimental procedure is shown in Figure 3.9.

Meanwhile, the recording by the wave gauge is continuous. The start and end times of the wave gauge recording encompass the entire duration of the wave-maker operation. The wave gauge starts recording before the wave-maker begins and stops as soon as the wave-maker finishes.

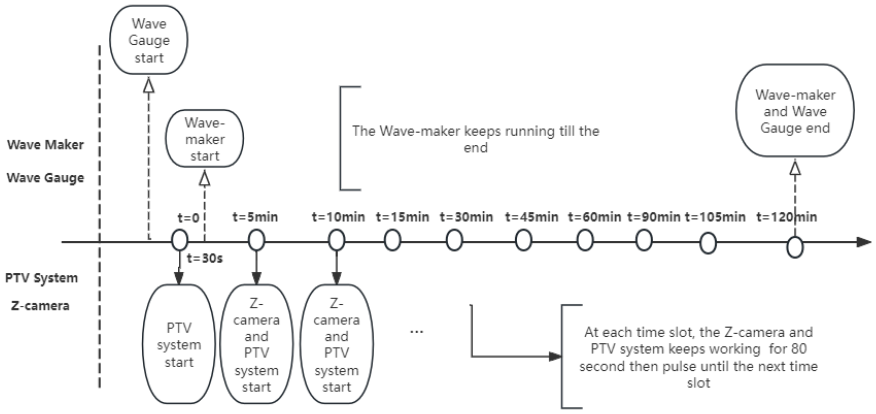

Figure 3.9: Device measurement procedure of one single running

3.2. Time domain wave analysis

3.2.1. Wave gauge calibration

During the experiment, the wave gauges were calibrated before the wave. We adjusted the height of the wave gauge so that the detection voltage of the wave gauge corresponding to the highest initial position was recorded from the highest position, and each time it was adjusted down by 10cm, and the detection voltage of the adjusted down position was recorded at the same time, so that we obtained the change of the voltage value and the change of the water surface position relationship. In a certain range of the wave gauge measurement, the relation between the water elevation (h) and the voltage (V) can be seen as a linear relation as the Eq.(3.1). Figure 3.10 shows the example of the linear relation between the voltage that the measure directly obtains and the actual water elevation. From this graph, the slope parameter a and intercept b can be calculated.

$$h = a * V + b \tag{3.1}$$

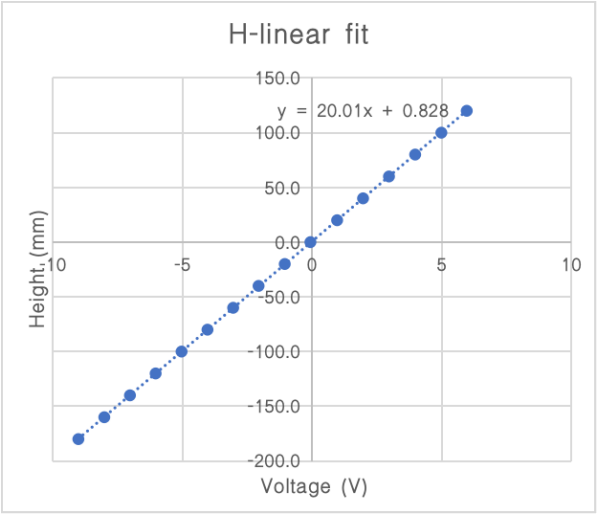

Figure 3.10: Example of relation between Voltage and water elevation

3.2.2. Data Detrending

Wave signal detrending is the process of removing the overall trend or long-term linear changes in a wave signal. Detrending the data in this experiment is necessary due to the extended duration of each run, which lasts two hours. It is essential to disentangle wave characteristics from overarching

trends, such as the decreasing of water level changes caused by leaking, evaporation, or drift of wave gauges. This practice enhances signal fidelity, facilitating a more precise analysis of wave-specific fluctuations and ensuring the accuracy of statistical metrics, including the mean and standard deviation. Mathematically, for a time series $y_i(t)$, a linear trend can be expressed as:

$$y_i(t) = at + b + \epsilon(t) \tag{3.2}$$

Least-squares method is used to find the coefficients a and b that minimize the sum of squared residuals:

$$\sum_{I=1}^{N}(y_i - (a \cdot x_i + b))^2 \tag{3.3}$$

This can be represented in matrix form as:

$$\mathbf{y} = A\mathbf{c} + e \tag{3.4}$$

where: $\mathbf{y}$ is the vector of data points. A is the design matrix with a column of normalized indices and a column of ones. **c** is the vector of coefficients $[a, b]$. e is the vector of residuals

Using the normal equation of least-squares, the optimal coefficients **c** are found by:

$$\mathbf{c} = (A^T A)^{-1} A^T \mathbf{y} \tag{3.5}$$

After obtaining the coefficients, the linear trend $A\mathbf{c}$ is subtracted from the original data to obtain the detrended data.

3.2.3. Wave-by-wave analysis

Zero-down crossing

To perform wave-by-wave analysis, identification of single waves over the time series is the first steps. Zero-down crossing is most often used method to separate waves. In the experiment time series, where the signal is sampled at discrete time points t_i with values x_i, a zero-down crossing between two consecutive points t_i and t_{i+1} occurs if:

$$\begin{cases} x_i > 0, \\ x_{i+1} < 0, \end{cases} \tag{3.6}$$

In this experiment, the sample rate of each wave gauge is $200Hz$, in comparison to the wave frequency is in scale of $1Hz$, which can be consider large enough, hence, we directly use t_{i+1} as zero-down crossing points.

Average wave height

Let $\eta(t)$ be a continuous signal representing the surface elevation, and let $t_0, t_1, \ldots, t_n$ be the times at which zero-down crossings occur. t_p and t_t correspond to the time of the peaks and troughs of the surface elevation The wave height between consecutive zero-down crossings can be expressed as:

$$H_i = \eta(t_p) - \eta(t_t) \text{ for } t \in [t_i, t_{i+1}] \tag{3.7}$$

The average wave height $\bar{H}$ is then calculated as :

$$\overline{H} = \frac{1}{n}\sum_{i=x}^{n} H_i \tag{3.8}$$

where n is the number of waves (the number of zero-down crossing intervals). As the wavemaker begins operation, the wave gauge is activated simultaneously. Initially, there is a period of wave development until stability is reached. Consequently, the first x waves must be disregarded. Figure 3.11 displays the initial wave evolution, showing that a total of $x = 10$ waves are skipped before stability is achieved. Since the wave gauge deactivates as soon as the wavemaker is turned off, it is unnecessary

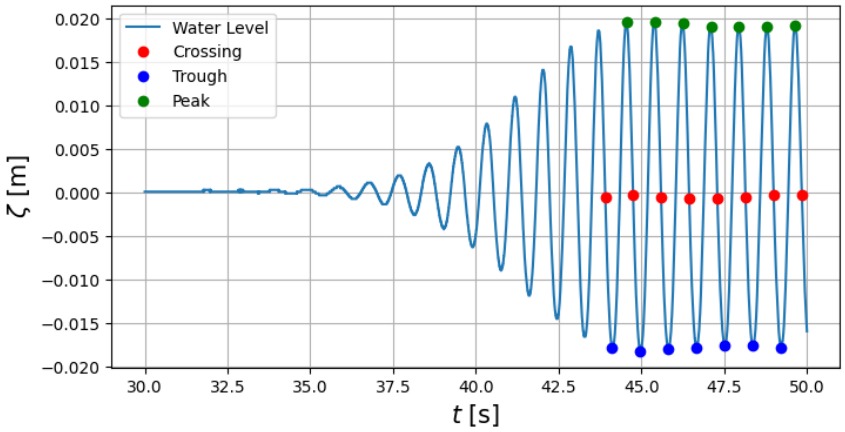

Figure 3.11: Wave evolution at the beginning of the wavemaker start.

to skip the final waves.
The zero-crossing point does not exactly coincide with zero due to the method used, which selects the first index where the water surface elevation goes from positive to negative. The displacement and velocity of water particles are $\frac{\pi}{2}$ out of phase; maximum velocity occurs at zero displacement. Despite our high sampling rate (200Hz), errors persist. Although not a true zero-crossing point, it is primarily used to determine the wave period, partially mitigating the error. Thus, these points are still reliable indicators. **Average wave period**
The wave periods T_i between consecutive zero-down crossings can be calculated as:

$$T_i = t_{i+1} - t_i \tag{3.9}$$

The average wave period $\overline{T}$ is then:

$$\overline{T} = \frac{1}{n}\sum_{i=x}^{n} T_i = \frac{1}{n}\sum_{i=x}^{n}(t_{i+1} - t_i) \tag{3.10}$$

Where $n+1$ is the number of zero-down crossings, and i denotes the index of the crossings.
Skewness and Asymmetry
The skewness formula Sk and As provides a normalized measure of the nonlinearty of the distribution of the signal η. By examining the third central moment normalized by the cube of the standard deviation, it captures the extent and direction of the nonlinearty. The skewness Sk and As of a water elevation series η according to **(author?)** [7] as:

$$Sk = \frac{\langle(\eta - \bar{\eta})^3\rangle}{\sigma_\eta^3} \tag{3.11}$$

where: σ_η is the standard deviation of η; $\langle\cdot\rangle$ denotes the mean for discrete datasets.

$$A_{s_\eta} = \frac{\langle\mathcal{H}(\eta - \bar{\eta})^3\rangle}{\sigma_\eta^3} \tag{3.12}$$

where where $\mathcal{H}$ is the imaginary part of the Hilbert transform.

3.2.4. Viscous wave attenuation

Since the wave gauge No.4 and No.5 in Fig.3.2 will be removed to minimize interruption of water flow in the area near Z-camera and PTV system, we use the data of wave gauge No.2 to represent the incoming wave statistics. However due to the attenuation affect, in reality the wave height is lower.

Therefore, a viscous wave attenuation fit is made to predict the real wave height near Z-camera and PTV system.
The amplitude as a function of time under internal friction is given in [8] as:

$$a_i(t) = e^{-2\nu k^2 t} a(0) = e^{-2\nu k^3 \Delta x/\sigma} a(0) \tag{3.13}$$

using $t = c\Delta x = k\Delta x/\sigma$. The dissipation of the amplitude due to friction with the side walls is given by [20]

$$a_w(t) = e^{-\alpha \Delta x} a(0)$$

with

$$\alpha = \frac{k}{W}\sqrt{\frac{2\nu}{\sigma}}\left[\frac{\sinh(2kh) + Wk}{\sinh(2kh) + 2kh}\right]$$

with W the width of the tank.

$$a_t(t) = e^{-2\nu k^2 \Delta x/\sigma} e^{-\alpha \Delta x} a(0) \tag{3.14}$$

According to table 3.2, the distance between WHG 2 and WHG 4 is $21.79 - 12.79 = 9m$

3.2.5. Reflection analysis

To evaluate the presence of excessive reflected waves in our wave flume experiments and validate the feasibility of the experimental setup, we employed the methodology delineated by Michael Isaacson [10].
Isaacson's approach involves three distinct methods that utilize fixed probes to measure the incident wave height, the reflection coefficient, and the reflection phase angle. In our study, we adopted Method III, which involves three fixed probes measuring the wave heights only. This method was selected for its simplicity and applicability in situations where phase measurements are impractical or inaccurate.

3.3. Spectral domain wave analysis

Discrete Fourier Transform (DFT) is used to convert the time-domain signal into the frequency domain.

$$X[k] = \sum_{n=0}^{N-1} \eta_w[n] e^{-i2\pi kn/N} \tag{3.15}$$

where: N is the number of samples. k is the frequency index. $X[K]$ represents the complex amplitude of the (k)-th frequency component.
Power Spectral Density (PSD) provides a measure of the power present at each frequency. It is computed as:

$$P[k] = \frac{|X[k]|^2}{N\Delta t} \tag{3.16}$$

Given a wave energy spectrum $S(f)$, where f is the frequency, the (n)-th spectral moment (m_n) is defined as:

$$m_n = \int_0^\infty f^n S(f)\, df \tag{3.17}$$

In practice, since wave spectra are often available as discrete data, the integral is approximated by a sum:

$$m_n \approx \sum_{i=0}^{N-1} f_i^n S(f_i) \Delta f \tag{3.18}$$

• (f_i) are the discrete frequencies.

• ($S(f_i)$) is the spectral density at frequency (f_i).

• (Δf) is the frequency interval.
H_{m0}, also known as the spectral significant wave height, is defined based on the zeroth moment of the wave energy spectrum ($S(f)$). The zeroth moment (m_0) represents the total energy in the wave spectrum. The significant wave height (H_{m0}) is calculated as:

$$H_{m0} = 4\sqrt{m_0} \tag{3.19}$$

T_{m01} (Mean Wave Period) is calculated using the zeroth spectral moment (m0) and the first spectral moment (m1) of the wave energy spectrum.

$$T_{m01} = \frac{m_0}{m_1} \tag{3.20}$$

T_{m02} (Energy Period) is calculated using the zeroth spectral moment (m0) and the second spectral moment (m2) of the wave energy spectrum.

$$T_{m02} = (\frac{m_0}{m_2})^{\frac{1}{2}} \tag{3.21}$$

3.4. Surface drift tracking

3.4.1. Z-camera experiment setup

As shown in Fig. 3.7, the Z-camera is located near the PTV system to track the surface drift.
In the experiment, the Z-camera will record videos at given time intervals: 5 min, 10 min, 15 min, 30 min, 45 min, 60 min, 75 min, 90 min, 105 min, and 120 min as Figure 3.9. Each video lasts 80 seconds to capture a sufficient number of waves. For simplicity, time references may be abbreviated later, such as using 't5' to represent 't = 5 minutes'.
Fig. 3.12 is a screenshot from the video $W1\_01$ (Here, '01' represents the experiment number of the repeated experiment). The yellow floating particles in figure 3.12 can be considered as tracers that are assumed to follow the free-surface fluid motion. As the wave propagates, these particles exhibit oscillatory motion, moving left and right periodically in response to the changing forcing induced by waves. Additionally, there is a net displacement of the particles due to the phenomenon of drifting. In this experiment, a tracking algorithm will be employed to monitor the movement of individual particles and fit the data to a linear model to determine the individual drift velocities. By averaging the drift velocities of all tracked particles, the overall drift velocity can be obtained for this specific time interval.
The calibration process consists of three main components: intrinsic calibration, extrinsic calibration,

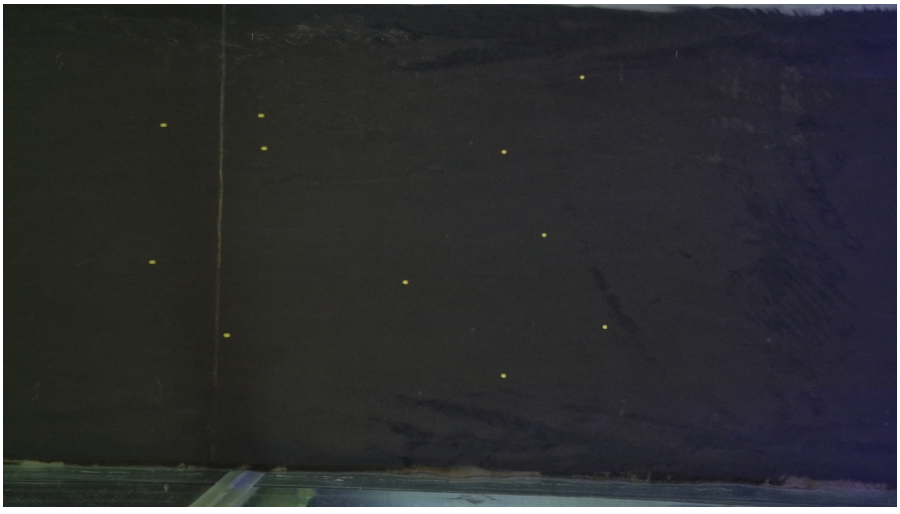

Figure 3.12: Screenshot of the videos in W1_01. The yellow dots is the tracer and the black surrounding is the black bottom in order to make tracers more visible

and parameters calibration.

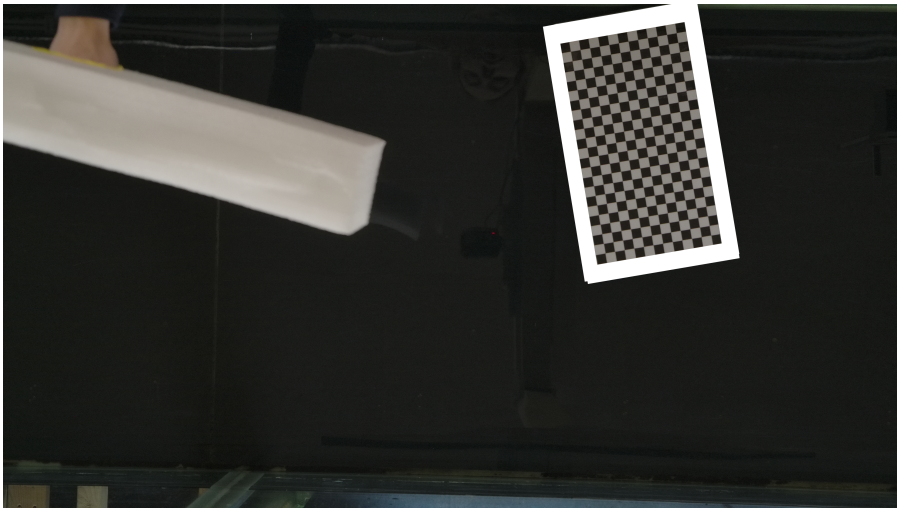

Figure 3.13: Intrinsic calibration

3.4.2. Intrinsic Calibration

This step focuses on determining the intrinsic parameters of the camera to model the internal geometry of the camera, including lens distortion. As shown in Fig. **??**, a calibration board is used to detect and correct for lens distortion by estimating the camera's intrinsic parameters such as focal length, principal point, and distortion coefficients. We capture 10-15 images of the calibration board from different angles and positions within the frame, ensuring that the entire field of view is well-sampled for accurate distortion correction.

Lens distortion, especially radial and tangential distortion, can affect the accuracy of measurements, particularly in the periphery of the image. Additionally, perspective distortion, caused by the varying distance between objects (e.g., particles) and the camera, affects how objects are perceived in a 2D image. For instance, due to the camera's perspective, particles may appear to move faster at wave peaks and slower at troughs. To mitigate perspective distortion, the camera is positioned 3 meters above the water surface, reducing the angle of view and minimizing the impact of perspective on the perceived particle velocity.

3.4.3. Extrinsic Calibration

After the Intrinsic calibration, local coordinate system is constructed, but the origin is arbitrary. Extrinsic calibration involves reconstructing the real coordinate system from original image and aligning the arbitrary origin with the real coordinate system of the wave flume. After this process, The relationship between the image unit (Pixel) and the real unit (mm) can be obtained.

3.4.4. Parameters Calibration

This step optimizes the use of existing yellow balls as tracking markers by ensuring accurate detection and tracking while minimizing errors from wall interference. To achieve this, the tracking region excludes the walls of the wave flume, thereby reducing disturbances caused by proximity to the walls. A restricted area with a 10-centimeter margin from both the upper and lower edges of the flume will be established, filtering out particles that fall outside this designated area.

Additionally, particles that cluster together during the experiment will be removed from the analysis. Clustering can distort tracking accuracy by causing overlapping trajectories and misleading velocity measurements. By filtering out such clustered particles, we enhance the overall precision of the tracking process and ensure more reliable measurements of individual particle motion within the flume.

3.4.5. Averaging method of Z-camera tracking

As shown in figure 3.16, after the tracking process, the displacement in time is obtaining with the component of periodic oscillations and net drift, as indicated by the solid line. A fitting linear line serves to extract the net drift, which shown as the dashed line. The slope of this net drift is the drift velocity of

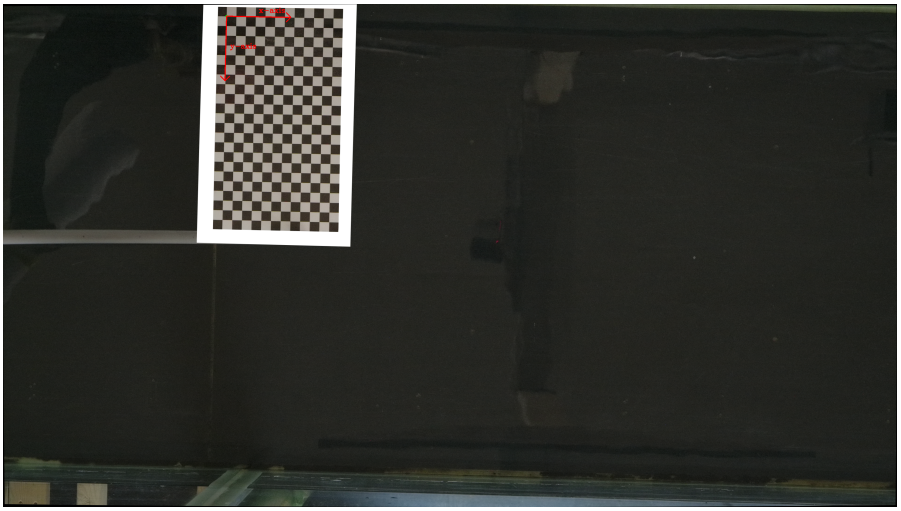

Figure 3.14: Extrinsic calibration

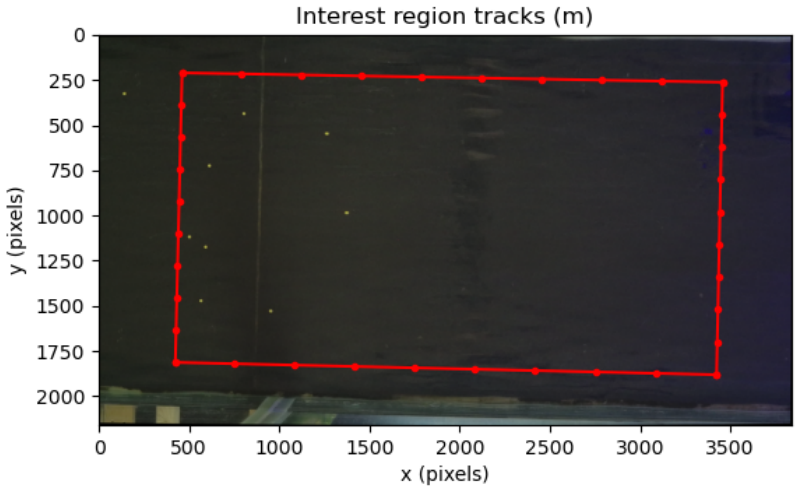

Figure 3.15: Z-camera's tracking restricted area to ensure that it is not affected by side walls. The relation between pixels and millimeter is 0.357 mm/pixel.

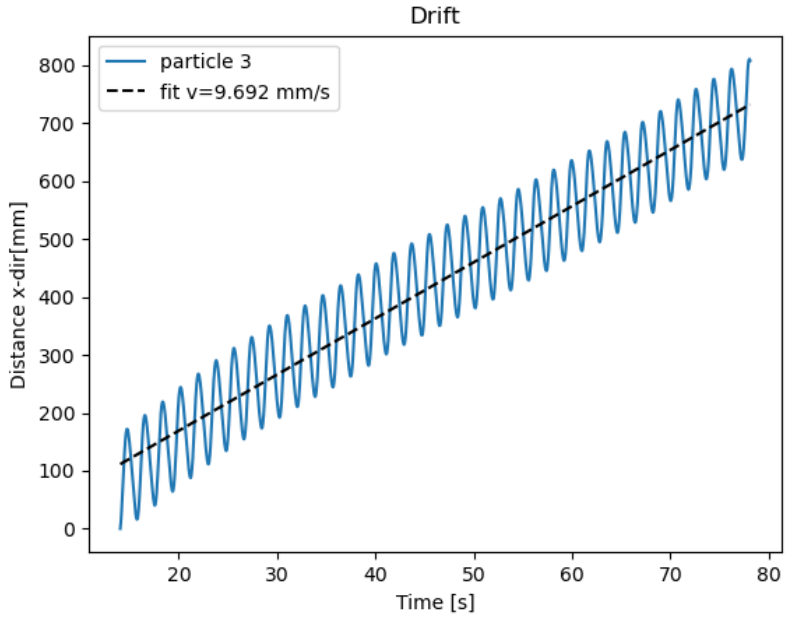

Figure 3.16: The position of the tracked particle by Z-camera in x-direction. The 'Distance' infers the distance between the current position and the lowest position of this particle. Solid line: the overall displacement of the pariticle, dash line: the fitting reuslts given by the program

this specific tracking ball. To minimize error from the non-integer part of the wave, the tracking particles must be selected so that their size is at least 15 times the wavelength.
With the above steps, the analysis of the drift velocity of a tracked particle can be completed. Then, by averaging all the tracking ball within the restriction area as figure 3.15, the averaged net drift at the surface can be obtained.

3.5. 3D PTV measrurements

3.5.1. Introduction to the PTV system

Particle Tracking Velocimetry (PTV) is a non-intrusive optical measurement technique used for visualizing and measuring fluid flow by seeding the fluid with tracer particles and optically tracking their motion over time. Utilizing LaVision's FlowMaster Shake-the-Box 3D PTV system, PTV offers higher resolution compared to traditional flow measurement techniques (e.g. ADV, EMS, LDA). It tracks individual particles in the flow field, providing quantification of a volumetric flow field, other than local measurements of the flow velocity with a point probe (ADV, EMS, LDA).
Additionally, as a non-intrusive optical method, PTV does not interfere with the flow, preserving ideal experimental conditions and eliminating disturbances caused by probes. The Shake-the-Box (STB) method, implemented via the Shake-the-Box software, facilitates time-resolved and three-dimensional particle tracking by automatically preprocessing the recorded particle data from the MiniShaker [22]. The STB method allows high-density particle tracking without ghost particles, providing higher accuracy, better resolution of small-scale flow features, and enabling Lagrangian analysis of flow fields.

3.5.2. Experimental Setup for PTV

Figure 3.17 is the top view of the setup of the PTV system which includes the following components:
LED Source: A LED light source is used to illuminate the flow. Two boxes were used to provide enough light, each LED box measuring 30cm $\times$ 10cm.
MiniShaker: Four high-speed cameras (Imager M-lite 2M) are positioned at fixed angles to capture particle movements, centered at a distance of 50 cm from the middle of the measurement volume. The measurement volume has a certain thickness, allowing the cameras to capture particle movements

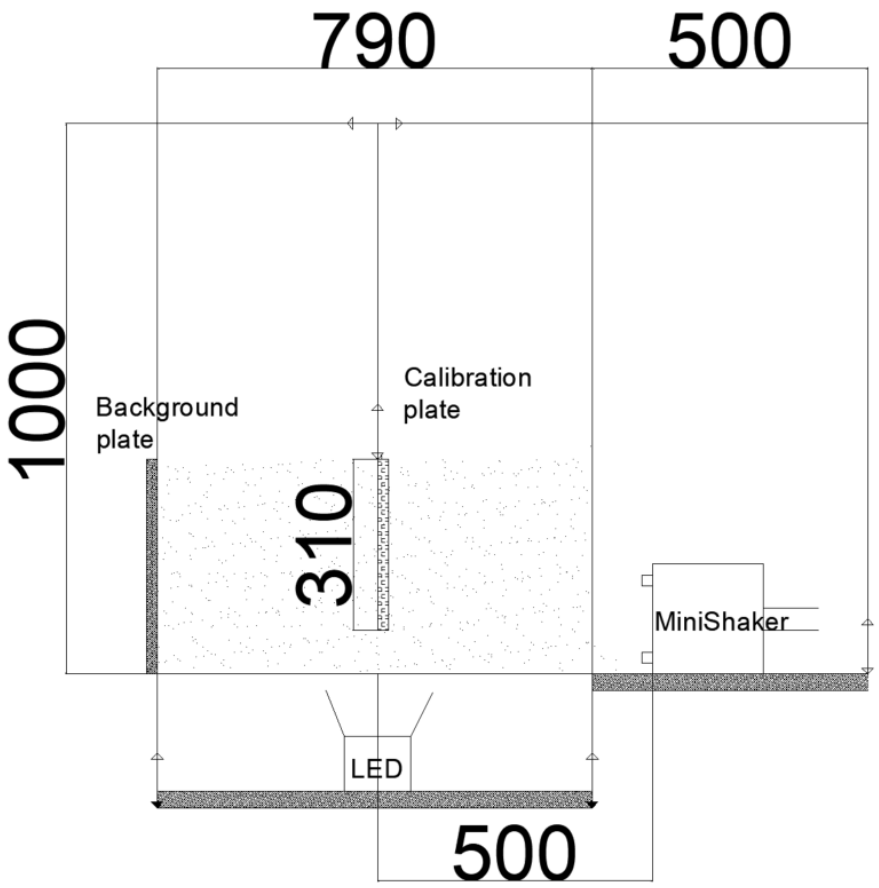

Figure 3.17: The conceptual sketch for the calibration of PTV . The scales are in mm and the wave propagating direction is poingting inside the figure.

throughout the full three-dimensional space. The cameras have a resolution of 1920x1280 pixels and a frame rate of 100 frames per second. The lenses used for these tests are the 8 mm set.
Light Blocking Curtains: Light blocking curtains play a crucial role in the PTV system by preventing interference from external light sources (such as sunlight or indoor lighting), enhancing image contrast and clarity, reducing reflection interference, and controlling experimental ambient light.
Calibration plate: The Calibration are used to calibrate and reconstruct the coordinate system inside the flume prior to the wave experiment. The calibration process follows the instruction of *Product Manual of FlowMaster Shake-the-Box (4D PTV)*.
Particle Seeding: Hollow plastic spheres with a diameter of 15 micrometers and a density of 1.00 g/cm³ are seeded into the fluid. These particles are selected for their neutral buoyancy, ensuring that they follow the fluid motion without sinking or floating, which is critical for accurately tracking the flow. Their high reflectivity enhances visibility under the system's lighting, allowing for precise particle tracking and measurement.
Data Processing Software: LaVision's FlowMaster Shake-the-Box system is used for system configuration, pre-experiment verification, and analysis of experimental data.

3.5.3. PTV calibration procedure

The calibration procedure can be divided into two parts: Volume Calibration and Self Calibration. For more detail, please refer to *Product Manual of FlowMaster Shake-the-Box (4D PTV)*.
Volume Calibration involves calibrating the camera, not only for the mapping of a single xy world plane to the camera's view, but also for the z-dependence of the mapping from a world point to the camera chip. This is achieved using a 3D calibration board (Figure 3.8b) placed at the center of the view. Five photos are taken at different positions along the z-axis. The software then performs calibration using 3rd-order polynomial interpolation between multiple distances of the board.

For Self Calibration, the flume volume is seeded with particles. The software automatically computes and corrects any errors in the Volume Calibration. This process is repeated until the calibration error is less than 1 pixel per side (each seeding particle takes approximately 4 pixels per side).

3.5.4. Settling Velocity and background motion

Stokes' Law provides a method to calculate the terminal settling velocity of spherical particles at rest when the particle diameter is less than $0.1mm$[5] [24]. The law is expressed as follows.

$$v_s = \frac{(\rho_p - \rho_f)gd^2}{18\mu} \tag{3.22}$$

where v_s is the settling velocity, ρ_p is the particle density, ρ_f is the fluid density, g is the acceleration due to gravity, d is the particle diameter, and μ is the water viscosity.
For this calculation:

- Particle density (ρ_p) = $1000kg/m^3$
- Fluid density (ρ_f) = $999.126kg/m^3$ (water at $15 \circ C$)
- Acceleration due to gravity (g) = $9.81m/s^2$
- Particle diameter (d) = $15 \times 10^{-6}meters$
- Fluid viscosity (μ) = $0.0013Pas$

This reveals the theoritical settling velocity of the seeding material will be: $v_s = 1.0723 \times 10^{-4}$ mm/s
In ideal situation, before the wave-make starts, the water in the flume is completely still. However, in reality, the flow in the interior of the water is never still, and the subtle flow is always there because of the small disturbance and the low-frequency component, which is not easy to dissipate. Another important reason is the particle settling or floating. As calculated in Section **??**, the settling velocity of the selected seeding material is negligible because it is much smaller than the fluid flow velocity. Therefore, its effect on the motion of the particles can be ignored. However, due to the manufacturing process, the seeding material is not entirely homogeneous, meaning that some particles may differ in density or shape, causing them to either sink or float. While this could contribute to background motion, it is also possible that long-period motions slowly damping out in the flume are responsible for some of the observed background motion.
In experiments, the background motion of the particle will never been known in advanced. But the initial motion before the wave arrived at the windows of the PTV system can be inspect in $t0$ shown in figure 3.9. By checking the initial motion, the background motion will be known from post-processing.
To minimize the size of the background motion, we keep the water in the flume as still as possible and maintain a completely uniform temperature throughout the water. We allow sufficient time between each experiment to manage these processes. In this case, we have a 30-minute interval between each experiment.

3.6. Lagrangian velocity calculation for PTV system

3.6.1. Particle Selection Scheme

The software (Shake the Box) is able to export the information of every tracked particle (3-dimension position and the temporary information). However, not all tracked particles provide information with lower errors. Therefore, suitable particle selection scheme is provided first.
Since particle acceleration is theoretically corrected during calibration, tracking errors tend to increase as the particles move further from the calibration board's position. This leads to lower confidence in particle tracking accuracy at the edges of the field of view. Particles near the edge of the camera's view are not desirable, as they can cause significant errors in tracking. Therefore, in the x-y plane, 150mm from the center of the view to both edges will be restricted as the Red square area in figure 3.18a. For the y-z plane, restriction also need to be employed. Away from the centre, 3-dimensional vorticity will occur and 2-dimensional motion condition would not be applied, hence, the particle in the small area from the middle is selected. 60mm from the center of the view to both edges in the y-z plane will then be restricted to prevent the affect of the side walls effect as shown in figure 3.18b. Also, it can be seen that the field of view of the PTV is located in the center of the water column, and part of the region below

the wave trough and above the bottom of the water (including the boundary layer) is outside the field of view. Therefore, we are unable to obtain velocity data outside part through the PTV system. The part of the water depth uncovered is varied by wave conditions, but generally, the coverage is large. The detailed coverage area is shown in 4.3.6

In spectrum domain of the velocity time-series, the inspected flow's frequency range generally extends

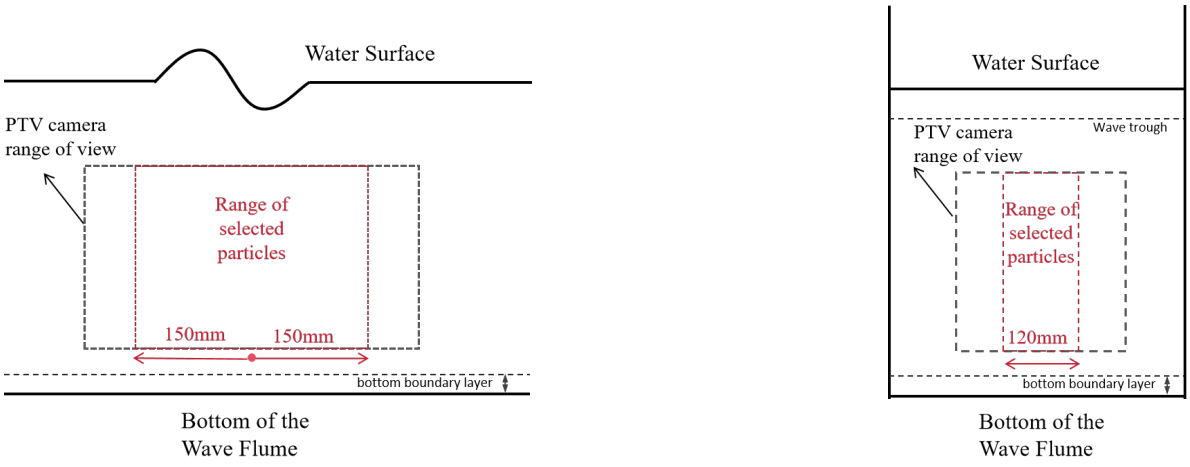

(a) x-y Plane **(b)** y-z Plane

Figure 3.18: Area of the PTV camera range of view and the particle selected area

from 0 (linear motion) to f_p (peak frequency); the higher frequencies observed in the experiment are caused by noise or other high-frequency, small-scale turbulence, which appears as some irregular bias in the time domain. Particles with too short a tracking duration may result that the high-frequency noise will not be averaged out and eliminated and thus not taken into account. To ensure that the particle tracking duration is long enough to ignore the bias caused by high-frequency noise, criterion ϵ based on the tracking duration is proposed. A rough estimate of this criterion suggests that particles with a time duration longer than $15 \times T_p$ are selected for calculating the Lagrangian mean drift. Table 3.3 shows the value of the criterion for each wave condition.

Table 3.3: Table showing T_p, δ of each wave condition

	T_p (s)	ϵ (s)
W1	1.81	27.08
W2	1.41	21.08
W3	1.21	18.08
W4	1.41	21.08
W5	0.85	12.82

3.6.2. Lagrangian periodic motion

Before introducing the Lagrangian averaging method, the Lagrangian periodic motion should first be determined. Because both Z-camera particle tracking program and PTV system track the displacement in a Lagrangian frame, it is important first to identify the peaks or troughs of the first-order motion (wave oscillation) of the tracked particles. Figure 3.19 shows the tracked results of the particles by PTV system based on the displacement of one particle. Periodic motion can be identified in the results of PTV system. It should be noted that the particle tracking results is a series of continuous oscillations which include single waves. In order to split the whole trajectory into wave-by-wave Lagrangian periodic motion, the peaks and troughs of the plots are identified, which will serve as the delimiter between two successive waves, from which the streamwise location and corresponding time-instances are obtained. The complete trajectory with the Lagrangian periodic delimiter can then be obtained, as shown in Figure 3.20. Note that in this PTV system, the 'y' recognized by the software refers to the coordinates in the vertical depth direction, with the origin pointing from the bottom to the surface of the water, so that

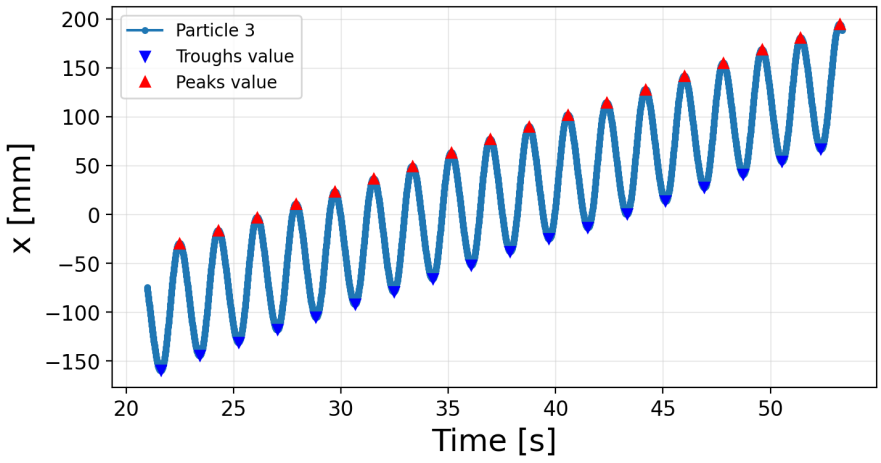

Figure 3.19: The position of the tracked particle by PTV in x-direction. Blue △ : the exact position of each troughs value, Red △ : the exact position of each peaks value

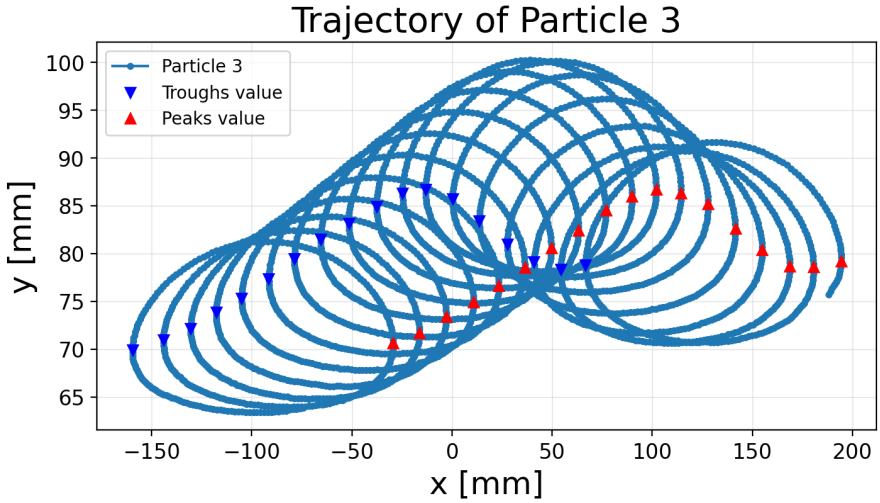

Figure 3.20: The trajectory of an example particle.

hereafter 'y' represents the depth direction, and z represents the cross wave flume direction. It is different from the previous. After getting the Lagrangian periodic delimiter, the data before the first delimiter and after the last will be discarded, since the remaining incomplete parts of the trajectory will introduce an error in the calculation of the velocity.

3.6.3. Particle Averaging method

3.6.4. Averaging method of PTV system

The averaging method is more complex than the Z-camera because the effective particles tracked through the PTV system can be roughly 4-5 times more than those tracked through the buoyant sphere at the surface and its due to the fact that the particles are smaller in diameter and are likely to undergo not only lateral movement, but also vertical net displacement. A tracked particle may be displaced vertically by a large amount during oscillation, and at this point the exact depth represented by the particle is difficult to define. For particles with large vertical displacements, if the average depth is simply taken, then there may be a relatively large error. For this case, various methods will be considered, the first one is mainly to take a time average and filter out the particles with excessive vertical displacement (Time-averaged), the second one is to split the particle trajectories according to the Lagrangian period in order to refine the net drift trajectory (Wave-by-Wave averaged), and another one is to filter out the high-frequency component by using low-pass filters to obtain real-time trajectories of particles at low

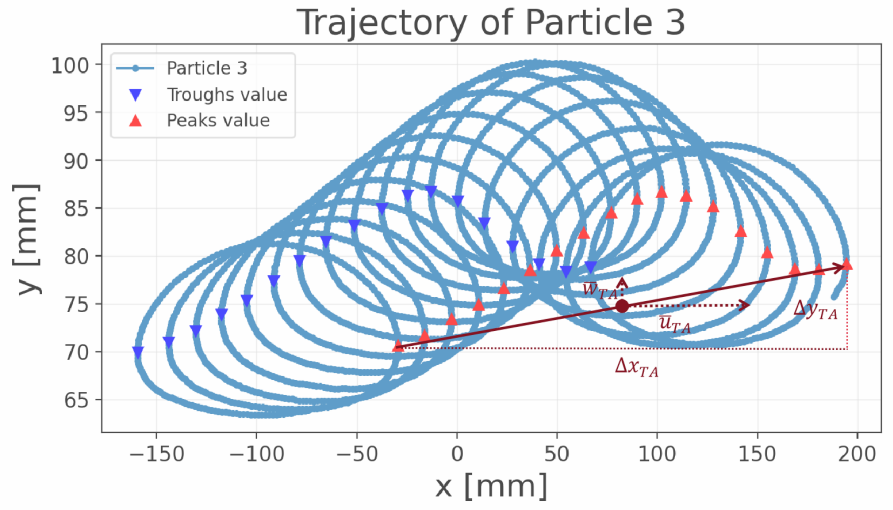

Figure 3.21: Illustration of the time-averaging method. → : The averaging displacement with direction, Δx_{TA}: The displacement in x-direction, Δy_{TA}: The displacement in y-direction, $\overline{u}_{TA}$ the velocity vector of the x-direction averaging velocity, $\overline{w}_{TA}$ the velocity vector of the y-direction averaging velocity

frequencies (Low-pass filter).

Time-averaging Method

The time-averaging method for obtaining the mean Lagrangian drift necessitates monitoring the trajectory of water particles across successive wave cycles to quantify their average displacement. This is achieved by documenting the positions of tracer particles between the start and end of the track, taking only the tracks longer than the δ in table 3.3, computing their displacements, and subsequently averaging these displacements over several wave periods to isolate the resultant net drift.

The time-averaged displacement over a time duration ΔT is given by:

$$\overline{\Delta x} = \frac{1}{\Delta T}\int_0^{\Delta T} \Delta x(t)\, dt, \Delta T = n \times T_L \tag{3.23}$$

Where $n = 1, 2, 3, ...,$ T_L is the Lagrangian period in Lagrangian frame.

Then the mean Lagrangian drift velocity $\overline{U}$ is:

$$\overline{u}_{TA} = \frac{\overline{\Delta x}_{TA}}{\Delta T} \tag{3.24}$$

An example of the time-averaging method is shown in Figure 3.21. We used the entire trajectory data (in this case, n = 18) to average. The time-averaging results show a displacement vector from the initial point to the last point, and in this case, this representative position (hence depth) of the averaged trajectory will be at the midpoint of this displacement vector. The velocity vectors in the x-direction as well as in the y-direction are also calculated by this time-averaging method. Finally, we keep only particles that are within a reasonable range by filtering out particles whose vertical displacement Δy_{TA} is too large. After adjusting, we set the limitation be $\Delta y_{TA,max} = 20mm$

Wave-by-Wave Method

The time-averaging method averages over the entire duration, which can also averaged out the turbulence in the net displacement. The wave-by-wave scenario takes into account all periodic wave motions. By obtaining the displacement vector by every two successive periodic diameter, more resolution can be obtained by using this approach, as shown in Figure3.22.

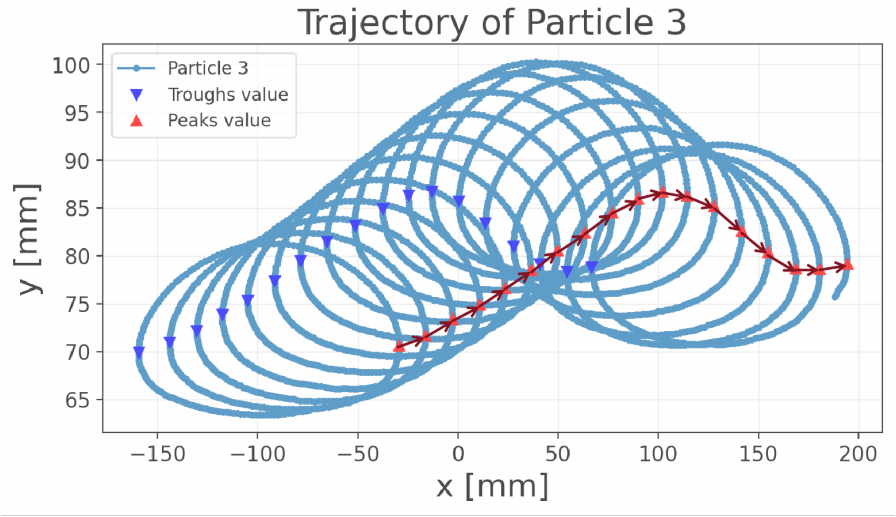

Figure 3.22: Illustration of the wave-by-wave method

Low-pass frequency filtering

To separate the consistent movement of particles and reduce the effect of wave-induced periodic motions, the low-pass frequency averaging technique is used to determine the Lagrangian drift. This approach entails removing high-frequency components of the particle motion, which are mainly linked with wave-induced oscillatory motion, and concentrating on the lower-frequency components that indicate the net drift. The steps are as follows:

1. Fourier transform: The Fourier transform is applied to the time series data of the particle positions:

$$X(f) = \int_{-\infty}^{\infty} x(t) e^{-i2\pi ft}\, dt \tag{3.25}$$

2. Low-Pass Filtering: A low-pass filter is applied to the frequency-domain data:

$$\widetilde{X}(f) = H(f) \cdot X(f) \tag{3.26}$$

where $H(f)$ is the low-pass filter function defined as:

$$H(f) = \begin{cases} 1 & \text{for } |f| \leq f_c \\ 0 & \text{for } |f| > f_c \end{cases} \tag{3.27}$$

3. Inverse Fourier Transform: The inverse Fourier transform is applied to the filtered data. This transforms the frequency domain data back into the time domain, now with the high-frequency oscillatory components removed. The resulting time series represents the low-frequency motion of the particles:

$$\widetilde{x}(t) = \int_{-\infty}^{\infty} \widetilde{X}(f) e^{i2\pi ft}\, df \tag{3.28}$$

For different wave types, different f_c are required, in order to completely filter out the first-order frequency component. A sufficiently low f_c should be chosen while at the same time the cutoff frequency should be as high as possible in order to prevent the loss of some low-frequency information. Once adjusted, f_c is most effective when it is between 0.1 and 0.3 times the peak frequency f_p. Figure 3.23 shows the cut-off frequency selection scheme, f_c should be away from the first-order frequency component and should not influence the low-frequency component. By using the low-pass filtering method, a filtered trajectory can then be obtained (Figure 3.24). Theoretically, the full derivatives of the filtered trajectory with respect to time is the velocity after averaging.

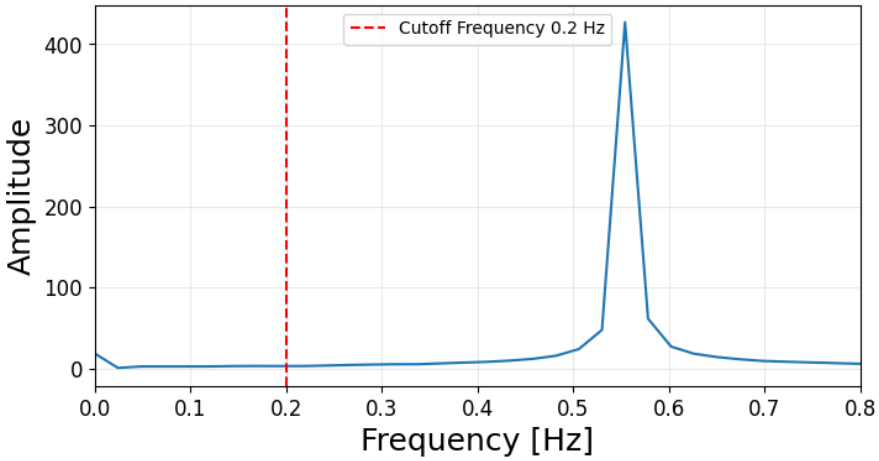

Figure 3.23: Example frequency spectrum of W1

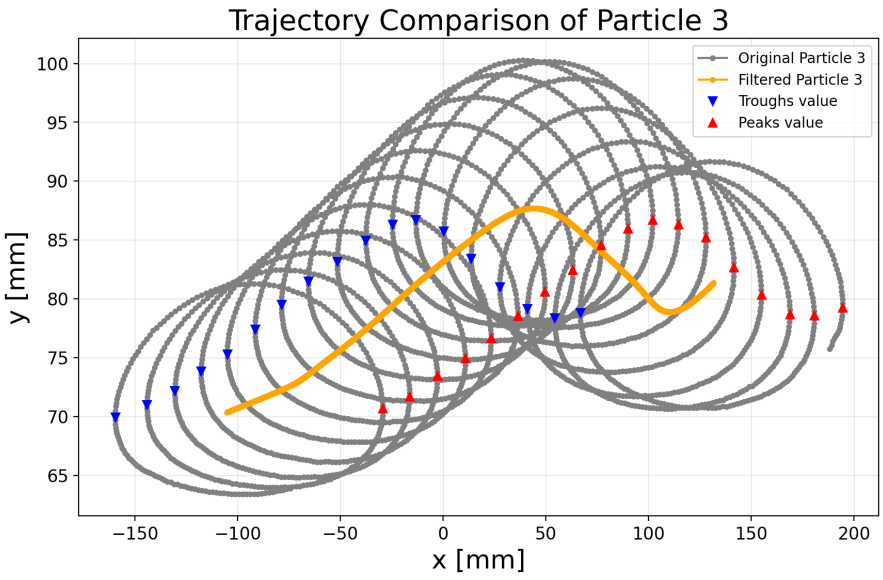

Figure 3.24: Illustration of the low-pass filtering method

The vertical direction coordinate in the velocity profile
Assuming the particle's initial coordinate in the depth direction is y_0, after time Δt, the particle may experience a displacement in the depth direction, resulting in a new coordinate y_t. This displacement is denoted as $\Delta y_{TA} = y_0 - y_t$, as shown in Figure 3.21. However, when reacting to the velocity profile, we must have a definite depth coordinate y_L. Typically, we use $y_L = \frac{1}{2}(y_t + y_0)$, the average depth coordinates of the initial and ending moments. Different methods have different definitions for y_0 and y_t. For the time-averaged method, y_0 and y_t represent the initial and ending positions of the tracked particles, and for the wave-by-wave method, y_0 and y_t represent the position of each segment from the zero position of the displacement to the position of the next zero position after one Lagrangian period. And for the low-pass method, we divide the entire water depth into 20 bins, and all Lagrangian drift velocities within the depth range of each bin belong to the centre of this bin.

3.6.5. Velocity calculation and uncertainties

With the ShakeTheBox software, we can analyze the exact position of each particle in 3 dimensions with time resolution. After obtaining the specific position at each moment, we use the central difference method to calculate the displacement velocity of the particle.
Suppose we have information about the position of the particle at different points in time, which can be expressed as $x(t_i)$, and t_i means the i^{th} time point. The time difference with two successive positions will be $\Delta t = \frac{1}{f_s}$, where the sample rate f_s in our case is $100Hz$. Then the central difference gives

$$v(t_i) \approx \frac{x(t_{i+1}) - x(t_{i-1})}{2\Delta t} \tag{3.29}$$

Suppose we have N points, notice that at the boundary when $i = 1$ and $i = N$, there will not be a solution. Given that the sample data is sufficient enough, then the data at the boundary will be discarded. Then we consider the uncertainty of the calculated particle velocity. Given the uncertainty of the position (δx), the partial derivatives with respect to $x(t_{i+1})$ and $x(t_{i-1})$:

$$\frac{\partial v}{\partial x(t+\Delta t)} = \frac{1}{2\Delta t}, \quad \frac{\partial v}{\partial x(t-\Delta t)} = -\frac{1}{2\Delta t} \tag{3.30}$$

The uncertainty in velocity δv is:

$$\delta v = \sqrt{\left(\frac{\partial v}{\partial x(t+\Delta t)}\delta x(t+\Delta t)\right)^2 + \left(\frac{\partial v}{\partial x(t-\Delta t)}\delta x(t-\Delta t)\right)^2} \tag{3.31}$$

Substituting 3.30 gives:

$$\delta v = \sqrt{\left(\frac{1}{2\Delta t}\delta x(t+\Delta t)\right)^2 + \left(\frac{-1}{2\Delta t}\delta x(t-\Delta t)\right)^2} \tag{3.32}$$

Assuming the positional uncertainties at the two time points are the same, we get:

$$\delta v = \sqrt{\left(\frac{1}{2\Delta t}\delta x\right)^2 + \left(\frac{-1}{2\Delta t}\delta x\right)^2} \tag{3.33}$$

After further simplifying the equation 3.33, we get the final expression of the uncertainty:

$$\delta v = \frac{\delta x}{\Delta t} = f_s \delta x \tag{3.34}$$

Equation3.34 is a function of spatial uncertainty δx and sample frequency $f_s = \frac{1}{\Delta t}$. Further analysis will be performed in the section 4.3.1

3.7. Vorticity of the velocity profile

In a two-dimensional flow, the velocity field can be expressed as $u(x, y)$ and $v(x, y)$, where $u(x, y)$ denotes the transverse velocity component of the flow field (x direction) and $v(x, y)$ denotes the longitudinal velocity component of the flow field (y direction).
The vorticity ω is the vorticity of the velocity field, and in the two-dimensional case, the non-zero component of the vorticity is only in the z direction, and its expression is:

$$\omega_z = \frac{\partial v}{\partial x} - \frac{\partial u}{\partial y} \tag{3.35}$$

However, to simplify the calculations, in the flume, the length of the flume (39m) is significantly greater than the depth of the water (0.35m), and therefore the velocity profile in the direction of wave propagation is significantly greater than that in the vertical direction, which is also recognised in 4.3.6. The velocity profile in the direction of wave propagation is significantly greater than that in the vertical direction. If the velocity in the vertical direction is neglected, then Equation 3.35 can be written as:

$$\omega_z = -\frac{\partial u}{\partial y} \tag{3.36}$$

Therefore, after obtaining the velocity profile, the profile of the vorticity is obtained through Equation 3.36.

4

Results

This chapter presents the findings of the study, structured into three key subsections. In Section 4.1, important wave parameters such as height, period, and energy distribution are examined, along with assessments of wave attenuation and reflection. Section 4.2 analyzes the result of Z-camera and surface drift velocity over time. Finally, Section 4.3 evaluates the results from the PTV system, analyzing the velocity profiles obtained, as well as the corresponding vorticity profiles.

4.1. Wave analysis

4.1.1. Wave Statistics

The figure 4.1 shows the example of the water surface elevation recorded at WGH 2, which represents the 'offshore' wave condition for this experiment. Table 4.1 presents each wave statistic. Table 3.1 shows the real offshore condition measured, which is in consistence with the forced value with negligible deviation. W1 and W2 show large Sk, meaning the wave is skewed most. On the other hand, W5 is less skewed in comparison to others. In these five sets of experiments, all values of As are closed to zero at offshore condition, meaning that the wave asymmetry can be neglected.

Table 4.1: Wave statistic of the five wave condition used in this experiment, as measured at WGH 2. H_p: Average Peak Wave Height; T_p: Average Peak Wave Period; Sk: Non-dimensional Wave Skewness; As: Non-dimensional Wave Asymmetry; ka: Non-dimensial Wave Steepness; kh: Non-dimensional Water Depth; Forced ka: Forced Non-dimensional wave steepness calculated from the input wave parameters in Table 3.1

Wave	H_p (m)	T_p (s)	Sk (-)	As (-)	ka (-)	kh (-)	Forced ka (-)
W1	0.102	1.81	0.62	0.041	0.103	0.709	0.102
W2	0.125	1.41	0.57	0.031	0.171	0.959	0.179
W3	0.055	1.21	0.21	-0.012	0.092	1.175	0.101
W4	0.065	1.41	0.27	-0.096	0.089	0.959	0.096
W5	0.037	0.85	0.14	-0.020	0.107	1.999	0.115

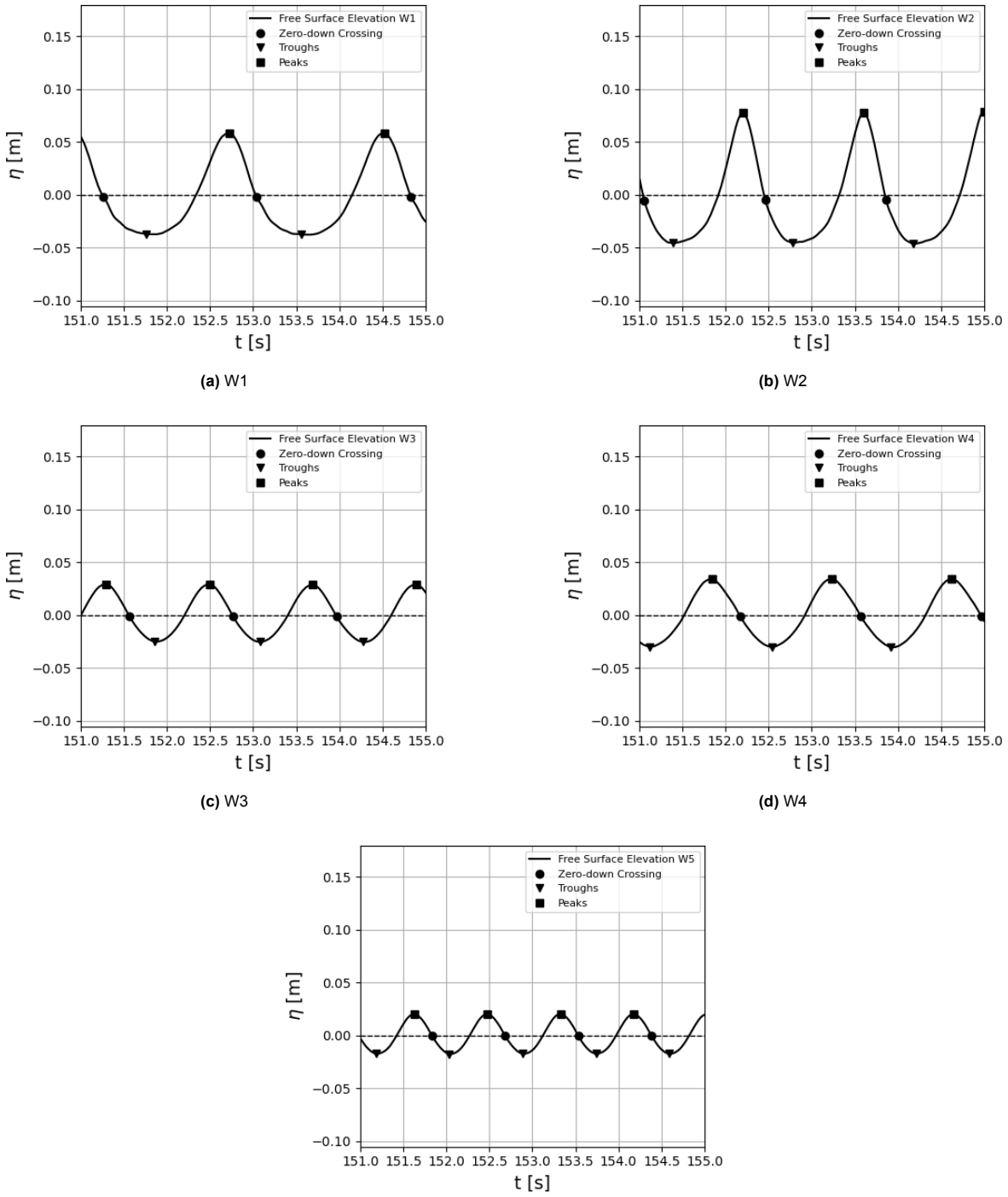

(a) W1

(b) W2

(c) W3

(d) W4

(e) Enter W5

Figure 4.1: Example of the time series of the free surface elevation of each wave condition offshore (WGH 2)

4.1.2. Spectral Analysis

In the Power Density Spectrum (PDS), the frequency domain analysis provides information on the wave components present in the wave flume. As illustrated in Figure 4.2, the PDS of W1 demonstrates a pronounced peak around 0.7 Hz at all wave gauges. This peak marks the dominant frequency component where the wave energy is concentrated. Beyond 0.2 Hz, the PDS values typically decrease and remain at a trough until they reach the dominant peak at 0.7 Hz. Past the 0.7 Hz peak, the PDS values decline sharply, suggesting minimal energy content at frequencies higher than 0.7 Hz.

When comparing the non-detrended and detrended data, the non-detrended data exhibit significant power near 0 Hz, which is not observed in the detrended data. This discrepancy indicates the presence of a linear trend in the surface elevation, potentially due to water leakage or wave gauge movement, which confirms the need for a detrending process. Furthermore, a comparative analysis of the wave gauges reveals that from WGH 1 to WGH 7, where the wave is not breaking yet. However, wave attenuation is also noticeable at these wave gauges as the peak PSD keep decresing from WGH 1 to WGH 7. To comprehensively evaluate the influence of attenuation, a detailed wave attenuation estimation will be conducted in the subsequent section.
However, at WGH 9 and WGH 10, due to the wave starting to break earlier, a decrease in peak frequency energy is observed along with an increase in background energy. This increase in background energy results from wave breaking, which causes energy to dissipate from the peak into the background. However, no secondary peak formation is observed, indicating that the waves still consist of monochromatic waves.

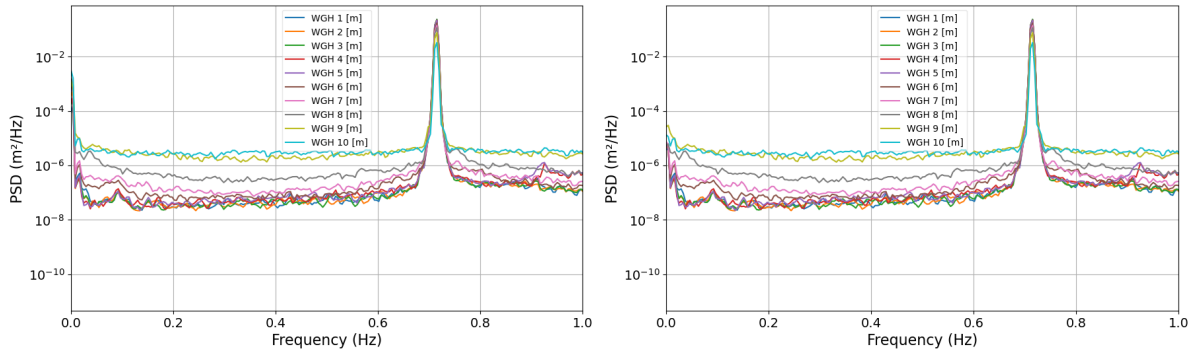

(a) Undetrended data

(b) Detrended data

Figure 4.2: Power Density of W1 with the different wave gauges

4.1.3. Wave attenuation estimation

The wave attenuation in the wave flume can be estimated as described in Section 3.2.4. The distance from WGH 2 (offshore wave condition) to WGH 4 (the nearest wave gauge to PTV and Z-camera) is 9.00 m. However, to minimize disturbances caused by the probe near the PTV and Z-camera, WGH4 were removed for the last two repeats. Therefore, predicted data accounting for viscous attenuation is used in the subsequent analysis. Figure 4.3 illustrates the measured and predicted results of H_{m0}. Furthermore, Figure 4.3 shows the differential values of H_{m0} between WGH 2 and WGH 4, as well as the predicted and observed values at WGH 4.
The results clearly indicate that attenuation causes a reduction of approximately 1-4 mm in wave height between WGH2 and WGH4. This attenuation varies with different wave conditions and increases with rising wave steepness. Although the predicted values differ slightly from the actual conditions, the discrepancy is generally below 1 mm. Thus, the predicted values demonstrate good agreement with the observed results, and will be used to obtain the wave height near the PTV and Z-camera measurement when WGH 4 and 5 are absent.

4.1.4. Reflection analysis

In Section 3.2.5, the three-wave-gauge method is used to estimate the reflection wave component. Table 4.2 shows the analysis results of each wave gauge. The result shows a low reflection coefficient of all wave conditions. The amplitude of the reflection wave is roughly 20 times smaller than the incident wave, which means the reflection is negligible. Hence, the reflected wave signal will not be taken into account in the following analysis.

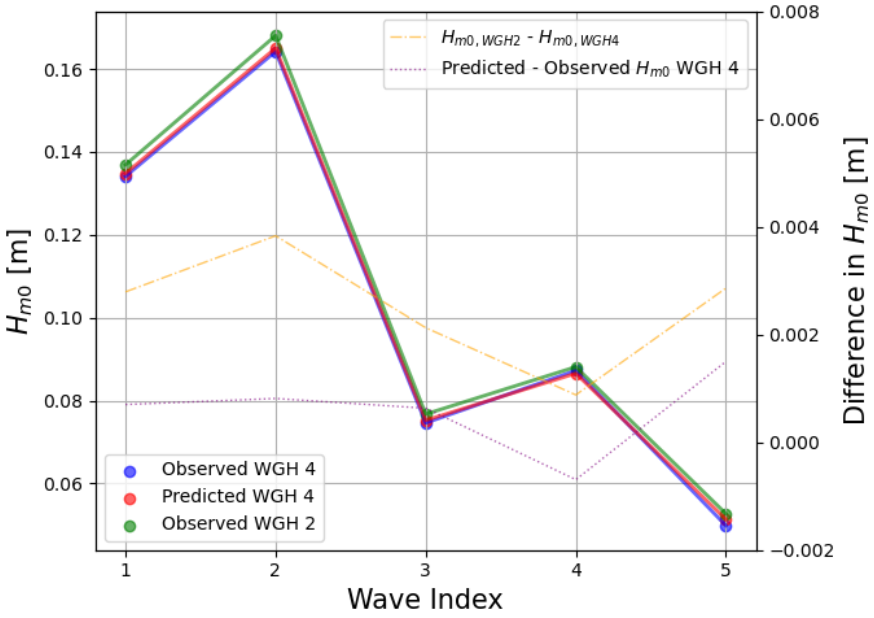

Figure 4.3: H_{m0} at WGH2, WGH4 and predicted WGH4 (solid line) and difference between the H_{m0}(dash line)

Table 4.2: Reflection analysis. a_I: incident wave amplitude; a_R: reflection wave amplitude; $R = \frac{a_I}{a_R}$

	f_p[s^{-1}]	a_I[m]	a_R[m]	R
W1	0.556	0.036	0.0012	0.033
W2	0.714	0.057	0.0012	0.020
W3	0.833	0.027	0.0006	0.022
W4	0.714	0.030	0.0006	0.021
W5	1.177	0.018	0.0010	0.056

4.2. Surface drift measurement

4.2.1. Reliability check of the tracking program

To validate the surface drift observation data, it is necessary to verify the reliability of the tracking results for each individual time slot recorded by the Z-camera. For each wave run, there are multiple recording time slots (t5, t10, t15...), and Figure 4.4 presents the mean particle count at the surface, as tracked by the code. The x-axis label denotes wave experiment ID. The Figure 4.5 shows the average value of the particle tracking duration, but expressed in terms of the wave count, e.g. the unit means that the particle tracking duration contains 1 wave period. The figure demonstrates that for each experiment ID, the averaged particle count from different experiment running is all larger than 8 and the overall tracking duration is higher than 20 waves, the bias earlier evaluating in Section 3.6.3 will be low enough. Overall, a sufficient number of particles were tracked within the restricted region, and the duration of tracking for each particle was adequate. These conditions ensure that the results are representative of the flow field.

However, the results represent the entire run, averaged over all time slots. It is necessary to check the tracking quality of each individual time slot to ensure the reliability of the Lagrangian drift results for the corresponding time periods. A comprehensive assessment was conducted for all time slots. The results are presented in Appendix A. Most of the particle counts for specific time slots exceed 8, except for *W1_05_t30* and *W3_01_t5*. And the tracking duration for all experimental conditions and time slots is at least 15 waves. The data indicate that the majority of tracking outcomes exhibit an a sufficient quantity of particles tracked and prolonged tracking duration. Nevertheless, the experiment IDs *W1_05_t30* and *W3_01_t5* yielded unreliable results as the camera failed to track the floating particles because of technical issues. Consequently, these data points will be excluded from the subsequent analysis.

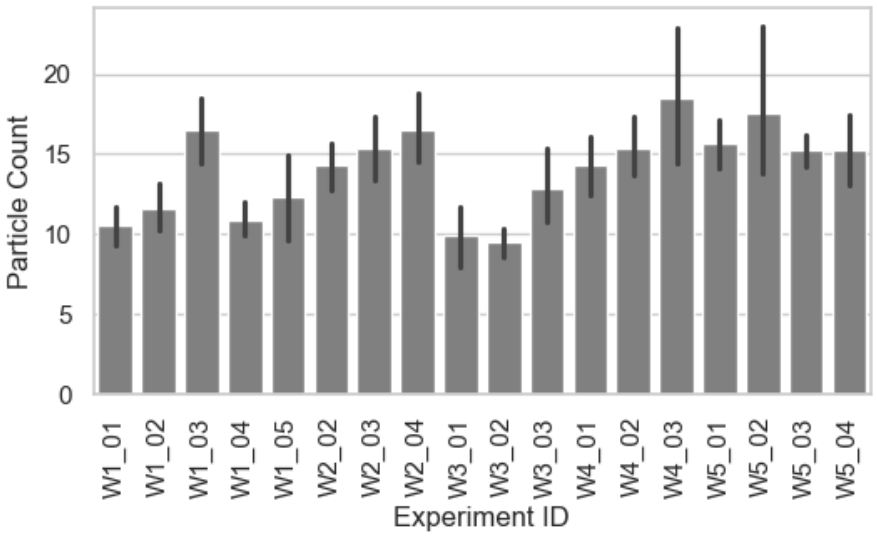

Figure 4.4: Average Particle Count. 'W' here means the wave condition, and the number after the underline represents the number of the repeated experiment

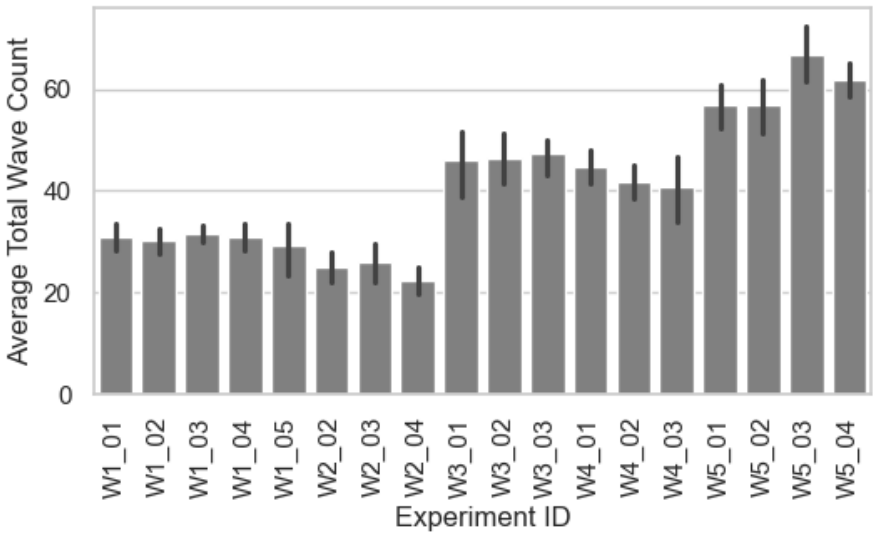

Figure 4.5: Average Wave Count.

4.2.2. Time results and drift toward equilibrium

Figure 4.6 shows the observed surface Lagrangian drift velocity over time. The y-label represents time-averaged surface drift velocity. The scatter points are observations, and the red line is the theoretical Stokes drift. Exponential fits illustrate the trends in drift velocity over time.

Under all wave conditions (W1, W2, W3, W4 and W5), the experimental results show a similar pattern. The repeated experiment follows the trend and have low standard deviation, indicating a good repeatability. The measured surface drift velocity is always smaller than the theoretical surface Stokes drift (shown as the plain red line). It is, however, close to the theoretical value at the beginning of the run (t5) for W5, which represents the deepest wave conditions. A stabilization process of the drift is observed in all waves. Different wave condition shows a different stablization time, but after 60 min, all wave conditions can be seen as stabilized. The exponential fitting curves is used to describe the trends in the measured data.

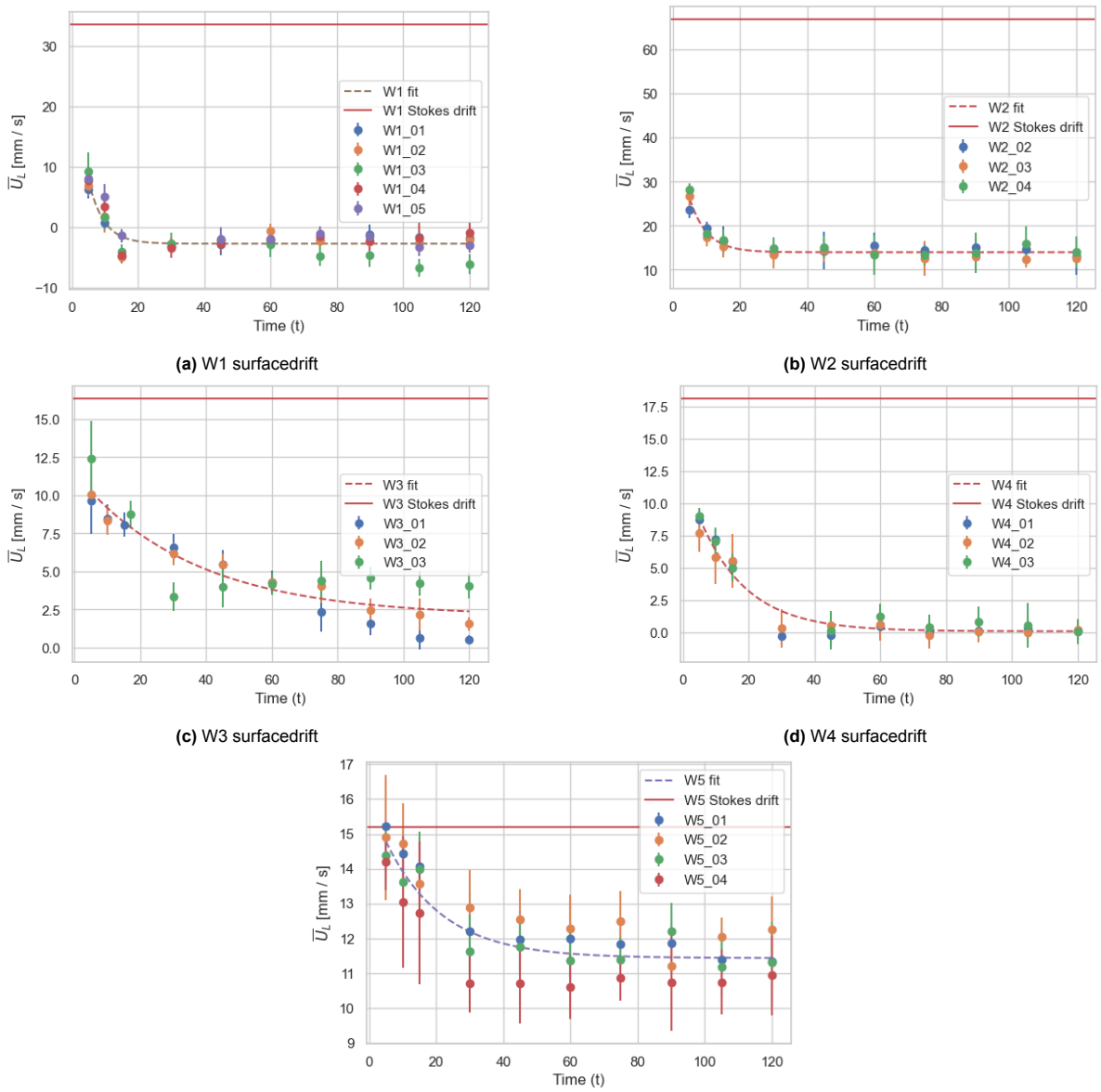

(a) W1 surfacedrift

(b) W2 surfacedrift

(c) W3 surfacedrift

(d) W4 surfacedrift

(e) W5 surfacedrift

Figure 4.6: Surface mean x-direction Lagrangian drift velocity outcomes with the theoretical Stokes drift velocity and exponential fit. - - : the exponential fitting curves. ● with vertical standard deviation range: the observed surface drift velocity, and the standard deviation is the result from each single measurement. —: the calculated theoretical Stokes drift velocity at the surface from equation 2.10

4.2.3. Comparison between theoretical and measured Eulerian velocity

After obtaining the stable value of the Lagrangian drift velocity, the Eulerian current at the surface can be calculated using Equation 2.11. Figure 4.7 displays a comparison between the observed and theoretical Eulerian velocities at time period t5 (Figure 4.7a) and at equilibrium (Figure 4.7b). As shown in the figure, the measured values are close to the theoretical values at t5, while W1 and W2 exhibit a larger magnitude of the velocities compared to the depth-uniform current. At equilibrium, the observed velocities become even more larger magnitude of the velocities than at $t5$. Except for W5, the deviations from the theoretical values increase for other wave conditions compared to t5. Furthermore, waves with higher Eulerian velocities show larger deviations from the theoretical values.

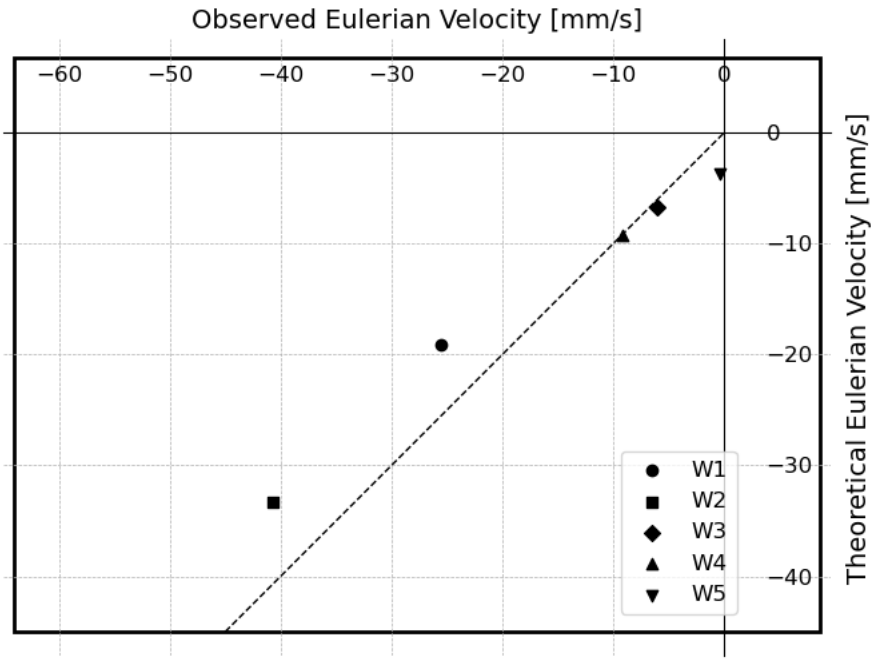

(a) t5

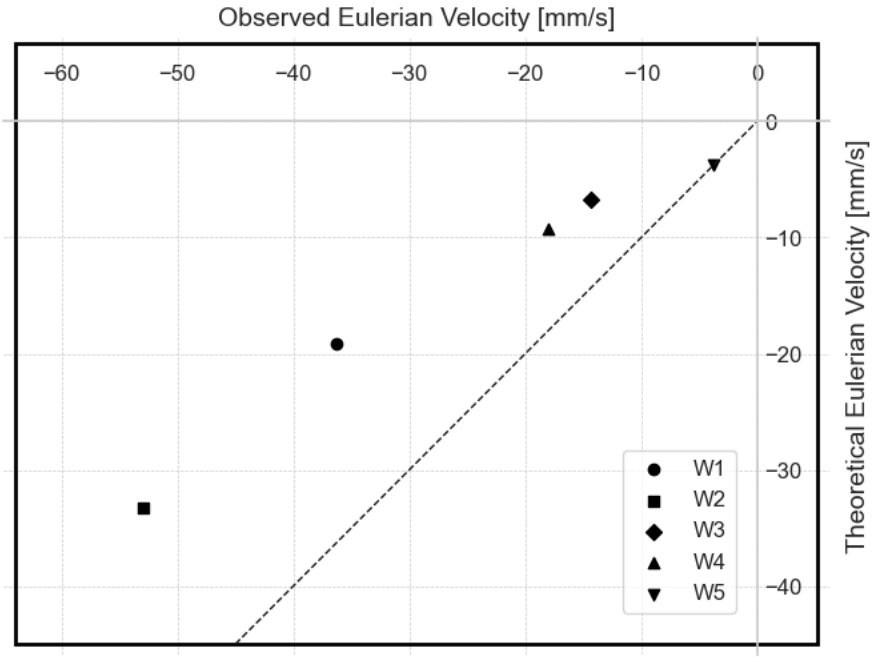

(b) Equilibrium

Figure 4.7: Comparison between Observed $\overline{U_E}$ and depth uniform value at t5 and equilibrium. The x-axis represents observed velocities and the y-axis represents theoretical velocities, both in mm/s. The dashed line represents the value when the observed value equals the theoretical value.

Equation 2.9 and 2.15 are both a function of kh and ka. In order to evaluate the influence of kh and ka separately, the equations first need to be arranged. From equation 2.9, we can alter the expression for the surface Stokes (z=0) as:

$$U^*_{std} = \frac{\sigma \tanh 2kh}{g} U_{std} = (ka)^2 \tag{4.1}$$

Then we alter the same way the conduction solution (equation 2.15), when on the water surface (z=h),

we can altered the expression as:

$$\overline{U_L^*} = \frac{\sigma \tanh 2kh}{g} \overline{U_L}(z = h) = F(kh)(ka)^2 \tag{4.2}$$

With the $F(kh)$:

$$F(kh) = \frac{2\cosh(2kh) - \frac{3}{2} + \left(kh - \frac{3}{2kh}\right)\sinh(2kh)}{2\cosh(2kh)} \tag{4.3}$$

The normalized Stokes drift U_{std}^* is only related to ka, while the normalized version of the conduction solution at the surface $\overline{U_L^*}$ is a function of both ka and kh. Therefore, the slope of $U_{std}^*/(ka)^2$ is 1 but the slope of $\overline{U_L^*}$ is $F(kh)$. Figure 4.8 shows the normalized version of $\overline{U_L^*}$ versus $(ka)^2$. The components of the Figure 4.8 can be read as follows: The gray dashed line is the normalized Lagrangian drift when the Eulerian return current is zero, hence results in the normalized Stokes drift. The Blue dashed line is the conduction solution given the different wave conditions while the blue region represents the range of the conduction solution. The light blue dots represents the Stokes drift plus the uniform Eulerian current, hence result in the irrotational solution. and the dark blue dots represents the equilibrium measured Lagrangian drift. For the conduction solution, it can be noticed from the figure that the slope corresponding to $\overline{U_L^*}$ (blue dashed line) increases with kh. The range of variation is larger than that of irrotational theory. Additionally, the conduction solution predicts a larger value than the Stokes drift (gray dashed line) at sufficiently high kh, indicating that the surface Eulerian flow derived from Equation 2.18 would be positive.

In the measured data, the size of kh also affects the agreement with the irrotational solution or the conduction solution. For W4, W3, and W1,W5, which have similar ka, the kh ranges from 0.709 to 2.00. We can see that for W1 (kh = 0.709), it is more consistent with the prediction of the conduction solution. However, for W5 (kh = 2.00) the observation coincides with the irrotation solution accounting for depth-uniform Eulerian return current. For W3 (kh = 1.175) the observed values are generally smaller than for the irrotational solution as well as the conduction solution.

For W2 and W4, which have the same kh (0.959) but different ka, the observations under this kh condition are not consistent with the irrotational solution as well as the conduction solution, and the offset values increase with increasing ka.

In the case of small ka and kh ranging from 0.7 to 1.175 (W1, W3, W4), the observed Lagrangian surface drift is close to zero and sometimes negative.

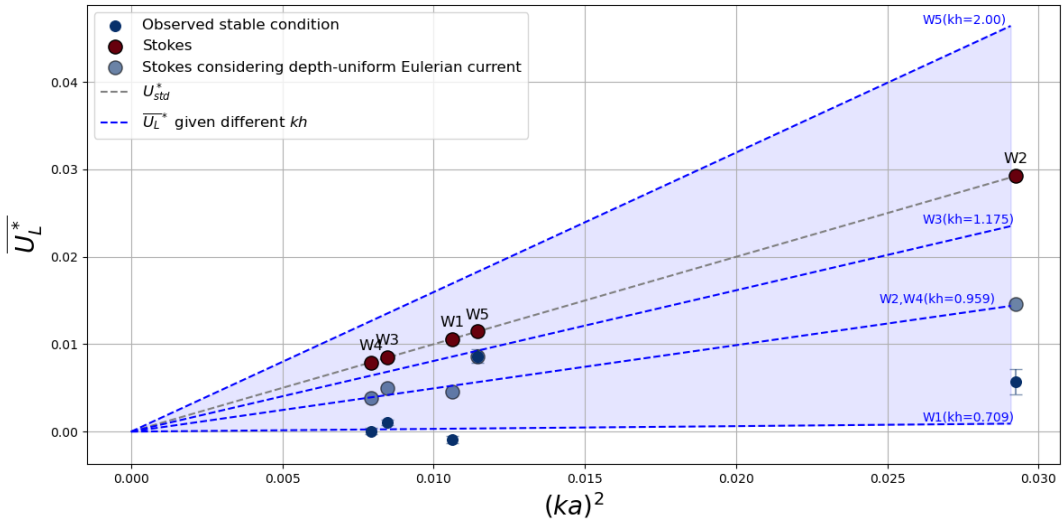

Figure 4.8: Comparison between the normalized Stokes drift, conduction solution and the observed drift at the surface. The blue dashed line: normalized conduction solution with different kh. The blue filled area: The range of the solution that the 5 types of wave considered

4.3. PTV measurements

In the following PTV measurements, data from W1_01, W2_01, W3_02, and W4_01 are used, as these experiments had the most tracked particles or the widest particle distribution among all the replicated experiment IDs.

4.3.1. Uncertainty of the particle velocity

Figure 4.9 illustrates the uncertainty of the velocity in the x, y, and z spatial directions, and the computational procedure is given in section 3.6.5. We binned the space, dividing it into 15 bins, and then calculated the uncertainty within each bin along with its standard deviation. As can be seen from the figure, the overall error in V_z is large, while V_x, and V_y have similar error levels. In the x-direction (Fig. 4.9a), notice that the uncertainty of V_x rises significantly by about a factor of 2 when it is close to the edges, which may be due to factors such as camera lens distortion. However, as stated in Section 3.6.1, we selected particles to ensure a lower level of uncertainty by only keeps the particle information on the -150 mm to 150 mm interval in the x direction.

4.3.2. Uncertainty of the drift velocity

Figure 4.9 shows the uncertainty in the computed velocity, which is attributed to inaccuracies in the spatial positioning of the particles. As illustrated in Figure 4.9a, the uncertainty in the particle x-direction velocity u_x averages 2.5 mm/s, i.e., presents a ±1.25 mm/s error range. However, this does not imply that the error in our measured drift velocity is in the order of millimeters per second. This is because the drift velocity obtained is averaged over a Lagrangian period of approximately 1 second, in this case, the sampling frequency becomes $1Hz$ instead of $100Hz$. According to equation 3.34, the magnitude of the uncertainty in the drift is approximately 100 times lower than the particle velocity. Hence the uncertainty of drift velocity is $\frac{1.25\ \text{mm/s}}{100} = 1.25 \times 10^{-2}$ mm/s

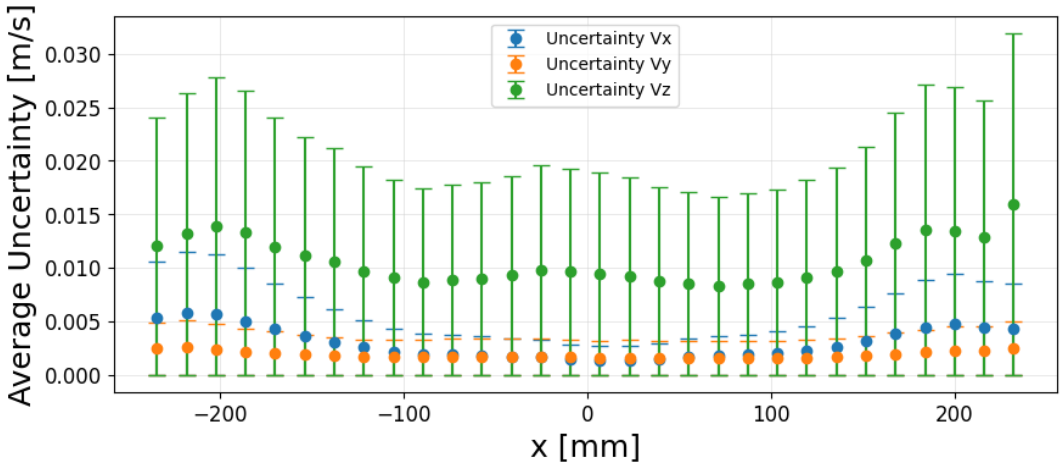

(a) Uncertainty vs. x

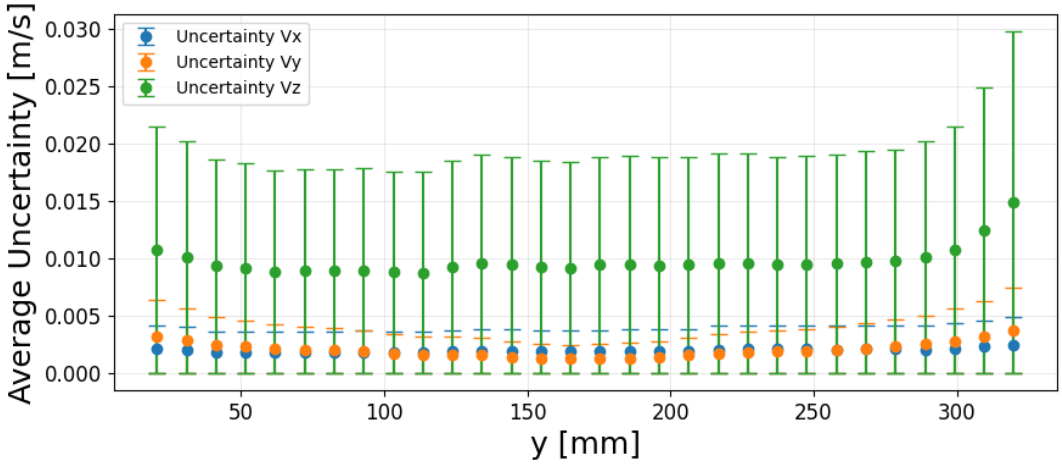

(b) Uncertainty vs. y

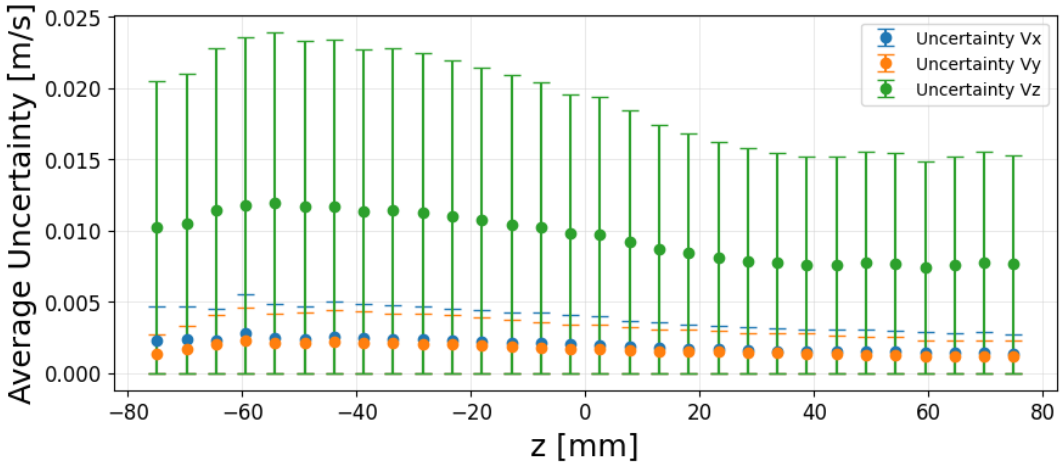

(c) Uncertainty vs. z

Figure 4.9: Average Uncertainty distribution from 3D direction. x, y and z is the wave propagation, vertical and cross wave flume direction respectively. Vx, Vy and Vz stands for the velocity in x, y and z direction.

4.3.3. Background motion

Figure 4.10 shows the background motion for each wave condition, with measurements taken over 20 seconds. According to the figure, the motion can be divided into two main distinct parts. The first part

is the vorticity observed in the central region of the water column, which is characterized by a relatively low velocity. In addition, there is a distinct upward collective motion characterized by relatively high velocities. This vertical motion may have originated from the previously discussed drift pattern, or it may have been an upwelling caused by the larger scale vorticity. Nonetheless, the relatively short duration of the initial motion tracking precludes definitive conclusions about the cause of the upward motion. Figure 4.11 shows the spatial distribution of the absolute values of the velocities of these particles, along with their uncertainty (shown by the error bars). Taken together, although there is some variation in their spatial distributions under a single experiment, the background velocities are not spatially significantly correlated when instrumental measurement errors are taken into account. It is worth noting that the peak drift velocity is an order of magnitude larger than the background motion (see Table 4.3).

As shown in Fig. 4.11, there are significant systematic errors along the x-axis in the ranges of -250 mm to -150 mm and 150 mm to 200 mm, with a maximum error value of 2.5 mm/s (W4) and an error bar significantly higher than that of particles in the interval of -150 mm to 150 mm. The standard deviation (error bar) in these outer regions is considerably larger than in the central interval (-150 mm to 150 mm), where the maximum particle error does not exceed 1.5 mm/s. As mentioned in Section 3.6.1, this error increases with distance from the center of the camera's field of view. This is mitigated by cropping the window, as described in Section 3.6.1. Table 4.11 shows that the range discussed in Section 3.6.1 exhibits lower uncertainty than the outer regions.

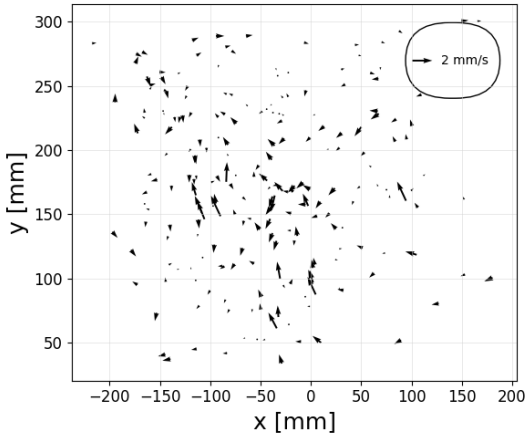

(a) W1

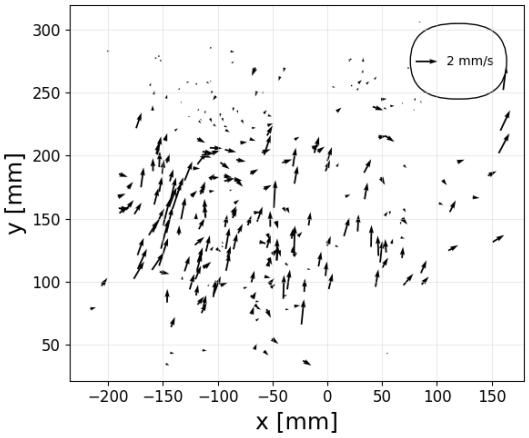

(b) W2

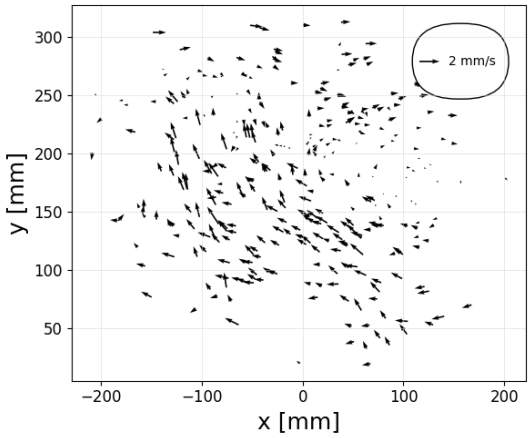

(c) W3

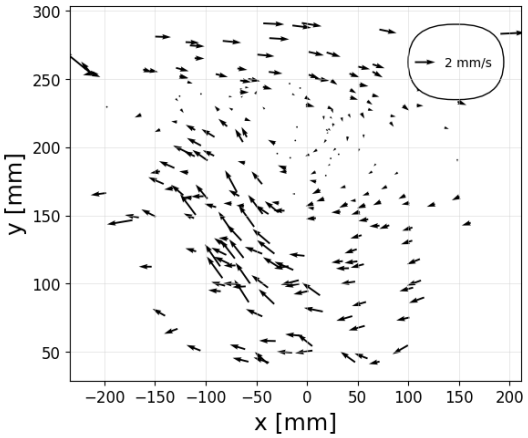

(d) W4

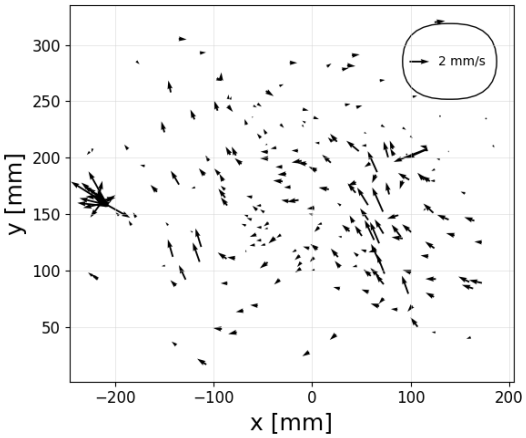

(e) W5

Figure 4.10: Pre-wave motion of particles in different wave conditions

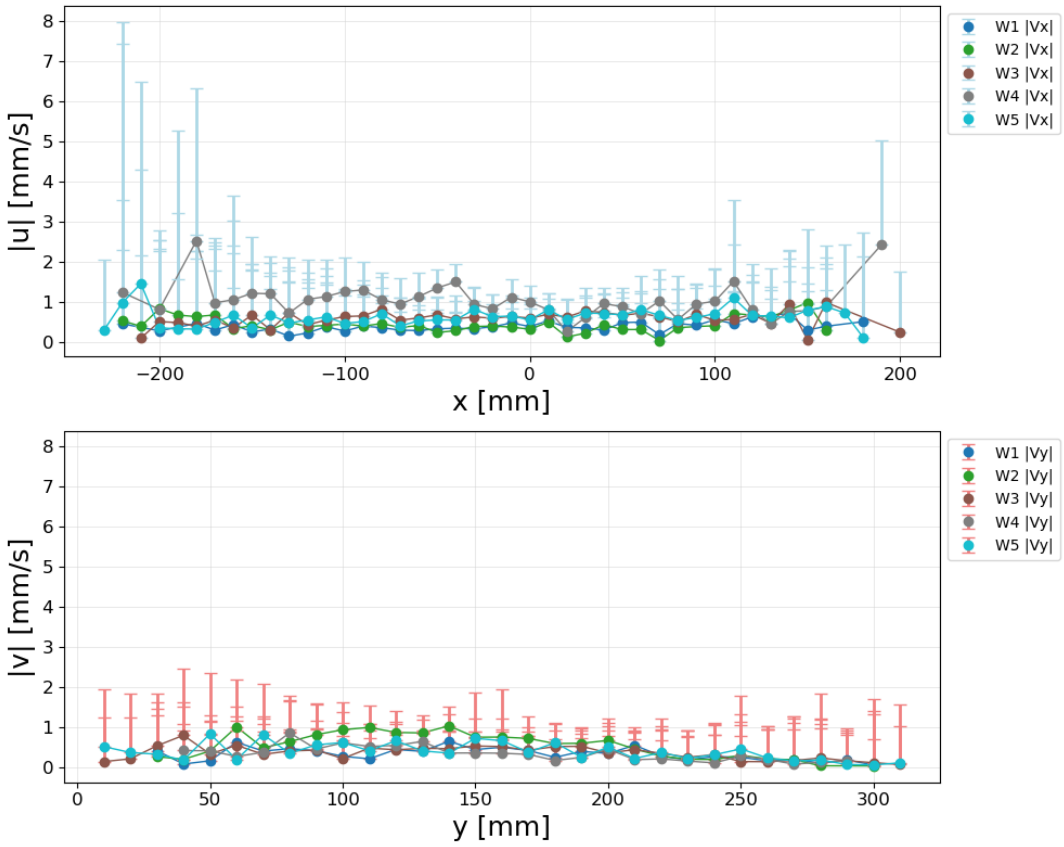

Figure 4.11: The velocity distribution of the background velocity. $|u|$: the x-direction magnitude of velocity; $|v|$: the y-direction magnitude of velocity.

Table 4.3: Average initial velocity in x, y and z directions for different waves

Wave	$V_x(mm/s)$	$V_y(mm/s)$	$V_z(mm/s)$
W1_01	-0.21	0.01	-0.15
W2_01	0.35	0.41	-0.01
W3_02	-0.26	0.29	0.06
W4_02	-0.45	0.11	-0.02
W5_01	-0.45	0.26	0.12

4.3.4. Comparison between different averaging methods

Figure 4.12 shows the mean Lagrangian drift profiles, analyzed using three methods in section 3.6.3: Wave Averaged using a wave-by-wave approach (blue solid line); Time-Averaging (green dashed line); and Low Pass (red dashed line). The x-axis represents the Lagrangian drift of $\overline{U_L}$ in mm/s, while the y-axis represents depth (y) in mm.

Figure (4.13) shows the standard deviation curves for each wave condition in more detail. It is clear that the time averaging method shows higher standard deviations, especially in the middle and deeper layers of wave types W3, W4 and W5. In contrast, the wave-by-wave method and the low-pass filter typically have the smallest standard deviations, indicating better stability and reliability. However, in the middle and deep layers, the standard deviation of the wave-by-wave method is smaller than that of the low-pass filter method. The wave-by-wave method has the highest resolution in the y-axis and acquires the largest amount of data, which results in a smaller error for the wave-by-wave method. The wave-by-wave method is well suited for tracking a small number of particles and a narrow confidence interval can be obtained. This method is found to be stable and reliable.

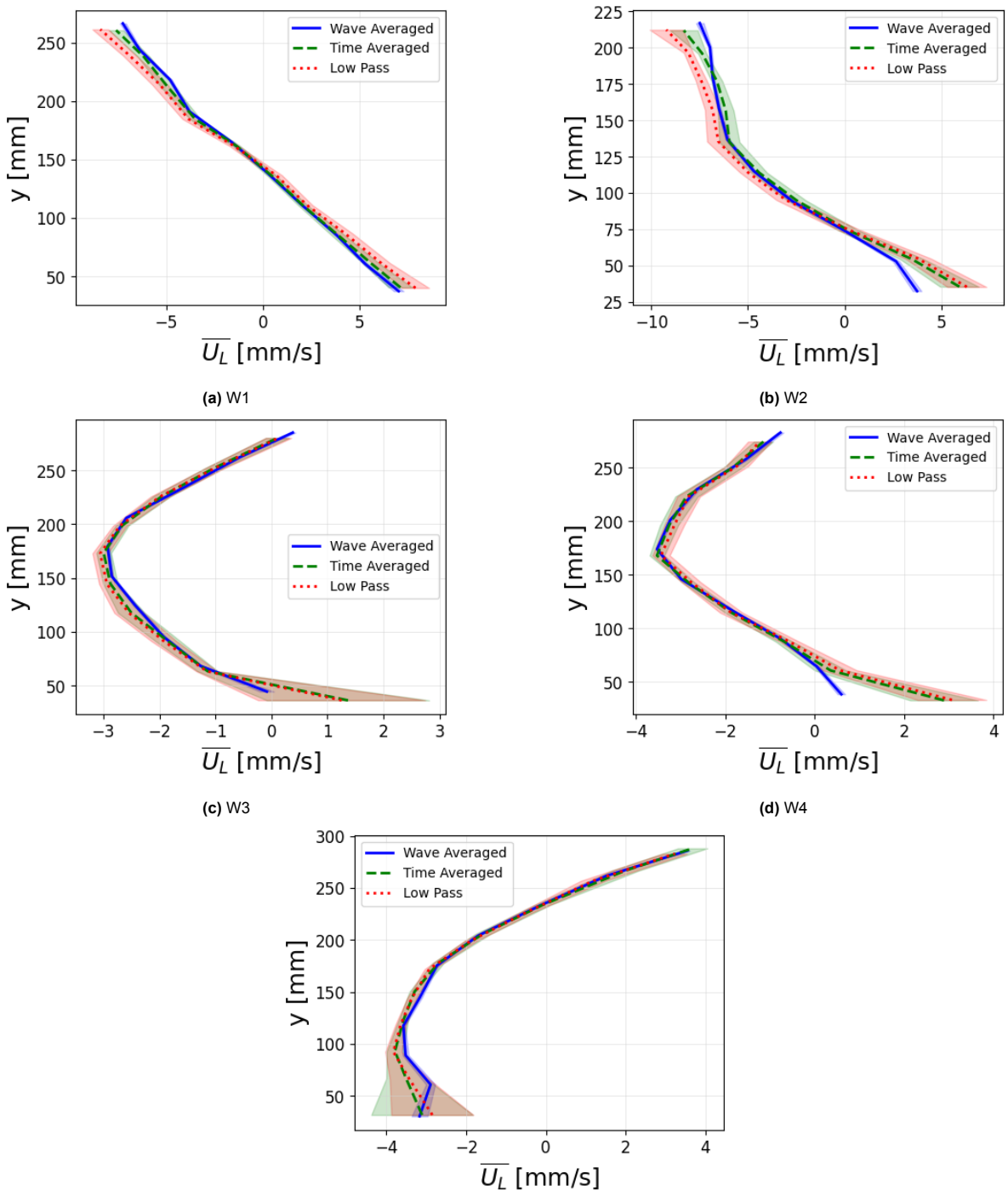

(a) W1

(b) W2

(c) W3

(d) W4

(e) W5

Figure 4.12: Lagrangian velocity as a function of the water depth based on the PTV-measurements for different averaging methods. Each sub-figure corresponds to a different wave condition. The shaded area represents the 95% confidence interval

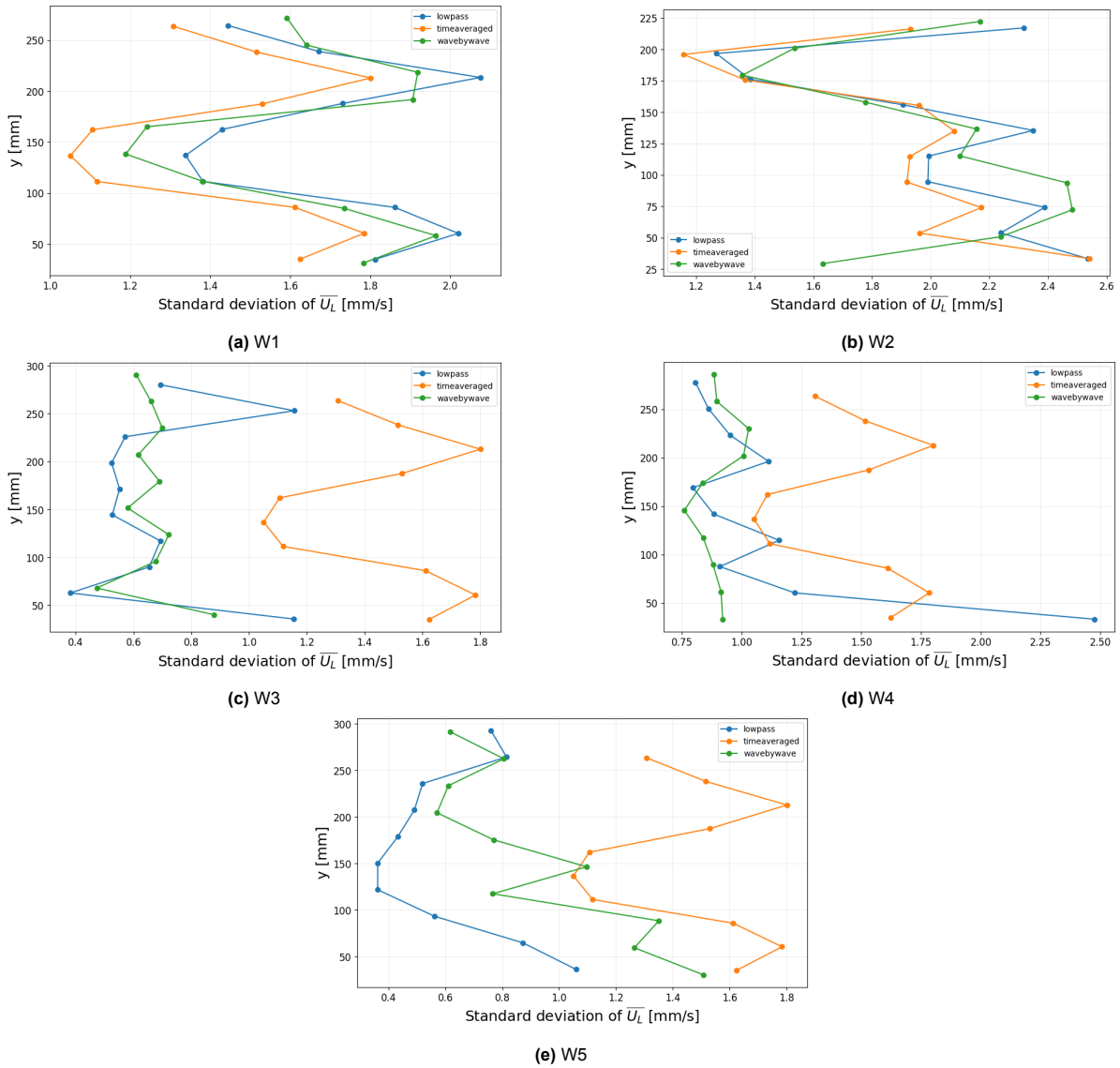

(a) W1

(b) W2

(c) W3

(d) W4

(e) W5

Figure 4.13: Standard deviation of the Lagrangian velocity over water depth based on the PTV-measurements for different averaging methods.

4.3.5. Correlation of the drift velocity with the cross flume direction

In order to examine the characteristics of the cross-wave flow component (z), The Pearson correlation coefficient is calculated. We take the W1_t05 as an example. The Pearson correlation r ranges from -1 to 1, where $r = 1$ indicates a perfect positive linear correlation, $r = -1$ indicates a perfect negative linear correlation, and $r = 0$ indicates no linear correlation.

Figure 4.14 shows that over the whole cross-flume direction (z direction), there is not much variation in the drift speed. At the same time, the value of the calculated correlation coefficient is -0.06. This indicates that the flow can be considered to be 2D in the analyzed particles and that the 3D effect due to the boundary is negligible.

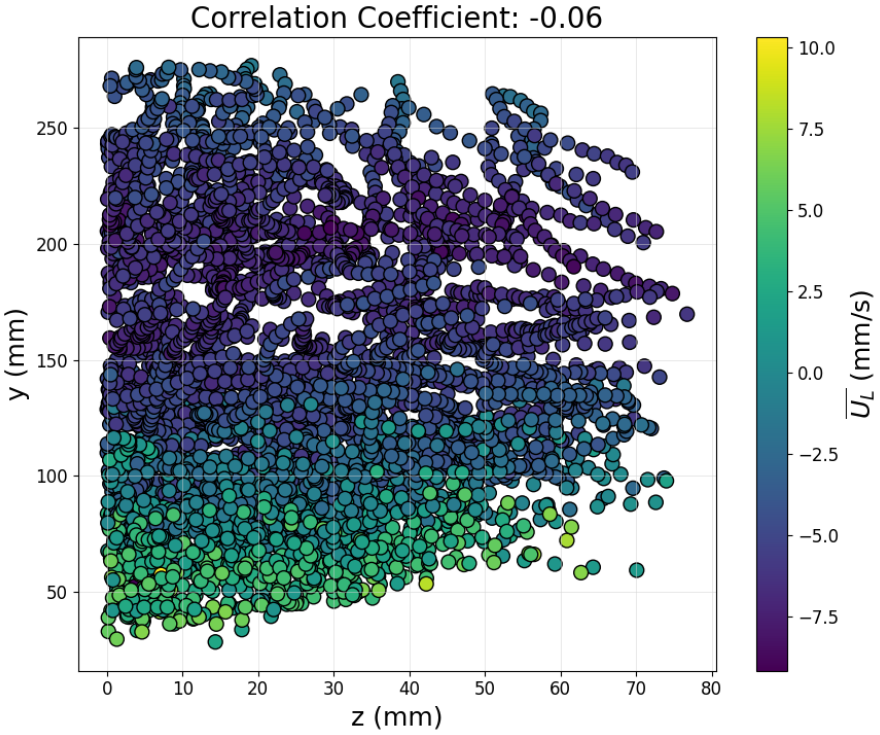

Figure 4.14: Correlation with the drift velocity and the z (cross-flume direction) at *W1_t05*. The scatter is mapped with the x direction drift velocity. The x-label: lateral position from the center of the wave flume, only positive value is taken into account. The y-label: vertical position with direction from bottom to surface. Upper text: the calculated correlation coefficient.

4.3.6. Comparison between observed and theoretical Lagrangian drift velocity

Using the wave-by-wave method, the theoretical Lagrangian drift can be obtained as shown in Figure 4.15 to Figure 4.19 for time interval t = 5 min, 10 min, 15 min, 30 min, 60 min, and 120 min. The plots also show the theoretical Longuet-Higgins solution and Stokes drift accounting for a depth-uniform Eulerian return current. The blue dots represent the wave-by-wave drift of each particle derived from the PTV measurements. The red line is the line connecting the mean values within each bin after dividing the depth into 15 bins, with a 95% confidence interval based on the variation of the velocities obtained for each tracked tracer. Surface drift results from the Z-Camera analysis have also been added at y = 350 mm (the still water level).

Subsequently, we examine the discrepancies in the measured data points. As illustrated in Figure 4.15 to Figure 4.19, notable variations in the measured drift exist at each depth; some wave conditions (i.e., W2, W3, W4) exhibit a 20 mm/s deviation at the a certain depth. Nonetheless, this does not necessarily indicate substantial measurement error. This uncertainties is generalized by wave-by-wave method, which will resolute the turbulence into the drift velocity. The most important indicator will be the averaged trend line and the confidence interval. Conversely, when these measurements are averaged using the binning technique, the resulting confidence intervals are sufficiently narrow. This precision is predominantly due to two factors: 1. the ample size of the sample data, and 2. the clustering of most sample particles around the average trendline.

In studying the evolution of the Lagrangian drift velocity with time under different wave conditions, we compare two theoretical solutions: the irrotational theory (Stokes solution) and the Longuet-Higgins-based conduction solution. The analysis shows that different wave conditions have different effects on the drift velocity, as shown in Figure 4.15 to Figure 4.19. For wave conditions W1-W4, the drift speeds for certain time periods are more consistent with the theory of the conduction solution. For example, at W1_t120, W3_t10 and W4_t10 and t15, the trend line supports the conductive solution. However, for wave condition W5 with larger kh values, the drift velocity tends to be more consistent with irrotational theory in the middle region of the water column (e.g., W5_t5, t10, t15). Also, near the water surface, the drift velocity of W5_t120 shows better agreement with the irrotational solution. While in the bottom

region, W5_t30 starts to deviate from the irrotational solution, showing differences from the theoretical solution.
According to Longuet-Higgins' theory, the irrotational solution (Stokes solution) applies when vorticity has not yet been conducted (i.e., under initial conditions). When vorticity is fully conducted and reaches a steady state, the conductive solution applies. Although the experiments in this study do not fully satisfy the assumptions of the conductive solution, the experimental trends qualitatively align with it. For example, the drift velocity in the mid-water column slows down and even shows a reverse flow, while positive flow occurs in the bottom region.

Top and Bottom Regions: In Figure 4.7, the surface drift velocity shows a transition from irrotational to non-irrotational solutions (except for W5). In the top part of the water column, the drift velocity decreases over time for W3, W4, and W5, while for W1 and W2, the drift velocity increases negatively. Near the bottom, the velocity generally increases over time, except for W5, where the trend differs. Eventually, the velocity in both the top and bottom regions stabilizes, though the stabilization time varies across different wave conditions.

Middle Part of the Water Column: The drift velocity in the mid-water column follows a distinct pattern. For wave conditions such as W1_t120, W3_t10, and W4_t15, the velocity profile in the middle of the water column matches the conductive solution (as shown by the red solid line in Figure 4.15 to Figure 4.19. However, for W3 and W4, the drift velocity gradually deviates from the conductive solution over time, with the negative velocity peak shifting toward the upper layer of the water column and eventually approaching the surface.
In contrast, for W5, the mid-water drift profile initially follows the irrotational solution during the first 15 minutes. However, by t=30, deviations start to appear near the bottom of the water column, and by t=60 and t=120, the entire mid-water column diverges from the irrotational solution.
Figure 4.20 shows the magnitude of vertical displacement rate $\overline{|W|}$. From Figure 4.20, it can be seen that the absolute value of the y-axis displacement velocity is larger near the water surface, and in the case of W2 (with the largest ka), the velocity at t30, t60, and t120 is significantly greater than that of the other wave conditions. Conversely, W5 (with the smallest kh) has a velocity significantly smaller than the others. However, for the x-direction drift velocity below the surface (Figure 4.15 to Figure 4.19), the absolute value of W2's drift velocity is smaller than that of W1, while W5 is similar to W3 and W4. Thus, we can conclude that there is no clear correlation between the absolute value of the y-axis displacement velocity and the magnitude of the x-direction drift velocity. From a vorticity perspective, if a stronger vorticity leads to a greater absolute y-axis displacement velocity, then the vorticity near the surface is larger than near the bottom. But to make this conclusion, we should analysis the impact of the initial motion first.
However, due to the relatively small magnitude of the y-axis displacement velocity (typically ranging from 0.5 to 1 mm/s), the background motion becomes significant in comparison. The background motion averages below 1 mm/s, with a maximum of 2 mm/s, as shown in Figure 4.11. It is important to note that the duration of the background motion measurement plays a crucial role in determining whether the background motion can be reliably compared with the y-axis displacement velocity observed during the "real" PTV measurements. But the measurement time of the background motion is too short (20 second), its influence on the overall uncertainty may be overestimated.

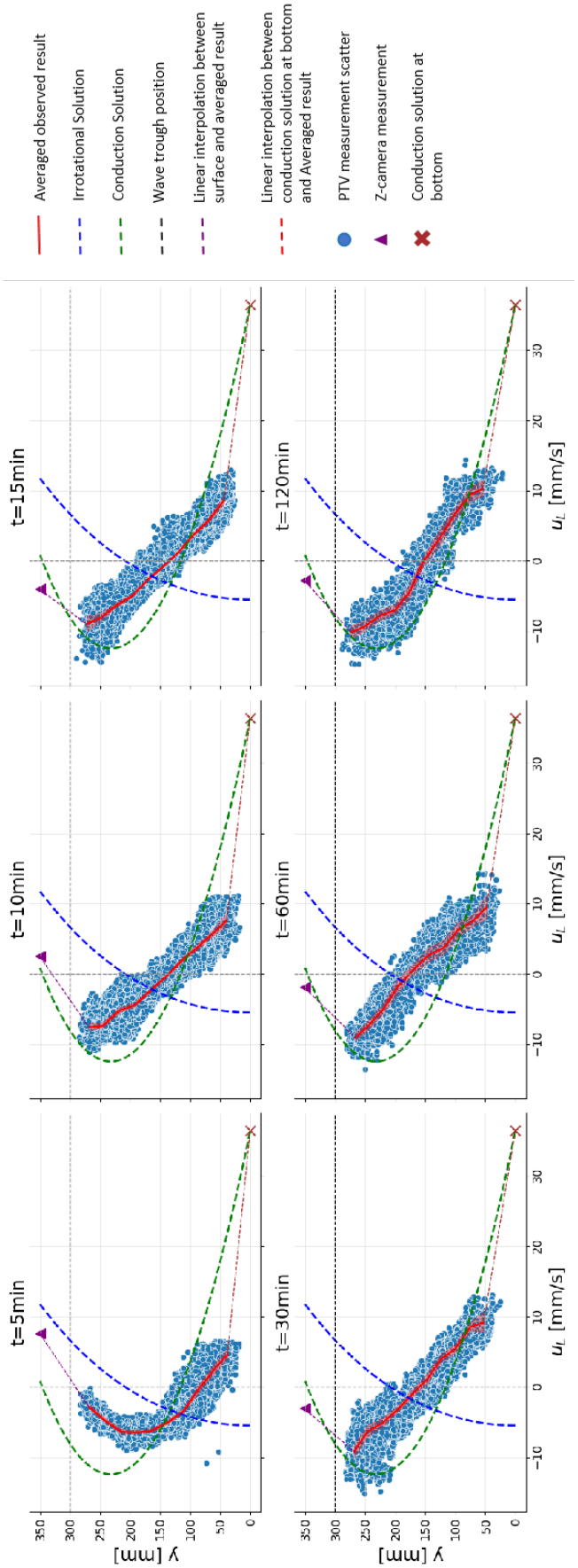

Figure 4.15: Observed Lagrangian Drift and theoretical drift velocity (W1)

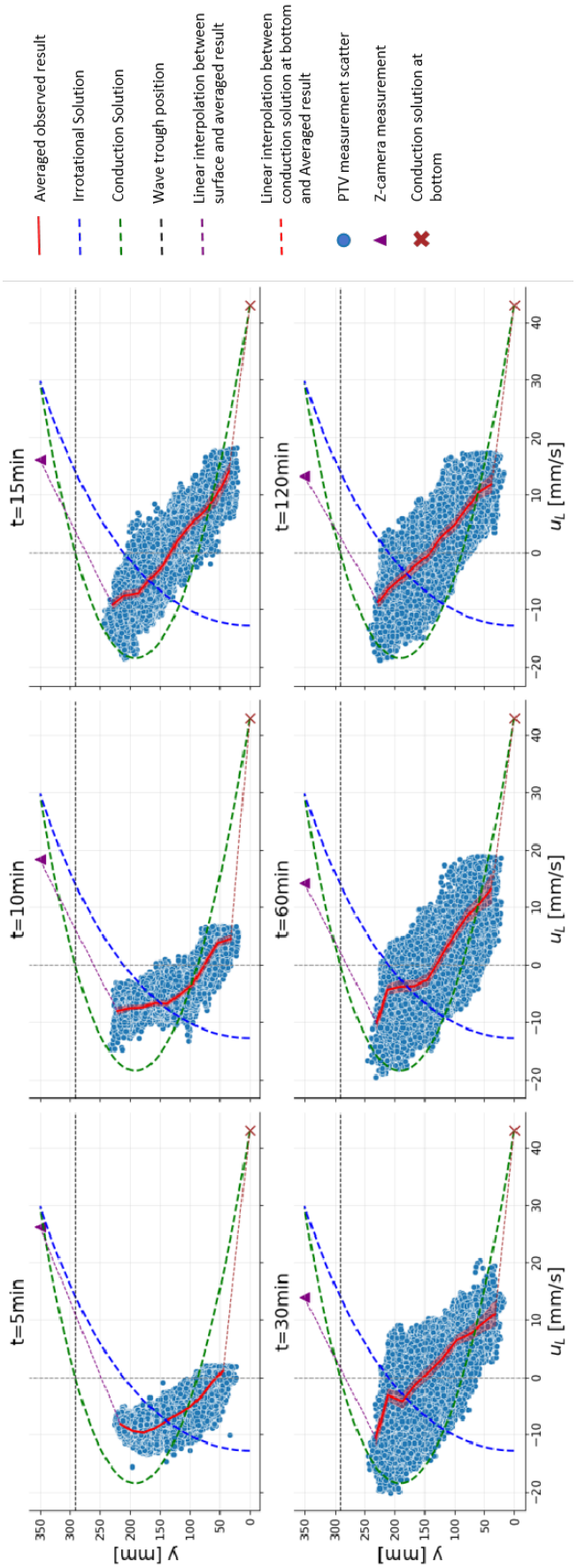

Figure 4.16: Observed Lagrangian Drift and theoretical drift velocity (W2)

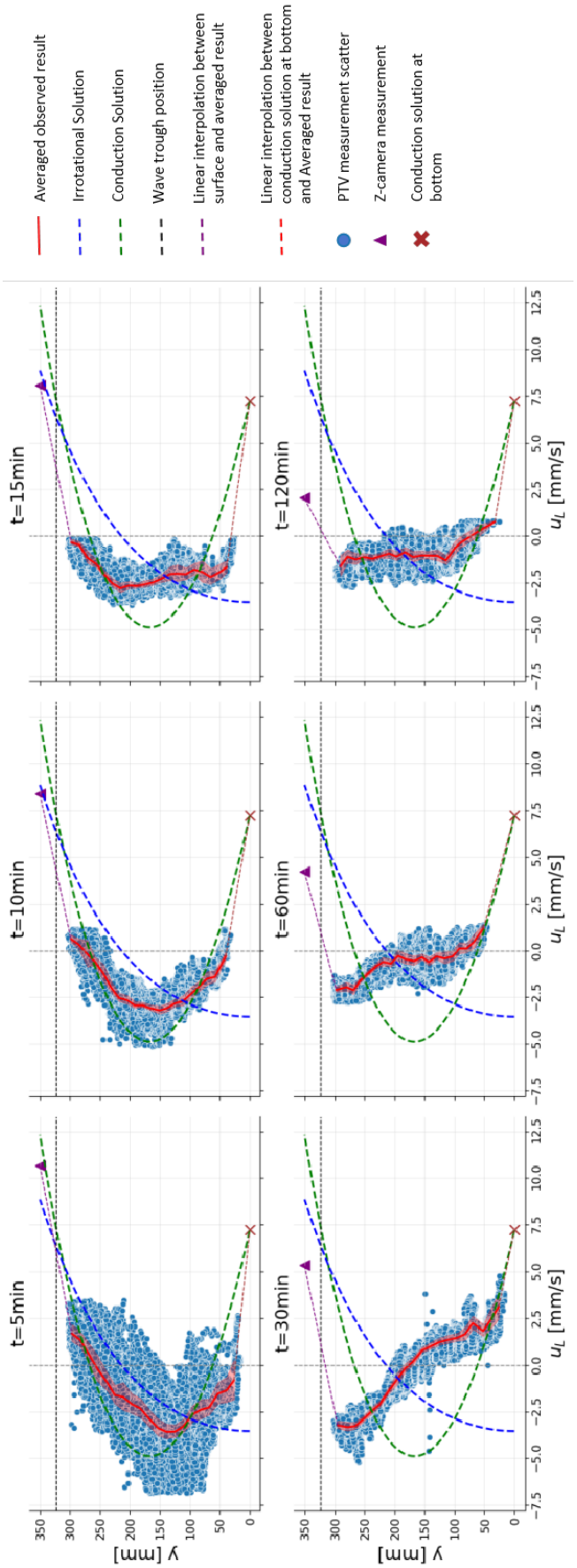

Figure 4.17: Observed Lagrangian Drift and theoretical drift velocity (W3)

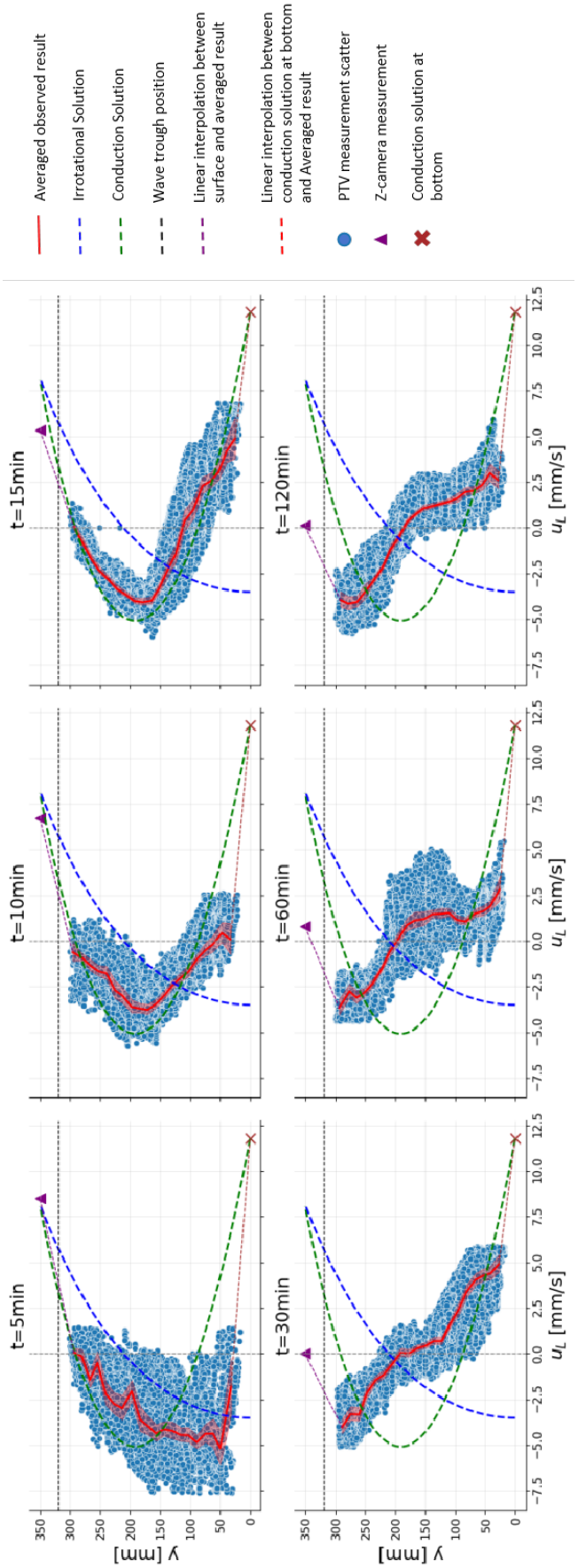

Figure 4.18: Observed Lagrangian Drift and theoretical drift velocity (W4)

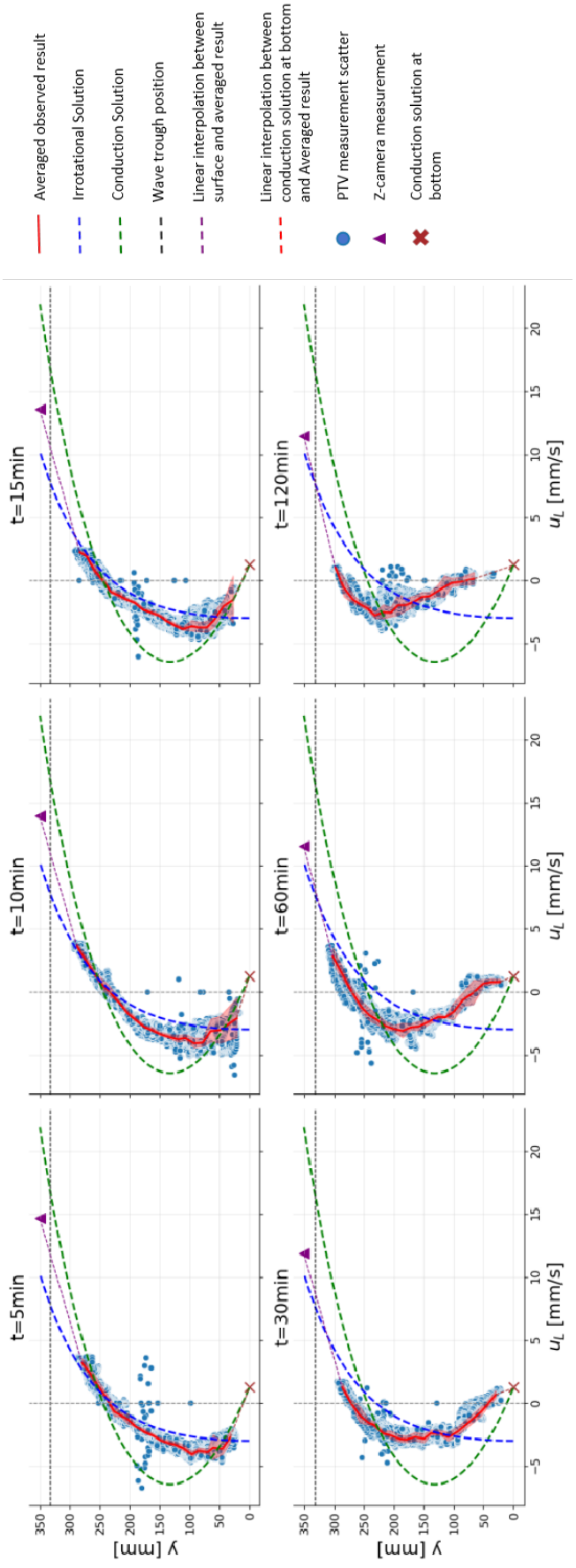

Figure 4.19: Observed Lagrangian Drift and theoretical drift velocity (W5)

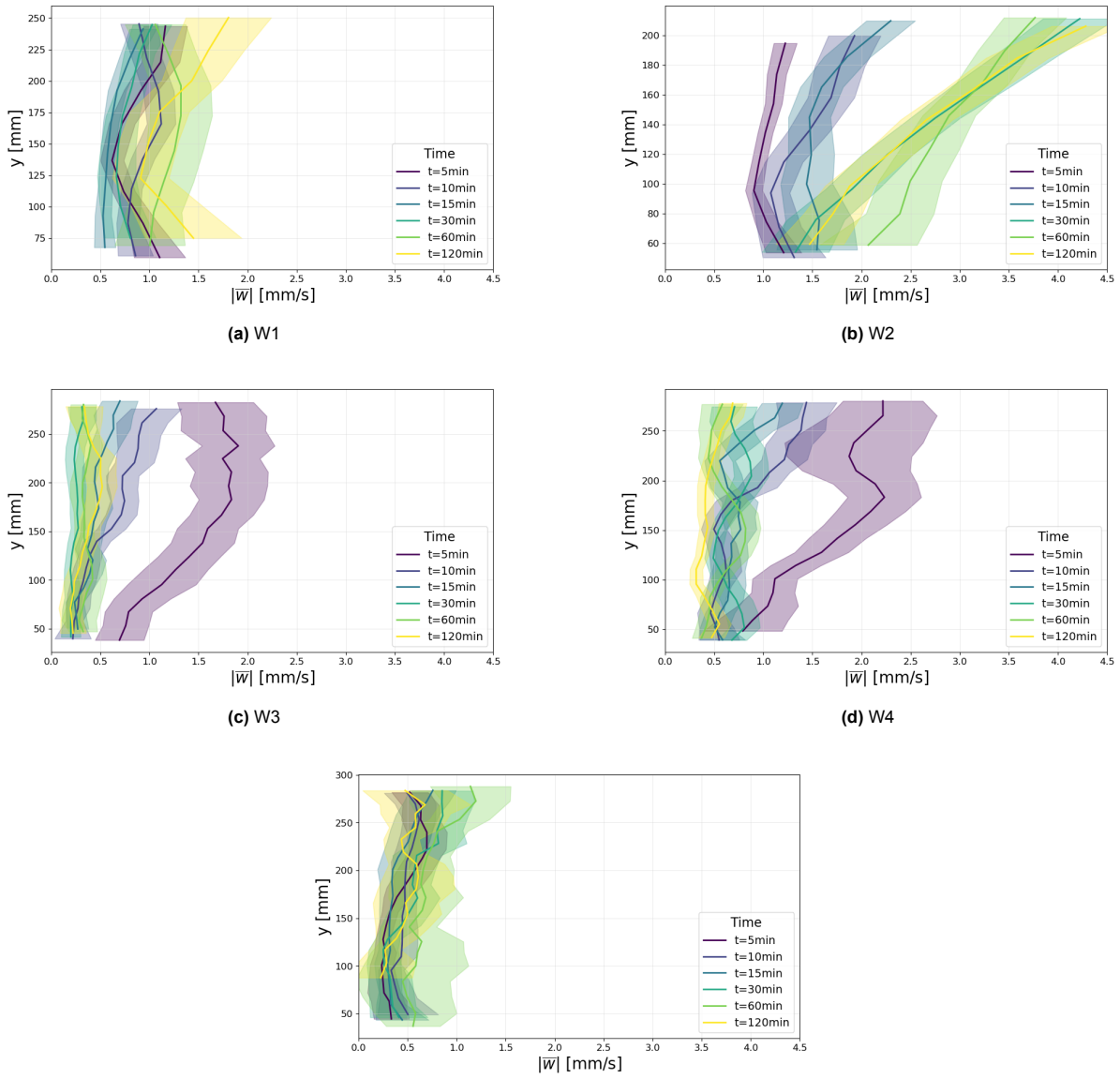

(a) W1

(b) W2

(c) W3

(d) W4

(e) W5

Figure 4.20: The magnitude of measured displacement rate in vertical direction $\overline{|W|}$, with the 95% confidence interval. The color indicates the time step.

Then the accuracy of the interpolation between surface, middle depth, and bottom is evaluated (Figure 4.15 to Figure 4.19 purple dashed line and orange dashed line). By Equation 2.12, the integration of the Lagrangian profile over depth should be zero. Table 4.4 shows the integral results of each wave condition after averaging all the time slots. In addition, the Average velocity deviation with respect to every time slot are shown in Figures(Figure 4.15 to Figure 4.19). The interpolation and PTV measurement averaged result (red solid line) is all taken into account. Then, if the integrated result is divided by the water depth (350 mm), the average velocity deviation is obtained, which indicates the averaged velocity profile deviation over the whole depth.

In comparison to the uncertainty of the PTV drift measurement (on the scale of 1.25×10^{-2} mm/s), the error here is significant for all wave conditions except W5. This difference can mainly be attributed to two factors: 1) the deviation caused by linear interpolation, 2) the discrepancy between the theoretical bottom velocity and the actual velocity. In all wave conditions, W1 and W2 exhibit the largest deviations, and W1 and W2 also have the highest wave heights, leading to the lowest trough positions. This suggests that there is a significant measurement gap between the PTV measurements and the surface measurements (approximately 75 mm for W1 and 125 mm for W2) (as can also be seen in **??**). In

contrast, W5, with the smallest discontinuity, also shows the smallest deviation. Therefore, it is it is expected that within the measurement gap between the PTV and surface drift velocities, there may be a more complex velocity profile.

Wave condition	**Integrated result** (mm^2/s)	**Average velocity deviation** (mm/s)
W1	255.72	0.73
W2	459.59	1.31
W3	-94.70	-0.27
W4	-66.18	-0.19
W5	3.92	0.01

Table 4.4: Integral result of Lagrangian profile over depth and the Average velocity deviation.

4.3.7. The velocity profile of Eulerian current

In this section, the measured Lagrangian drift velocities with the interpolation for the whole depth are used in combination with the Stokes drift, as represented by equation 2.18, to compute the Eulerian velocity profiles. The depth uniform Eulerian velocity is calculated using Eq. 2.17 and Stokes drift is calculated using Eq. 2.9.

In Figures 4.21 to Figure 4.25, we examine the Eulerian return flow velocity profiles under each wave conditions across various time intervals. The computed Eulerian velocities are depicted by the red solid line. For comparative purposes, the theoretically calculated Stokes drift velocities are shown by the blue line, and the measured and interpolated Lagrangian mean velocities are represented by the gray solid line. The red dashed line indicates the depth-uniform Eulerian flow (irrotational solution). The green dashed line indicates the Eulerian flow of the conduction solution.

For all wave condition, the shape and magnitude of the Eulerian return flow velocity profile undergo significant changes over time. Overall, in the region above a depth of y = 50 mm, the Eulerian flow evolves from a relatively uniform state at t = 5 minutes into a shear flow. Near the surface, the Eulerian flow exhibits notable negative enhancement, while in the region about 50 mm above the seabed, there is positive enhancement. The sheared pattern implies the evolution of the vorticity. This transition typically stabilizes after 30 to 60 minutes. For wave conditions W1 and W2, this stabilization occurs earlier. However, at equilibrium state, all the wave condition shows a deviation from neither the the irrotational solution nor conduction solution. It is worth noting that the magnitude of Eulerian flow velocity at the surface tends to become more larger in comparison to the conduction solution at the equilibrium state. However in the mid-water column, the magnitude of the Eulerian flow velocity is smaller at the prediction of the conduction solution.

4.3.8. The vorticity profile evolution in different wave condition

The vorticity profile for each wave condition is shown in Figure 4.26. Over time, the vorticity gradually deviates from the irrotational solution as the flow evolves. However, the profiles do not align with the theoretical predictions of the conduction solution. Above $y = 50$ mm, the vorticity is larger than predicted by the conduction solution in the upper half of the water column, while it is smaller in the lower half. Overall, except for wave condition W5, the vorticity increases more uniformly and positively across the entire water column at equilibrium. This contrasts with the conduction solution, which predicts a decrease in the upper part of the column and an increase in the lower part.

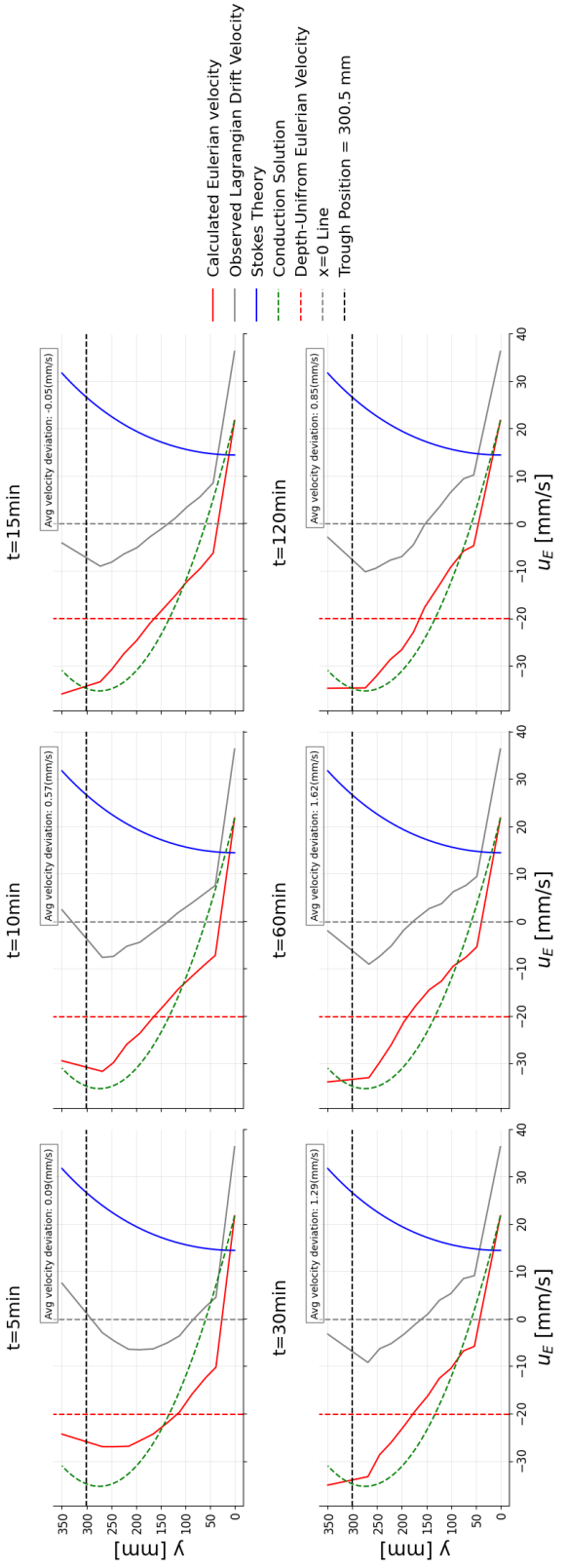

Figure 4.21: Eulerian velocity profiles for different waves (W1)

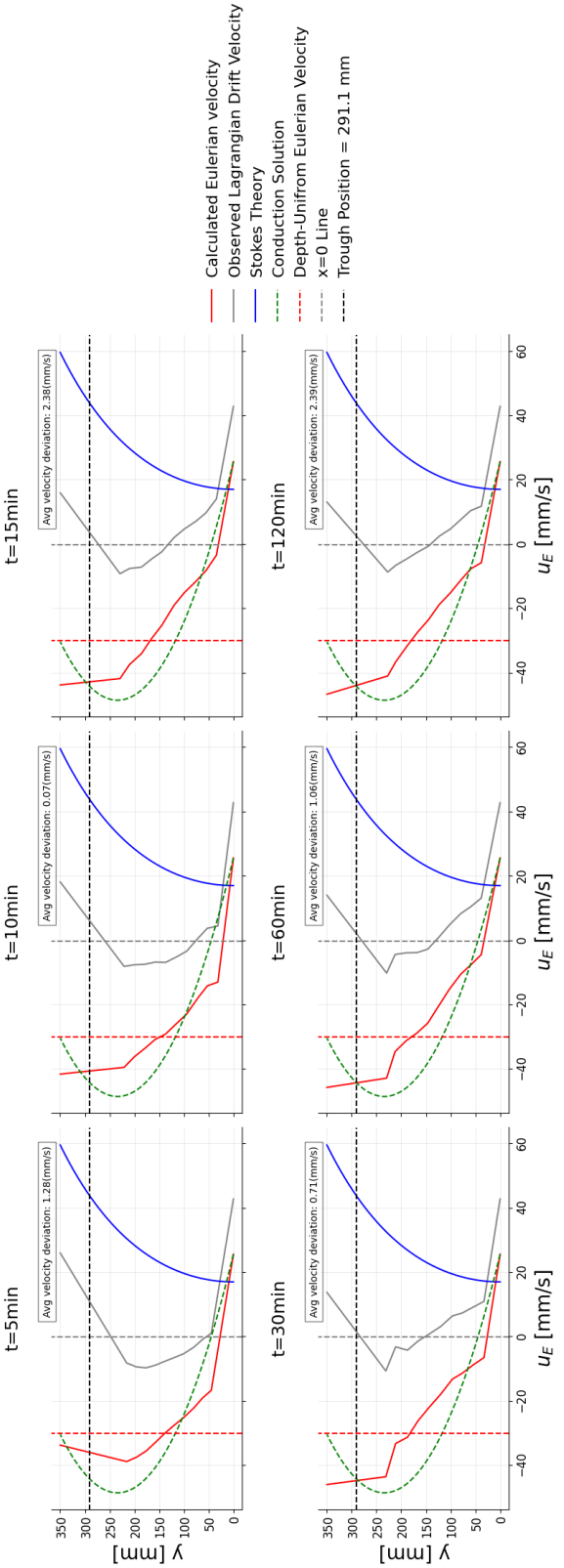

Figure 4.22: Eulerian velocity profiles for different waves (W2)

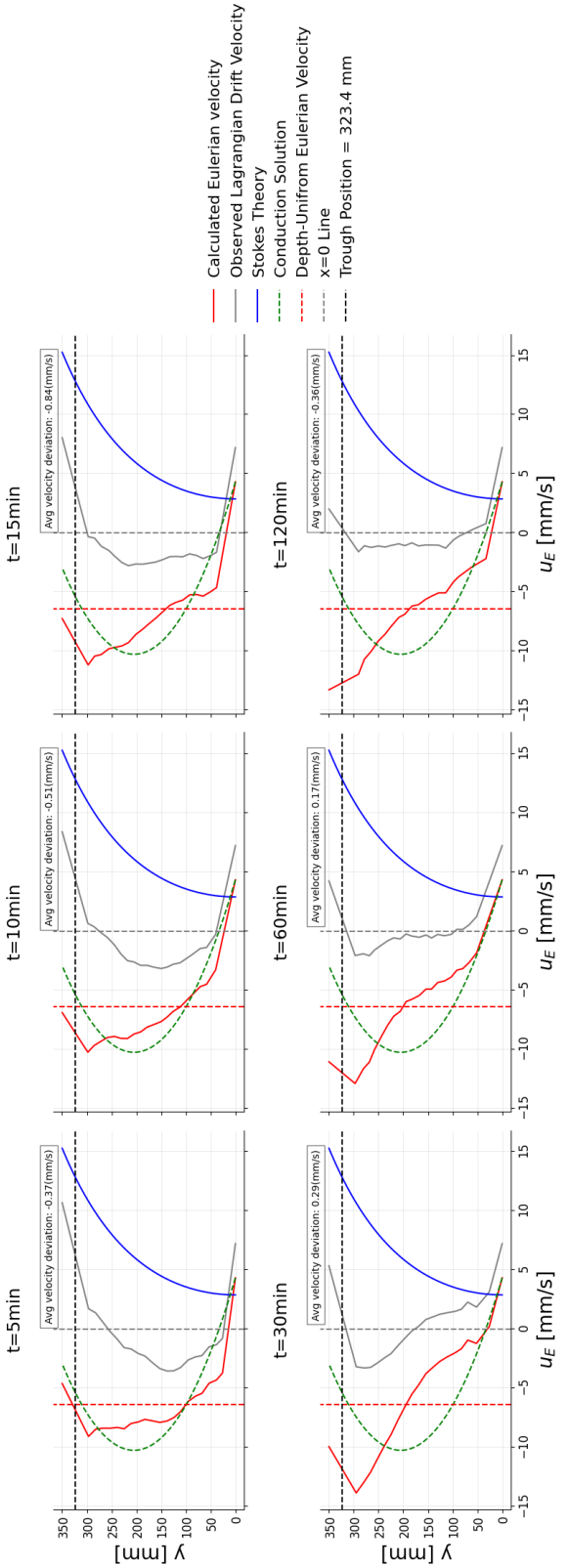

Figure 4.23: Eulerian velocity profiles for different waves (W3)

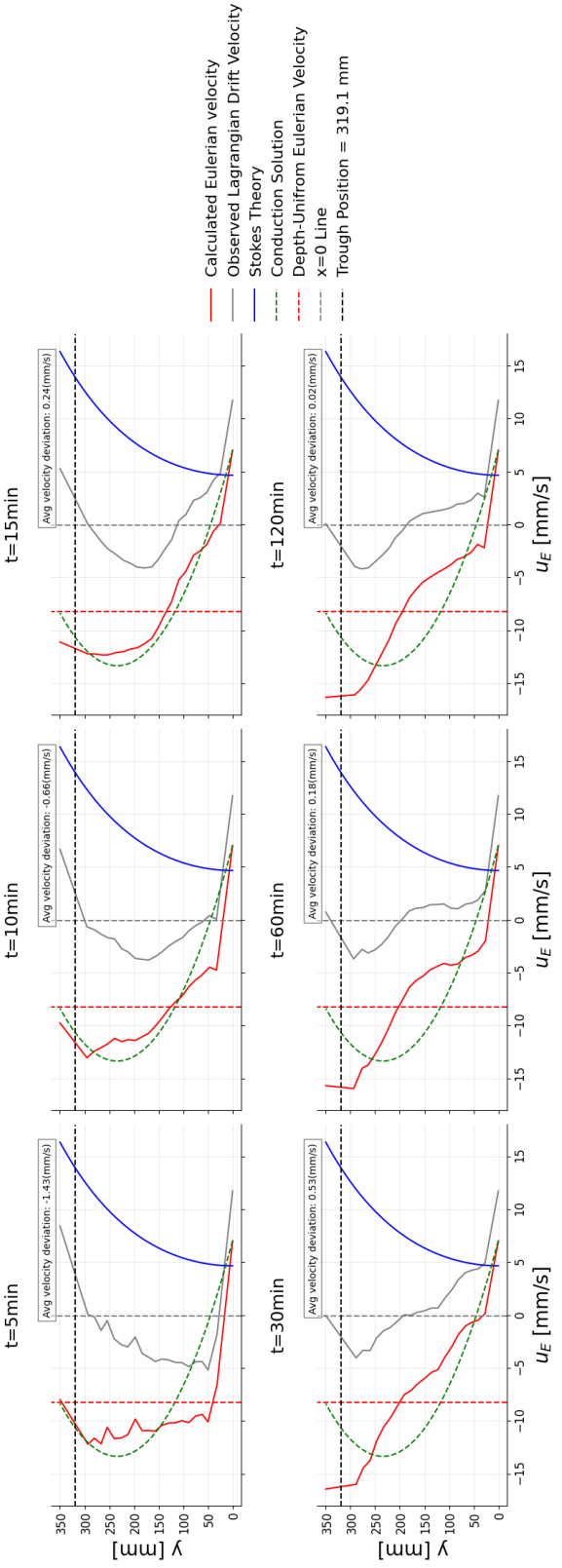

Figure 4.24: Eulerian velocity profiles for different waves (W4)

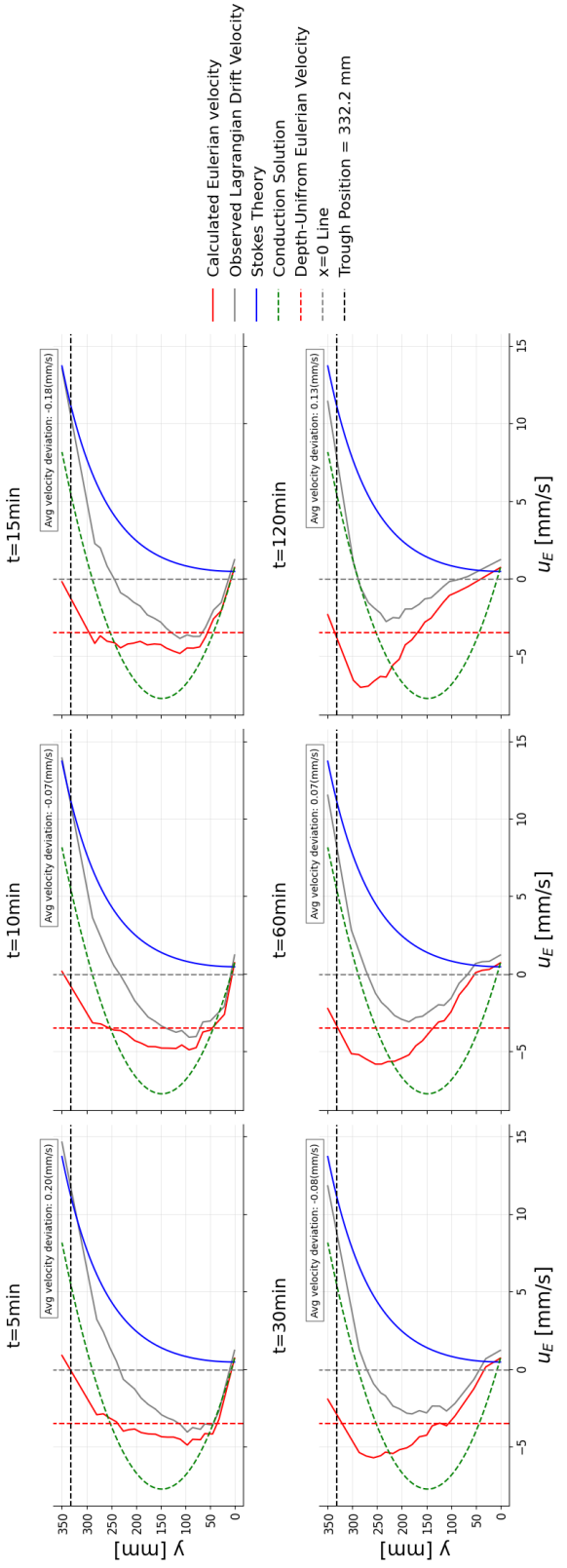

Figure 4.25: Eulerian velocity profiles for different waves (W5)

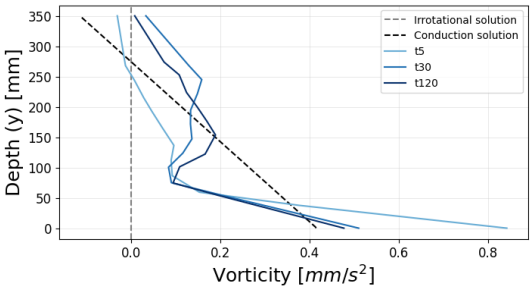

(a) W1

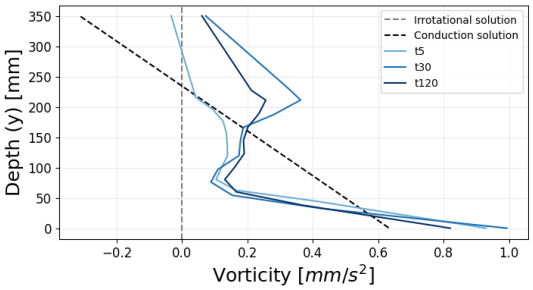

(b) W2

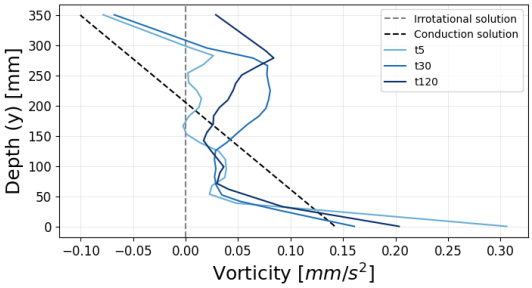

(c) W3

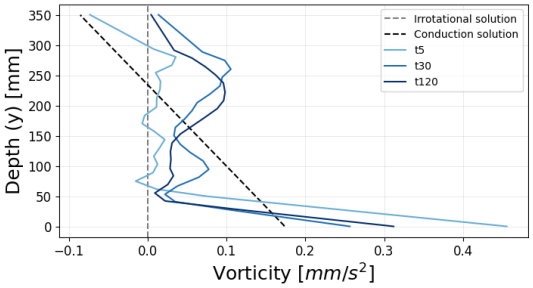

(d) W4

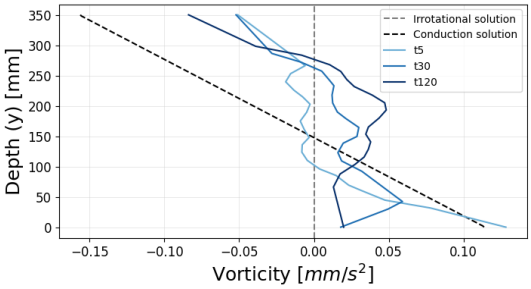

(e) W5

Figure 4.26: Vorticity profiles evolution in different wave conditions, in comparison with the irrotational solution and the conduction solution

5

Discussion

The Discussion chapter examines the experimental results in relation to wave-induced currents, comparing them with irrotational and conduction model and past research. It highlights the benefits of using advanced particle tracking methods, which offer higher resolution and accuracy in measuring velocity profiles. The chapter also addresses discrepancies between observed data and theoretical predictions, focusing on the effects of wave steepness, water depth, and vorticity. It further discusses how velocity profiles change over time and where the experimental data differs from conduction solution model. Lastly, it suggests future research directions to improve understanding of surface drift and vorticity dynamics.

5.1. Comparison of PTV System and Traditional Methods

In this study, we revisited the velocity profiles of wave-induced currents under different wave conditions. Using LaVision's MiniShaker 4DPTV, compared to the methods employed by **(author?)** [21] and **(author?)** [15], this system offers the following advantages:

5.1.1. Shorter Time Intervals Between Consecutive Measurement

The method of using dye to measure Lagrangian displacement has certain limitations, as it is not possible to obtain two consecutive Lagrangian velocity profiles at the same location within a short period of time. If the dye has not fully dispersed, it can obstruct subsequent measurements. In contrast, with the PTV system, we can continuously measure Lagrangian velocity profiles in a short time interval without the issue of dye interference, allowing for more frequent and reliable data collection. Thus, the PTV system enables more frequent observations within a short period of time, providing higher temporal resolution and capturing finer details of the velocity profiles. Previous studies, such as those by **(author?)** [21] and **(author?)** [15], focused more on long-term evolution over periods like 3 hours or 24 hours. In contrast, by leveraging the high temporal resolution of the PTV system, we examined the evolution of the velocity profiles within a 2-hour window, specifically studying the intermediate steady state mentioned by **(author?)** [15].

5.1.2. The rate of displacement of particle in the y-direction

Although **(author?)** [21] and **(author?)** [15] also obtained the displacement in the depth direction using neutrally buoyant particles, their method of directly recording observations led to certain limitations: 1) velocity measurements at different depths had to be conducted at different times, and 2) they were unable to achieve high resolution in the depth direction. As a result, they discarded experimental data where the displacement in the depth direction was too large. However, in this study, particles across the entire mid-water depth will be tracked simultaneously, and by using the wave-by-wave method, a fine resolution in the depth direction can be achieved. Therefore, we will be able to systematically analyze the displacement of particles in the depth direction.

5.1.3. Quantitative analysis of tracking uncertainty

We also performed a quantitative analysis of the errors resulting from particle tracking uncertainty. The analysis shows that particle tracking uncertainty in the x and y direction can be ignored, whereas the error of z-direction (cross wave flume) is more significant (Figure 4.9c). However, further analysis revealed that within the observed range of 12 cm in the middle, the particle's x-direction (wave propagation) is uniform (Figure 4.14) and independent of z. Additionally, using the wave-by-wave method, we obtained the scatter of all measurement data and analyzed the standard deviation (Figure 4.15 to Figure 4.19). Supported by a large volume of data, we found that the confidence interval is very narrow, indicating that the obtained velocity profiles exhibit negligible uncertainty. In contrast, the studies by **(author?)** [21] or **(author?)** [15] did not include any quantitative analysis of uncertainty.

5.2. The temporal evolution of the Lagrangian velocity profile

As mentioned earlier, **(author?)** [15] also considered the temporal evolution of the velocity profile and categorized it into three stages: the initial state, the intermediate equilibrium state, and the final equilibrium state. In this experiment, we focus on the evolution from the initial state to the intermediate equilibrium state over a time scale of $t = 5$ to 120 minutes. We found that, within 60 minutes, all experimental wave conditions, except for W5, had reached an equilibrium state. However, W5 still exhibited slight differences between $t = 60$ and $t = 120$ minutes, likely due to its higher relative water depth, which requires more time for vorticity diffusion.

In all wave conditions, the Eulerian flow evolved from a relatively depth-uniform state at the beginning to a state of negative shear. This indicates that the Eulerian flow near the bottom experienced a positive enhancement, while the flow at the surface exhibited a negative enhancement. Vorticity was observed to increase in all wave conditions, with the most significant enhancement occurring at the surface. According to the theory of the conduction solution, vorticity should spread from the bottom or surface towards the interior of the water column, implying that the middle of the water column should exhibit the greatest vorticity enhancement. However, the observed surface enhancement of vorticity suggests that convection in the direction of wave propagation may play a significant role in this process.

Observing the rate of velocity displacement in the depth direction reveals significant variations over time near the water surface and at mid-depth, while changes near the bottom remain minimal. Although no clear time correlation is observed, these variations may suggest vorticity convection in the wave propagation direction near the surface. In the wave conditions of W3 and W4, the displacement rate in the y-direction was highest at $t = 5$ minutes and gradually decreased over time until reaching stability. This contrasts with W1 and W2, for which the current analysis does not yet provide an explanation for the observed discrepancy.

5.3. The Lagrangian velocity profile under equilibrium state

5.3.1. Comparison between different relative water depth

Our study, focusing on waves with kh values between 0.709 and 1.175, shows that the velocity profile qualitatively aligns with the conduction solution. This finding is consistent with the conclusions of **(author?)** [15] and **(author?)** [21] when considering relative water depth (kh) as a key variable. However, from a quantitative perspective, for wave conditions W2 and W4 ($kh = 0.959$) and W3 ($kh = 1.175$), the surface drift velocity in the Lagrangian profile is significantly smaller than the predicted values, with a deviation of 5-10 mm/s. Similarly, in the middle region of the water column, the negative peak velocity is smaller than predicted by the conduction solution. This profile shape could result from a more uniform vorticity distribution compared to the conduction solution. This suggests that vorticity transport does not fully follow the conduction solution, but instead indicates the presence of larger-scale vorticity propagating in another direction (either the wave-propagating or cross-shore direction). If it can be confirmed that the sidewall effects are minimal, then the deviation of the velocity profile from the conduction solution is likely due to the horizontal convection effect mentioned by **(author?)** [13].

Figure 5.1 compares the results of **(author?)** [15], **(author?)** [21], **(author?)** [19], and the present study (W3) at the surface and mid-depth. Overall, the velocity profile pattern aligns with the discussion above: the surface drift velocity in steady-state conditions is consistently lower than the predictions of the conduction solution, and in regions with negative flow, the magnitude of the flow is also smaller than predicted. In the bottom region (which was not covered in the present experiment), the observed values from **(author?)** [15] and **(author?)** [21] match the predictions of the conduction solution. From

Figure 5.1c, it can be observed that the velocity profile at the early stage of the experiment follows a more irrotational solution pattern.

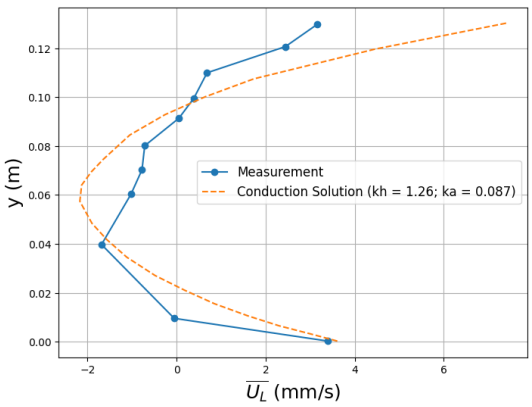

(a) (author?) [15] experiment result. h=0.13m, time-instance = 3 hour

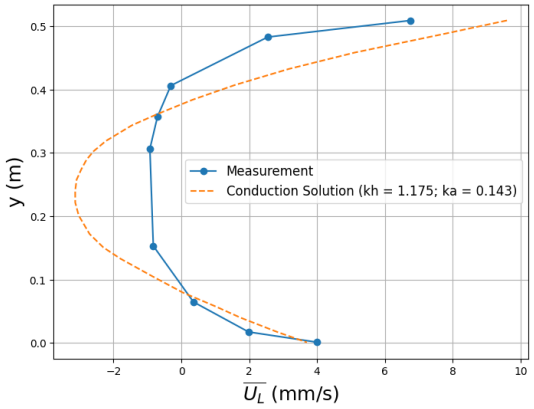

(b) (author?) [21] experiment result. h=0.51m, time-instance not addressed

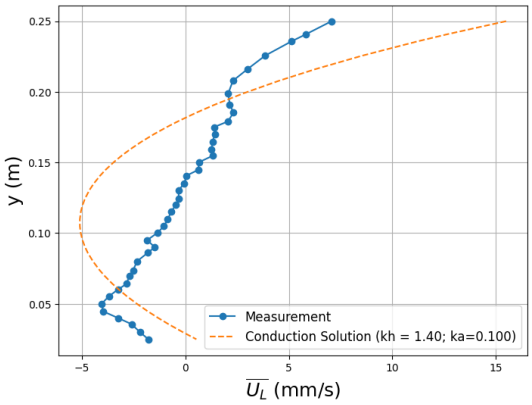

(c) (author?) [19] experiment result. h=0.25m, time-instance is at the beginning of the running

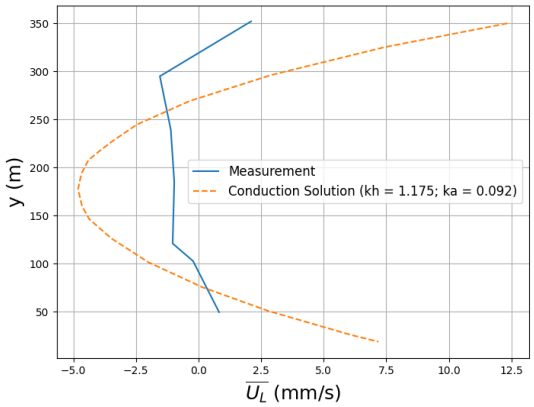

(d) Present experiment result. h=0.35m, time-instance = 2 hour

Figure 5.1: Measured Lagrangian velocity profile in comparison with Russell and Liu and the current experiment(W3).

5.3.2. Comparison between different relative wave steepness

The impact of relative wave steepness on surface drift velocity was also analyzed in this experiment. We non-dimensionalized the surface velocity for W2 and W4 ($kh = 0.959$) using Equation 4.2, and compared it with their corresponding ka values. In the experiment conducted by **(author?)** [21], there is a set of wave conditions ($ka = 0.931$, $T = 1.5$ s) similar to our W2 and W4. We applied the same method to non-dimensionalize the surface velocity, with the outcomes presented in Figure 5.2. In general, the non-dimensionalized mean Lagrangian velocity ($\overline{U_L^*}$) in this experiment does not differ significantly from the results of **(author?)** [21], with $F(kh)$ values of 0.495 and 0.449, respectively. In both experiments, it was found that as the ka value increases, the difference between $\overline{U_L^*}$ and the theoretical value also increases. This trend, observed in both **(author?)** [21] and our current experiment, suggests that the increase in ka causes the deviation from the conduction solution.

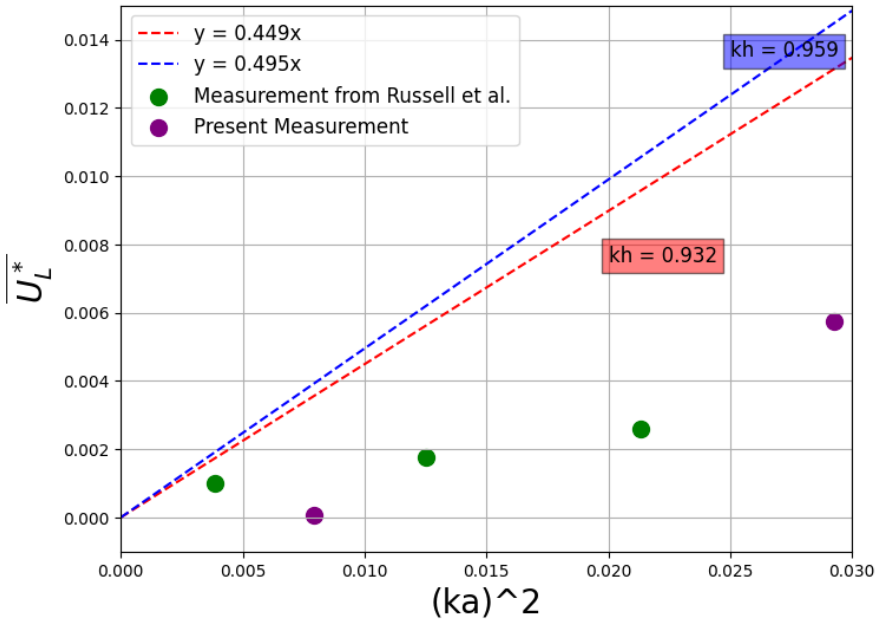

Figure 5.2: Comparison between the present measurement(W2 and W4) with Russell et al. using non-dimensional Lagrangian drift. The dashed line: conduction solution given by the present measurement(blue) and Russell's measurement(red)

6

Conclusion

This experiment, conducted in a wave flume, used LaVision's FlowMaster Shake-the-Box PTV system and Z-camera to analyze the evolution of Lagrangian velocity profiles over a period of 5 to 120 minutes under five different wave conditions.

6.1. Conclusion for Research Questions

What methods can be used to obtain the drift velocity from particle tracking data? What is the level of uncertainty in doing so? How does this uncertainty affect the analysis?

In order to extract the net drift velocity from the tracked particle motion, three averaging method is proposed. the time-averaging method, which calculates particle displacement over a long period, providing an overall drift but potentially including noise from large displacements; the wave-by-wave averaging method, which tracks displacement for each individual wave cycle, offering higher resolution and better depth accuracy, making it more stable for small samples; and the low-pass frequency filtering method, which filters out high-frequency components to focus on long-term drift, effectively removing short-term oscillatory behaviors and providing a smooth analysis of the net drift. Each method offers distinct advantages depending on the analysis goals. A comparison of the velocity profiles obtained by these three methods revealed that although the Wave-by-Wave method resolved the mean net flow along with the turbulent motion, it was the most stable and had a lower error, so it was decided to use the Wave-by-Wave method to analyse the velocity profiles in this study.

The uncertainty mainly arised from the follow two factors: 1.Spatial positioning uncertainty arises from inaccuracies in tracking particle positions over time, with errors potentially accumulating and impacting computed velocities, especially in the z-direction (cross-flume) and near the camera's field boundaries, where lens distortion may exacerbate inaccuracies. Cropping and selecting the central regions of the field of view help mitigate this uncertainty. 2. Background motion, although typically minimal, can introduce slight variability in observed drift velocities. It does not interfere with the drift velocity in the direction of the wave propagation, but have an impact on the vertical direction.

From a temporal perspective, what changes occurred in the velocity profile? How does it compare to the irrotational solution and the conduction solution?

From a temporal perspective, the velocity profile initially follows an irrotational flow pattern, characterized by relatively uniform motion, especially near the surface. Over time, vorticity begins to diffuse, and the profile shifts from this irrotational state to a more complex structure, increasingly resembling the conduction solution, particularly in the middle layers of the water column. Within approximately 60 minutes, the flow profile stabilizes, though discrepancies from both the irrotational and conduction solutions remain. During this stabilization process, the Eulerian flow becomes more sheared. While the irrotational solution accurately describes the early stages, the conduction solution progressively

approximates the flow behavior, although it never fully accounts for the observed complexity.

How do wave characteristics, such as relative wave height, steepness affect the velocity profile at equilibrium state? How does it compare to the irrotational solution and the conduction solution

Wave characteristics, such as relative wave height (kh) and steepness (ka), significantly impact the velocity profile. When kh is around 0.7, the velocity profile aligns well with the conduction solution. However, as kh increases beyond 2.0 (deeper water), the profile aligns more closely with the irrotational solution. For kh values between 0.96 and 1.18, the Lagrangian velocity profile shows a negative peak around the mid-water column, similar to the conduction solution, but the magnitude of this negative peak is significantly smaller. Meanwhile, at the surface, the Lagrangian drift velocity is more negative than predicted by the conduction solution. From an Eulerian perspective, a sheared current profile is observed.
For smaller wave steepness (ka), the conduction solution is more accurate, but as ka increases, the surface drift deviates from this solution due to violations of the small amplitude assumption.

Can the evolution of the velocity profile be explained from the perspective of vorticity transport?

The observed changes in the velocity profile can be understood through the lens of vorticity transport. Initially, vorticity is nearly zero in the upper part of the water column, consistent with the irrotational solution, which assumes regions with no vorticity. As time progresses, however, the observed vorticity differs from the conduction solution due to the presence of positive vorticity in the upper water column and negative vorticity in the lower part. These opposing vorticities interact and partially offset the vorticity predicted by the conduction solution, leading to a more uniform overall distribution of vorticity throughout the water column. This vorticity propagation is further influenced by more complex mechanisms, such as interactions with side walls and convection along the direction of wave propagation.

6.2. Future Work

Analysis of the surface drift velocity relative to wave steepness

The increase in ka (wave steepness) affects the small amplitude assumption of the conduction solution, thereby influencing the mode of vorticity conduction. In the existing experiments, the conduction solution often fails to accurately predict surface drift velocity in most cases, which could be related to the violation of the small amplitude assumption. However, in ocean environments, wave steepness cannot be ignored, especially in finite water depths, which may explain why the conduction solution is not always applicable in such settings. This is particularly relevant for nearshore regions, where complex wave dynamics, including the effects of steepness, play a crucial role in the transport and dispersion of pollutants. Understanding the relationship between surface drift velocity and ka can offer valuable insights into the movement of pollutants in these environments. Therefore, a more detailed analysis of this relationship is necessary to improve predictions of nearshore marine pollutant transport.

Constructing the Eulerian flow field and examining vorticity evolution

The transport of vorticity requires a more quantitative analysis through the examination of the Eulerian flow field. In this experiment, the PTV system allows the construction of such a flow field. The next step in the analysis will be to construct the flow field using the existing observational data and analyze the evolution of vorticity over time under different wave conditions. Furthermore, the results will be compared with previous datasets, such as those of **(author?)** [12] and **(author?)** [21], to provide context and validation. This will offer a more direct assessment of the diffusion and convective properties of vorticity.

Examining side walls and convection effects on velocity profiles

In this experiment, the vortex train was not studied in detail, making it impossible to quantitatively assess whether the convection pattern is significant. However, if future experiments confirm that the side walls do not significantly affect the velocity profiles, it can be assumed that vorticity convection is responsible for the deviations from theoretical predictions. Future research should also focus on examining the effect of side walls and the role of vorticity convection patterns in the flow.

Bibliography

[1] D. Andrews and Michael McIntyre. An exact theory of nonlinear waves on a lagrangian-mean flow. *Journal of Fluid Mechanics*, 89:609 – 646, 12 1978.

[2] EW Bijker, JP Th Kalwijk, and T Pieters. Mass transport in gravity waves on a sloping bottom. In *Coastal Engineering 1974*, pages 447–465. 1974.

[3] Oliver Bühler. *Waves and mean flows*. Cambridge University Press, 2014.

[4] Robert G Dean and Robert A Dalrymple. *Water wave mechanics for engineers and scientists*, volume 2. world scientific publishing company, 1991.

[5] S. Dey, S. Zeeshan Ali, and E. Padhi. Terminal fall velocity: the legacy of stokes from the perspective of fluvial hydraulics. *Proceedings of the Royal Society A: Mathematical, Physical and Engineering Sciences*, 475(2228):20190277, 2019.

[6] BD Dore. On mass transport velocity due to progressive waves. *The Quarterly Journal of Mechanics and Applied Mathematics*, 30(2):157–173, 1977.

[7] Steve Elgar, RT Guza, and MH Freilich. Eulerian measurements of horizontal accelerations in shoaling gravity waves. *Journal of Geophysical Research: Oceans*, 93(C8):9261–9269, 1988.

[8] Steven A Hughes. *Physical models and laboratory techniques in coastal engineering*, volume 7. World Scientific, 1993.

[9] Hwung-Hweng Hwung and C Lin. The mass transport of waves propagating on a sloping bottom. In *Coastal Engineering 1990*, pages 544–556. 1991.

[10] Michael Isaacson. Measurement of regular wave reflection. *Journal of Waterway, Port, Coastal, and Ocean Engineering*, 117(6):553–569, 1991.

[11] Jih-Yih Jiang and Robert L Street. Modulated flows beneath wind-ruffled, mechanically generated water waves. *Journal of Geophysical Research: Oceans*, 96(C2):2711–2721, 1991.

[12] Li Li and Robert A Dalrymple. Instabilities of the undertow. *Journal of Fluid Mechanics*, 369:175–190, 1998.

[13] Longuet-Higgins and S. M. Mass transport in water waves. *Phil.trans.roy.soc.london A*, 245(903):7611–7618, 1953.

[14] N Matsunaga, K Takehara, and Y Awaya. The offshore vortex train. *Journal of Fluid Mechanics*, 276:113–124, 1994.

[15] CC Mei, PLF Liu, and TG Carter. Mass transport in water waves. rep. 146, dep. *Civ. Eng., Massachusetts Inst. Technol*, 1972.

[16] SG Monismith, EA Cowen, HM Nepf, Jacques Magnaudet, and Laurent Thais. Laboratory observations of mean flows under surface gravity waves. *Journal of Fluid Mechanics*, 573:131–147, 2007.

[17] Stephen G Monismith and Derek A Fong. A note on the potential transport of scalars and organisms by surface waves. *Limnology and Oceanography*, 49(4):1214–1217, 2004.

[18] Kazuo Nadaoka and Takamichi Kondoh. Laboratory measurements of velocity field structure in the surf zone by ldv. *Coastal Engineering in Japan*, 25(1):125–145, 1982.

[19] Maciej Paprota, Wojciech Sulisz, and Anna Reda. Experimental study of wave-induced mass transport. *Journal of Hydraulic Research*, 54(4):423–434, 2016.

[20] Owen M Phillips. The dynamics of the upper ocean. *(No Title)*, 1977.

[21] RCH Russell and JDC Osorio. An experimental investigation of drift profiles in a closed channel. *Coastal Engineering Proceedings*, (6):10–10, 1957.

[22] Daniel Schanz, Sebastian Gesemann, and Andreas Schröder. Shake-the-box: Lagrangian particle tracking at high particle image densities. *Experiments in fluids*, 57:1–27, 2016.

[23] JFA Sleath. Mass-transport in water waves of very small amplitude. *Journal of Hydraulic Research*, 11(4):369–383, 1973.

[24] G. G. Stokes. On the effect of internal friction of fluids on the motion of pendulums. *Transactions of the Cambridge Philosophical Society*, 9(part ii):8–106, 1856. The formula for terminal velocity (V) appears on p. [52], equation (127).

[25] George Gabriel Stokes. On the theory of oscillatory waves. *Trans. Cam. Philos. Soc.*, 8:441–455, 1847.

[26] C Swan. Convection within an experimental wave flume. *Journal of Hydraulic Research*, 28(3):273–282, 1990.

[27] Laurent Thais. *Contribution à l'étude du mouvement turbulent sous des vagues de surface cisaillées par le vent| Theses. fr*. PhD thesis, Toulouse, INPT, 1994.

[28] Yoshito Tsuchiya, Takashi Yasuda, and Takao Yamashita. Mass transport in progressive waves of permanent type. In *Coastal Engineering 1980*, pages 70–81. 1980.

[29] Ton S van den Bremer and Øyvind Breivik. Stokes drift. *Philosophical transactions of the royal society a: mathematical, physical and engineering sciences*, 376(2111):20170104, 2018.

[30] TS Van Den Bremer, Colin Whittaker, R Calvert, A Raby, and Paul H Taylor. Experimental study of particle trajectories below deep-water surface gravity wave groups. *Journal of Fluid Mechanics*, 879:168–186, 2019.

A

Time Slot-Based Tracking Quality Assessment

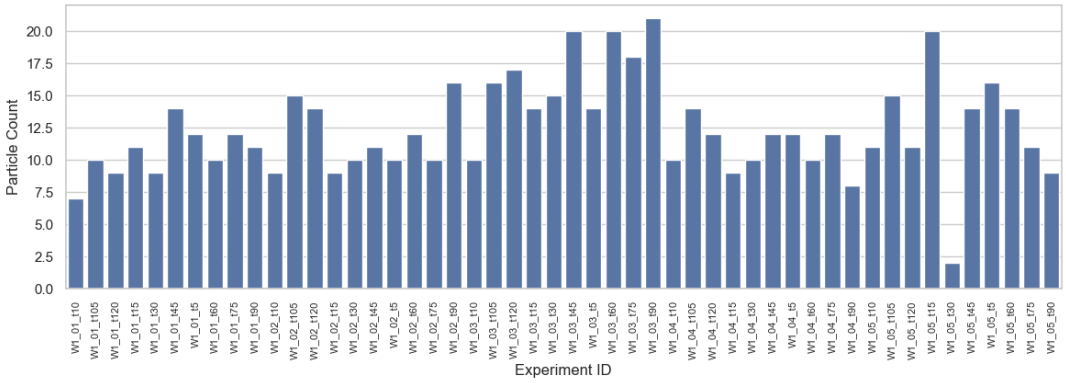

Figure A.1: W1 Particle Count

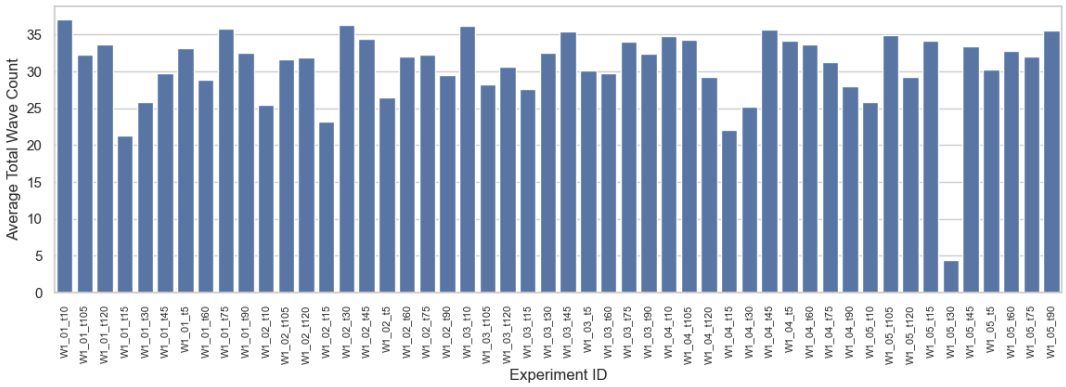

Figure A.2: W1 Wave Count

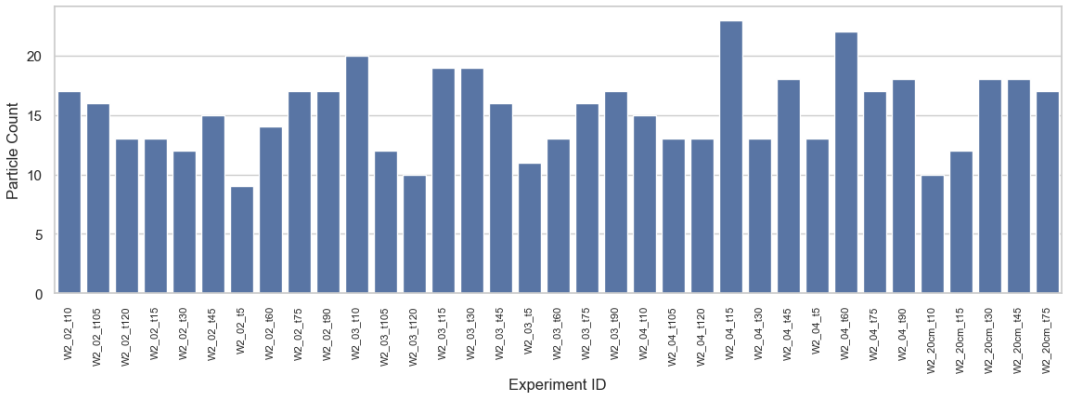

Figure A.3: W2 Particle Count

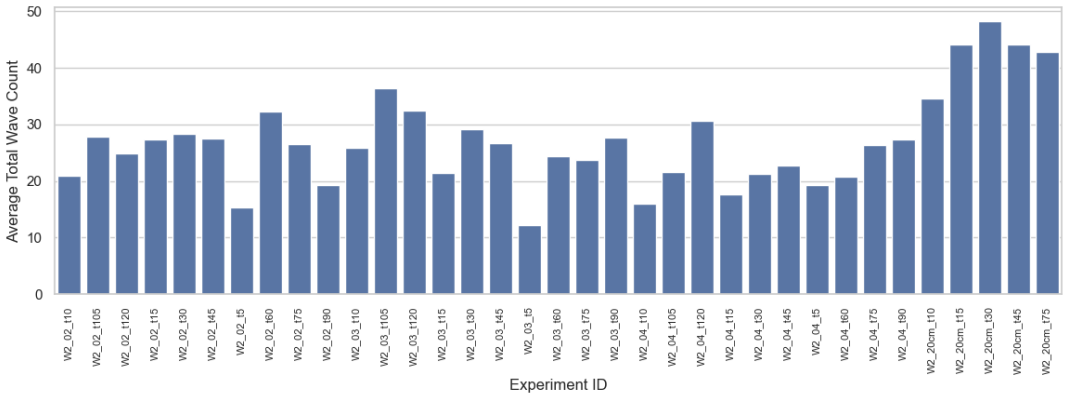

Figure A.4: W2 Wave Count

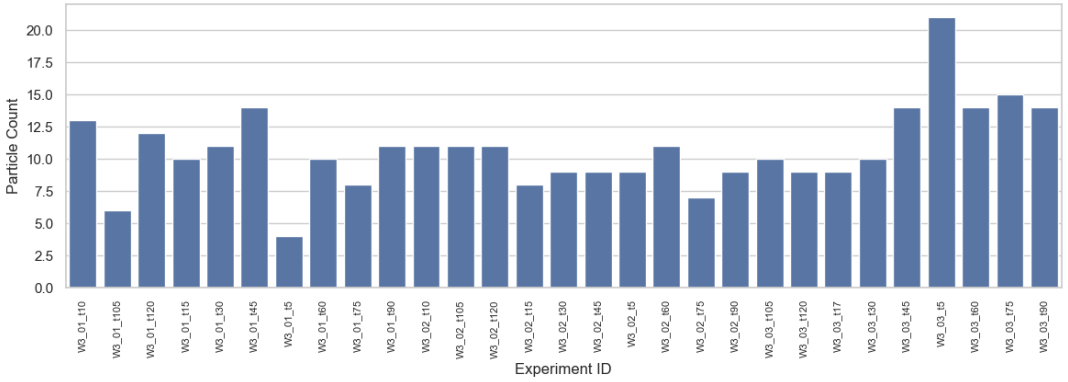

Figure A.5: W3 Particle Count

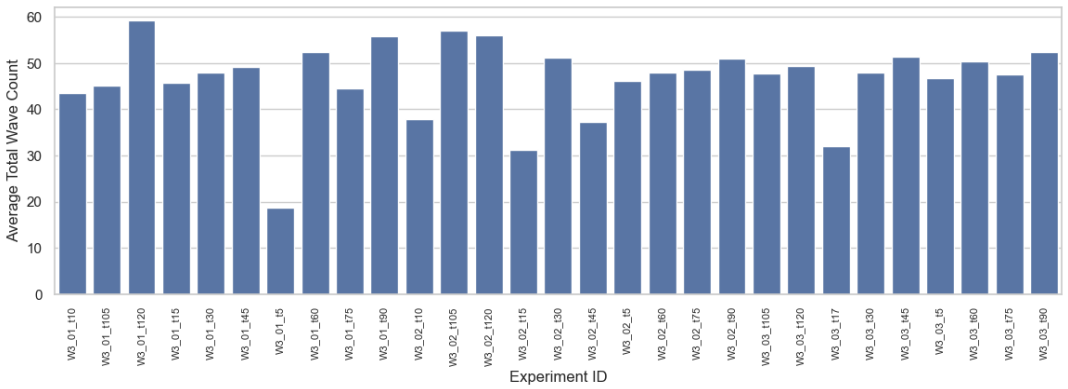

Figure A.6: W3 Wave Count

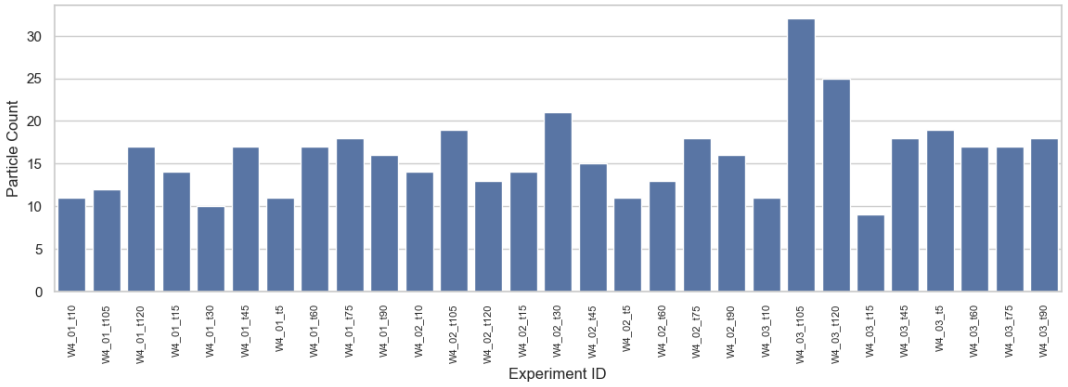

Figure A.7: W4 Particle Count

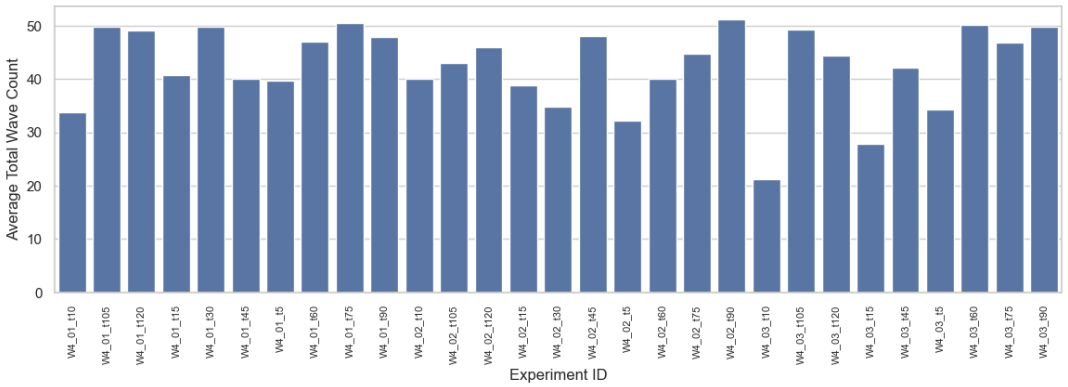

Figure A.8: W4 Wave Count

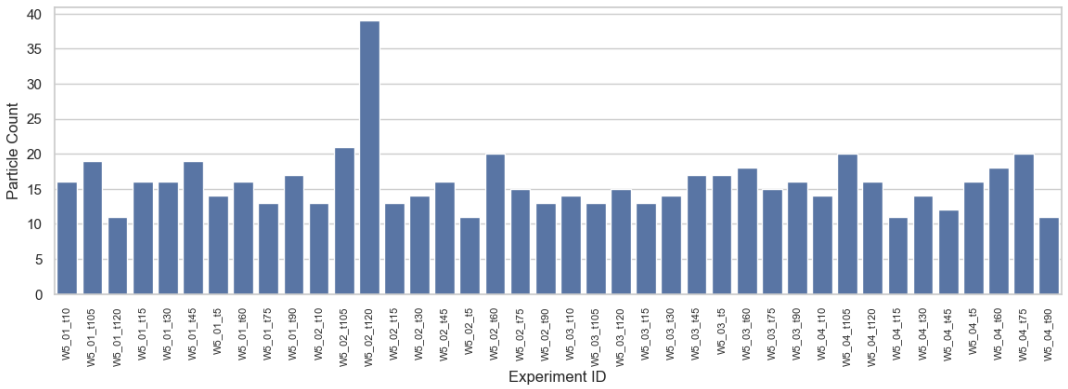

Figure A.9: W5 Particle Count

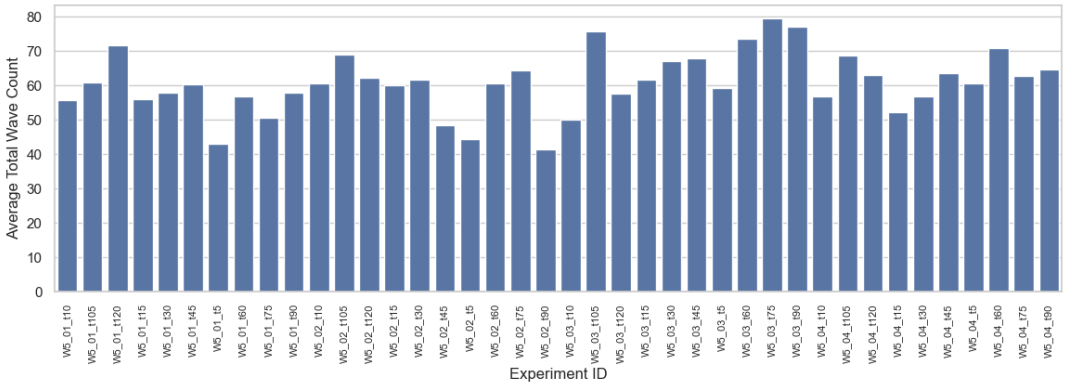

Figure A.10: W5 Wave Count